A MAGIC CUBE APPROACH FOR CRASHWORTHINESS AND BLAST PROTECTION DESIGNS OF STRUCTURAL AND MATERIAL SYSTEMS

by

Chang Qi

A dissertation submitted in partial fulfillment
of the requirements for the degree of
Doctor of Philosophy
(Mechanical Engineering)
in The University of Michigan
2008

Doctoral Committee:

Research Scientist Zheng-Dong Ma, Co-Chair
Professor Noboru Kikuchi, Co-Chair
Professor Christophe Pierre
Professor Victor C. Li

To my parents and my fiancée Coco

ACKNOWLEDGEMENTS

I would like to express my great appreciation and gratitude to my advisor, Dr. Zheng-Dong Ma, for his patient guidance and generous support during the whole process of this research, and for his concern and encouragement in my life. I don't think I would have finished this work without his help. I also wish to express my great respect and gratitude to Professor Noboru Kikuchi for his guidance, invaluable discussions, and innovative ideas provided during this endeavor. My sincere gratitude is also due to Professor Christophe Pierre and Professor Victor C. Li for serving on my doctoral committee, for reviewing this dissertation, and for offering helpful suggestions. I thank Dr. Ren-Jye Yang at Ford Motor Company for providing a design problem with industry background to enrich the applications of the proposed MQ approach in this research. And also, I thank Mr. Rod Perkins for helping revising the manuscript of this dissertation.

I wish to recognize my colleagues at the Computational Mechanics Laboratory: Dr. Jinzhong Wang, Dr. Harish Narayanan, Dr. Ercon Dede, and Mr. Geun Soo Ryu. I also want to mention some of my friends who have enriched my life in Ann Arbor: Dr. Jianmin Gu, Dr. Hui Wang, Dr. Dongying Jiang, Dr. Shih-Hsun Yin, Dr. Yi Yang, Dr. Jie Luo, Dr. Zhijun Li, Mr. Xin Chen, and Ms. Yuanyuan Liu.

Above all, I am particularly grateful to my parents and my brother, for their

support, patience, and encouragement, which I'll never be able to fully acknowledge. Special thanks to my fiancée Coco Zhang, for her love, friendship and support.

This research is supported by the Automotive Research Center Thrust Area III. I greatly appreciate the support from the ARC.

TABLE OF CONTENTS

LIST OF FIGURES

Figure

LIST OF TABLES

Table

ABSTRACT

A Magic Cube Approach for Crashworthiness and Blast Protection Designs of Structural and Material Systems

by

Chang Qi

Co-Chairs: Zheng-Dong Ma and Noboru Kikuchi

Crashworthiness design is one of the most challenging tasks in automotive product development, and blast protection design is crucial for military operations. The goal is to design an optimal crashworthy or blast-protective structure in terms of topology, shape, and size, for both structural and material layouts. Due to the difficulties in the crash analyses and the complexity of the design problems, previous studies were limited to component-level examinations, or considered only a simple design aspect. In this research, an advanced approach entitled the Magic Cube (MQ) approach is proposed, which for the first time, provides a systematic way to examine

general crashworthiness and blast protection designs in terms of both structural and material aspects.

The MQ developed in this research consists of three major dimensions: *decomposition*, *design methodology*, and *general consideration*. The *decomposition* dimension includes the major decomposition approaches developed for the crashworthiness design problems, and it can be applied to the blast protection design. It has three layers: *time (process) decomposition*, *space decomposition*, and *scale decomposition*. The *design methodology* dimension is related to the methodologies employed in the design process; three layers in this dimension are: *target cascading*, *failure mode management*, and the *optimization technique*. The *general consideration* dimension has three layers, which are *multidisciplinary objectives*, *loadings*, and *uncertainties*. All these layers are coupled with each other to form a 27-element magic cube. A complicated crashworthiness or blast protection design problem can be solved by employing the appropriate approaches in the MQ, which can be represented by the corresponding elements of the MQ. Examples are given to demonstrate the feasibility and effectiveness of the proposed approach and its successful application in real vehicle crashworthiness, blast protection, and other related design problems.

The MQ approach developed in this research can be readily applied to other similar design problems, such as those related to active safety and vehicle rollover.

CHAPTER I

Introduction

1.1 Overview

Increased traffic intensity, the mounting concern of the public about personal safety, and new stringent laws have combined to make vehicle safety one of the major research areas in automotive engineering. Vehicle safety research can be divided into two main areas: accident avoidance and mitigation of injuries. These two areas are often called active safety and passive safety, respectively. Accident avoidance (active safety) includes all measures that serve to prevent car accidents; while mitigation of injuries (passive safety) includes all measures that help to reduce injuries during accidents. Vehicle passive safety is directly related to the vehicle's structural crashworthiness, which will be the topic of this research.

Structural crashworthiness has been studied ever since the safety of vehicles first came under scrutiny, while the term "crashworthiness" was first used in the aerospace industry in early 1950's. In the automotive industry, crashworthiness connotes a measure of the vehicle's structural ability to plastically deform and yet maintain a sufficient survival space for its occupants in crashes involving reasonable

deceleration loads. The methodologies developed in this dissertation are applicable for other crashworthiness design problems; however, most of the example problems are from the automotive industry. Unless specified otherwise, structural crashworthiness will refer to automotive structural crashworthiness in this research.

With increased terror attacks, vehicle safety should be extended to address more severe loads such as the impact from blast and ballistic attacks, especially for military vehicles. Military vehicles are being reformulated to be safer and more efficient, yet with significant weight savings. Surviving a mine blast is of particular concern; new technology for blast protection design needs to be developed, and this is another topic of this research.

The following sections of this introduction present the state of the art of vehicle crashworthiness design and the blast protection design. Then, the motivation is presented and the research objective is proposed. Finally, the dissertation organization is laid out.

1.2 State of the Art of Vehicle Crashworthiness Design

Vehicle crashworthiness design has been studied for decades. With the introduction of higher standards for vehicle safety via government mandate and consumer demand, design for crashworthiness has become a major task in the vehicle development process. The goal of crashworthiness design is a vehicle body structure that can absorb the crash energy through controlled deformation, while maintaining adequate survival space so that the residual crash energy can be managed by the restraint systems, thus minimizing the crash loads transferred to the

vehicle occupants. This design goal is based on the following facts. On one hand, the body structure should be stiff enough to maintain sufficient integrity to prevent extra deformation or intrusion into the passenger compartment, i.e., to provide certain survival space. On the other hand, the deceleration level experienced by the occupant should be minimized; this requires the body structure to be soft enough to plastically deform and absorb as much crash energy as possible, so as to alleviate the deceleration pulse. This is a basic trade-off in vehicle body structure design problems. A vehicle body structure with good crashworthiness performance should provide a compromise between these two aspects, so as to make the design of the restraint system much more effective in meeting various vehicle safety standards, and more likely to achieve high star ratings in various vehicle safety evaluation programs.

1.2.1 Structural Crashworthiness Indices

Structural crashworthiness is indicated by various indices. Crash force history is an important index of a vehicle's crashworthiness. From a design point of view, a nearly constant crash force without large peaks is preferred for a crash event, since large crash peaks usually result in high acceleration of the occupant. Another line of thinking is that an acceptable peak crash force is needed in the early stage of a crash event, to activate the restraint system, i.e., seat belts, airbags, etc., for early protection of the occupant. In this work, a predefined crash force history is set as the design target for the crashworthiness design of a representative vehicle.

Energy absorption is closely related to the crash force history and is another

important crashworthiness index; the more crash energy absorbed by the vehicle structure, the less energy must be handled by the restraint system. For an energy absorption structural component, the specific energy absorption (SEA) is defined as

$$SEA = \frac{E}{m} \tag{1.1}$$

where E is the energy absorbed during a crash process, and it can be obtained by integration of the crash force-deflection curve; m is the total mass of the EA component. Crashworthiness design should always maximize the SEA, since a high SEA value implies a high efficiency of crash material usage.

Critical buckling force can be viewed as another index of crashworthiness; it determines the critical conditions when a structural component or a mechanical system buckles, either elastically or plastically, under a crash load. Crashworthiness design serves to maximize the critical buckling force of a structural component or a mechanical system. The critical buckling force is set as one of the objectives in the elastic mounting system (EMS) design problem discussed in Chapter IV.

1.2.2 Design Variables

Crashworthiness design variables can be generally classified into two categories: system-level design variables and component-level design variables. System-level design variables can include the variables that determine the position of a subsystem or a component in the system configuration, or the mass and the stiffness of a subsystem or a component, etc. In a vehicle crashworthiness design problem in Chapter III, control points on the force-deflection curves of various assemblies and

components are defined as design variables. Component-level crashworthiness design variables can be the following: size (panel thickness, trigger position, etc. [1]), shape (cross section profile), material properties (yield stress, etc. [2]), and structural topology (density or micro-cell dimension [3]).

1.2.2 Simulation Models

Experimental testing of vehicle crashes is very expensive and time-consuming, and it can be used only in the design stage when the design is close to being finalized. With advances in computer aided engineering (CAE) techniques, vehicle crash processes can be simulated and crashworthiness designs can be conducted using high-fidelity simulation models to partially or fully substitute the crash test, substantially reducing the time and cost of development.

Finite Element Models

Vehicle crashworthiness analysis is among the most challenging problems in structural mechanics due to the several complex phenomena, including non-linear material properties (plasticity, hardening, etc.); non-linear geometry (large deformations and displacements, buckling); dynamic load and impact (inertial effects); surface contacts (including self contact); and strain rate effects due to the speed of the crash. With the development of the explicit finite element (FE) method in the 1960's and 1970's, as well as with the introduction of supercomputers, full vehicle crash FE models were built and analyzed in the mid 1980's. During the last decade, development and improvement of the explicit FE codes continued to make

numerical solutions of vehicle crashworthiness analyses more accurate and stable. A FE crashworthiness model should satisfy at a minimum the following overall requirements:

1) Accuracy: the model should be able to yield reasonably accurate predictions of the essential features being sought;

2) Economy: the model should be executable within a reasonable turnaround time;

3) Robustness: small variations in model parameters should not yield large variations in model responses;

4) Ease of development: the model should be built in a reasonably short period of time.

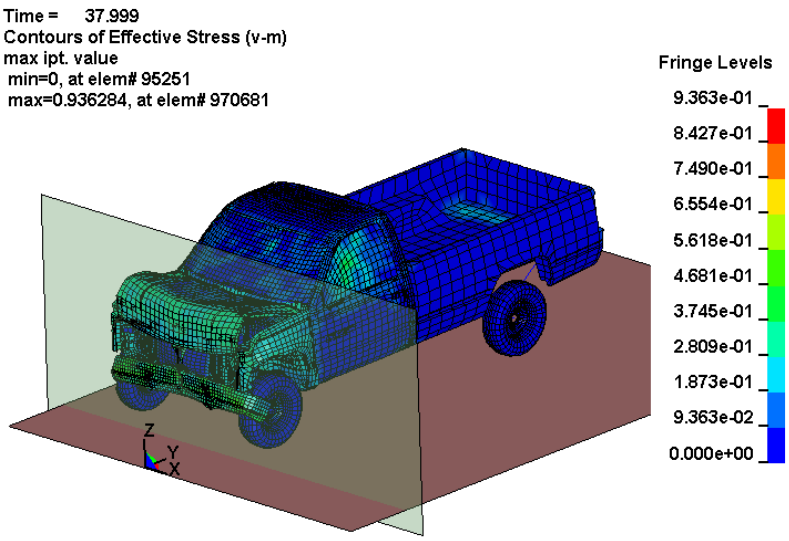

Figure 1.1: An example vehicle crash simulation with finite element modeling

A FE analysis can provide detailed structural deformation and stress (plastic strain, etc.) distribution. Based on this information, design revisions can be made to

achieve improved crash performances. Figure 1.1 shows an example of a vehicle frontal crash simulation result using a FE vehicle model.

Meta-Models

One major disadvantage of the FE model is its high computational requirement, which makes it less attractive for optimization studies involving many simulations. As a result, meta-models with less fidelity but with much lower computational costs have been developed, especially for design optimization purpose. These meta-models include a coarse-meshed FE model, a lumped mass-spring (LMS) model, a multi-body model, or a model built with beams and trusses, etc. Parametric optimization techniques by using these meta-models have been studied extensively [4] [5] [6]. The main problems associated with such models are the typical low model fidelity, and the realization of getting the optimized lumped parameters into an actual structural design. Despite these problems, however, some meta-models do provide formalisms for estimating the load and stiffness requirements of substructures and in some cases individual structural components.

A relatively simple meta-model is the LMS model developed by Kamal in 1970 [7]. As shown in Fig. 1.2, the major nonstructural components of a vehicle are represented by lumped masses, and major deformable structural components are modeled as non-linear spring elements, called energy absorbers (EAs), typically represented with force-deflection curves. The dynamic environment of the crash event is addressed by the velocity sensitivity factors (or called dynamic amplification

factors). Several versions of the LMS models have been successfully used in simulations of frontal, side, and rear vehicle crashes [6] [8] [9].

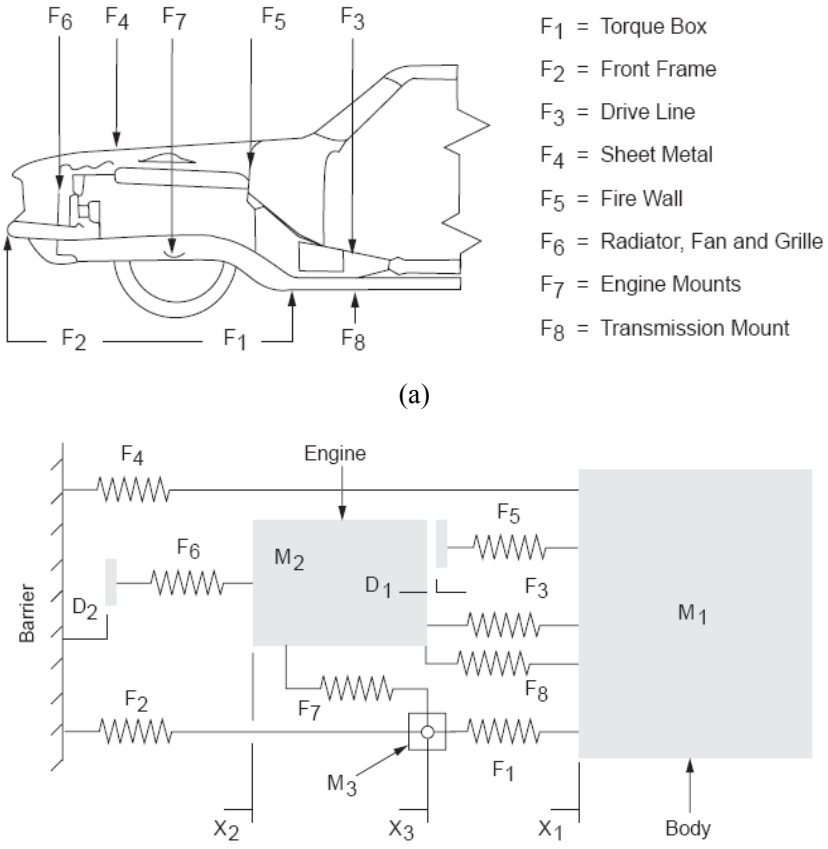

Figure 1.2: Kamal's model: (a) vehicle forestructure; and (b) lumped mass-spring model of (a). [7]

The drawbacks of the LMS model are obvious: the level of simplification is very high, and it cannot provide detailed structural deformation and stress distribution. On the contrary, building an LMS model requires prior knowledge of the constitutive characteristics of the deformable structural components, which must be determined experimentally, or calculated from FE models or an equivalent procedure. In such, the ability to accurately compute or acquire the model spring characteristics is one of the primary limitations with this modeling approach. In addition, the LMS model is

one-dimensional, modeling only the behavior in the longitudinal direction; a behavior due to the mismatch or non-alignment of the structure in the vertical plane or a horizontal plane cannot be captured. Therefore, offset or angular impact cannot be simulated by the LMS model. Despite these limitations, a big advantage of the LMS model is its high computational efficiency; a typical crash simulation using a LMS model takes only a couple of minutes or even seconds to finish. This gives the LMS model the ability to be used in the system-level design optimization process, to obtain the system configuration of a vehicle system. In this work, a finely tuned LMS model is employed for space decomposition of a vehicle system through a target cascading process, such that subsystem-level and component-level design objectives can be established for the following detailed design.

An improved version of the LMS model worth mentioning is the equivalent mechanism (EM) approximation model proposed by Hamza [10]. In this model, rigid beams and revolute joints are added to the traditional LMS model to capture a specific geometry of a crash mode, like a plastic hinge. The EM approximation model is still a highly simplified model with a lot of information loss. It also requires experiments or FE simulations to determine the spring parameters needed to construct the model.

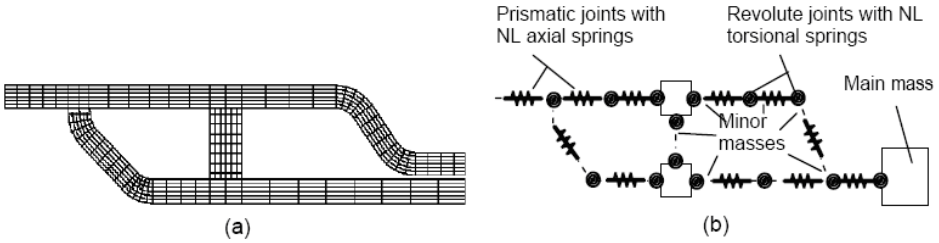

Figure 1.3: Equivalent mechanism approximation model of a vehicle substructure: (a) finite element model; and (b) equivalent mechanism model. [10]

Another similar meta-model used by many researchers [4] [5] [11] [12] is the multi-body model as shown in Fig. 1.4, in which a structure is approximated by a multi-body constrained mechanical system with revolute joints and non-linear revolute springs representing plastic hinges. In fact, an LMS model or an EM approximation model can be considered as a special case of the more general multi-body model formulation.

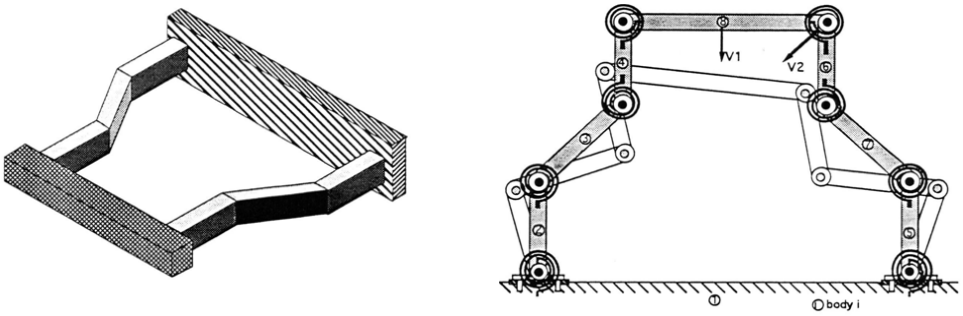

(a) (b)

Figure 1.4: Structural and multi-body model for an under-frame end: (a) simplified under-frame end; and (b) simplified multi-body model with plastic hinges. [11]

The three meta-models mentioned above either use longitude springs, or torsional springs, or both to represent structure stiffness, while the structural topological configurations are neglected. A more complicated crashworthiness meta-model that can overcome this shortcoming is the so-called lattice model, which uses

linked beam or truss (lattice) elements according to the structural topological configurations, as shown in Fig. 1.5 [13]. Compared to the full FE model, a lattice model is more computationally efficient, yet it can represent structural topological configuration in certain contexts and can be used for design purposes [14].

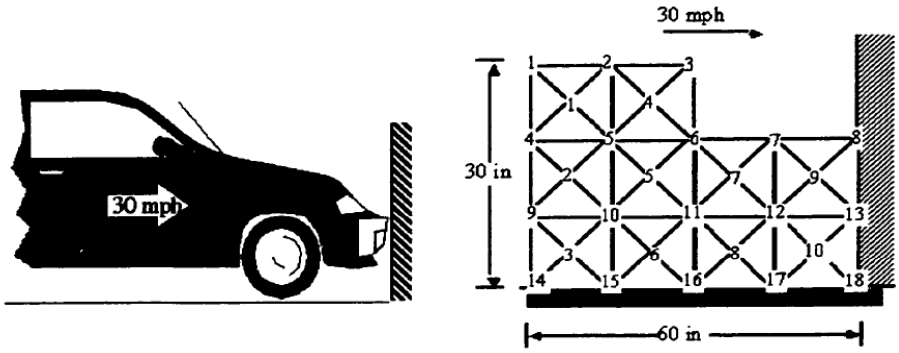

(a)

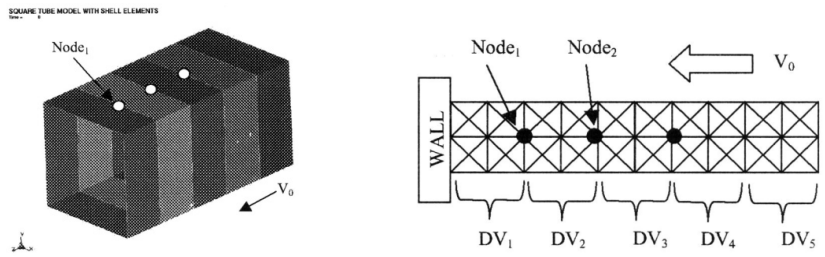

(b)

Figure 1.5: Lattice crashworthiness models: (a) system-level; and (b) component-level. [13]

1.2.3 Optimization Techniques

Optimization techniques for crashworthiness design can be grossly classified into two categories: parametric optimization techniques based on approximation models, and structural optimization techniques for component and system configuration design.

Parametric Optimization Technique

As mentioned previously, parametric optimization techniques by using the meta-models have been studied extensively. To include more detailed information in the parametric optimization process, the FE model should be used. As mentioned previously, the high computational requirements of a FE crash model limit its application in such a parametric optimization process. A feasibility study using numerical optimization methods and an FE model to design structural components for crash was presented by Yang et al. [15]. It was found that crash optimization with the FE model was feasible but very costly and that high FE mesh quality was essential for successful crash analysis and optimization.

Another difficulty faced in vehicle crashworthiness optimization with FE modeling is related to the fact that the objective and constraint functions are often not smooth, due to the numerical inaccuracies in the explicit non-linear dynamic code, as well as because of the essential non-smooth properties of a crash event itself. This makes it difficult to obtain accurate sensitivities for routine use in the parametric design optimization process.

To overcome this difficulty, much research has been dedicated to building approximate models with smooth responses and less computational cost. The most widely adopted technique is the response surface method (RSM), which builds an algebraic function (response surface) to capture the input-output relationship of a complex FE crash model based on a number of sampling points in the design space. With the construction of the response surfaces, noisy or unphysical components of

the objective and constraint functions are smoothed out. The optimal solution is then sought on these smoothed surfaces with less effort. The selection of approximation functions is essential. These functions can be polynomials of any order but can also be sums of different basis functions, e.g., sine and cosine functions. Once the structural crashworthiness responses are approximated, parametric optimization algorithms can be applied in the subsequent design process to obtain the optimal design for crashworthiness.

Etman et al. [16] were among the first to use RSM in structural optimization. Schramm and Thomas applied RSM using polynomial functions to optimize a wide range of crashworthiness designs [17]. Yamazaki and Han [1], Wang et al. [18], and Avalle et al. [19] used RSM for the crashworthiness design of thin-walled tabular structures. Marklund and Nilsson [20] used RSM for an industrial application by minimizing the weight of a B-pillar of a vehicle without the loss of safety. Redhe et al. [21] studied different aspects of RSM in crashworthiness applications and carried out some work on space mapping compared to RSM. A neural network can be viewed as a special case of non-linear response surface and has been shown to be able to approximate any function to an arbitrary degree of accuracy [22]. The use of the multilayer perceptron or back propagation (BP) neural networks in crashworthiness optimization problems was investigated by Hajela et al. [23].

While RSM and other approximation models have been successfully applied to parametric optimization for crashworthiness, the ranges of the design variables are often fairly limited in order to build a relatively accurate model with a small number

of sampling points, each of which requires a full crash simulation. The difficulty lies in minimizing the number of simulations, since numerical crash simulation is very expensive, while simultaneously achieving a response surface with high fidelity. Design of experiments (DOE) provides a systematic and formal way of defining a design matrix, and for studying the effects of design variables. Several methods exist for DOE, including the factorial method, the orthogonal method, the composite design method, sobol sequence, and the Latin hypercube method [24].

Structural Optimization Technique

Modern structural optimization has evolved since the 1940s, when it was developed from the aerospace industry. This development moved from the original stage of considering only the size or geometrical dimension of a structure, as illustrated in Fig. 1.6a, to a more generalized shape optimization consisting of finding the optimal shape of the boundary of a structural system as illustrated in Fig. 1.6b, to finally simultaneously selecting the best geometric and topological configuration while still taking into account the geometry and physical dimensions as well as connectivity of members and joints, as shown in Fig. 1.6c. Structural topology optimization has considerable practical importance because it results in greater material savings than size and shape optimizations.

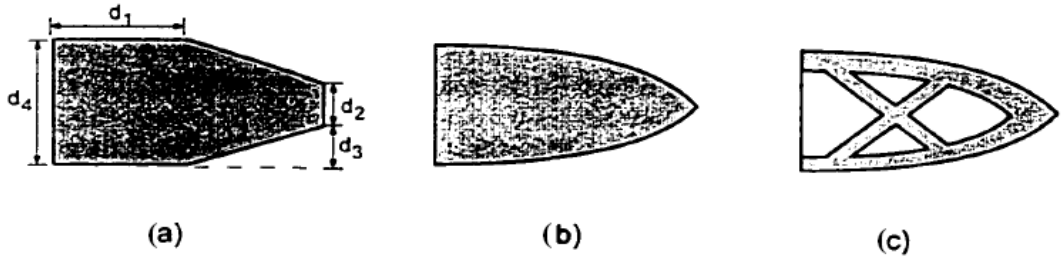

Figure 1.6: Classification of structural optimization: (a) size, (b) shape, and (c) topology optimization.

Based on the structural model, topology optimization for crashworthiness design can be divided into two categories: optimal topology design for discrete structures, and optimal topology design for continuum structures. For discrete structures, topology optimization implies the determination of the sequence of members and joints. Pedersen considered simplified planar models while ignoring contacts between elements [14]. The sensitivity analysis was derived analytically, which made the algorithm very efficient. The modeling was based on plastic beam elements, and an implicit dynamic Newmark time-stepping algorithm was applied for obtaining the transient response.

In continuum structures, topology optimization refers to the optimal material distribution, which assigns material properties and densities within a given design domain. The revolutionary homogenization-based method for topology optimization proposed by Bendsøe and Kikuchi [25] inaugurated a new era in this field, including the application of it to crashworthiness design. Mayer and Kikuchi [3] first introduced the topology optimization technique to the structural crashworthiness design based on the gradient method. The topological optimization of components to maximize crash energy absorption for a given volume was considered. The crash

analysis was performed using a DYNA3D FE analysis. Optimality criteria were derived using densities as the design variables, and a resizing algorithm was constructed. A novel feature is the introduction of an objective function based on strain energies weighted at specific times. Gea and Luo [26] implemented a regional strain energy formulation to topology design optimization for energy absorption. In addition to the gradient-based methods, Soto [27] proposed a heuristic approach for topological design with crashworthiness objectives. One drawback to this approach is that it requires much engineering experience to determine the necessary parameters to conduct the design. The lack of a systematic attribute limits its application to more general crashworthiness design problems. Some other works of topology design for crashworthiness include those conducted by Diaz and Soto [28], Arora, et al. [29], Knap and Holnicki-Szulc [30], Yamakawa, et al. [31], and Marzec and Holnicki-Szulc [32].

The standard topology optimization method optimizes a structure within a single structural domain, and it is subjected to a given amount of material for the whole structure. The optimization process determines material distribution automatically without interacting with the designer, leaving little flexibility to the designer for controlling the material in a way he/she may desire. A multi-domain topology optimization (MDTO) technique was developed by Ma, et al. [33]. In contrast to single domain topology optimization, the MDTO technique allows the designer to assign different amounts of material, or even different materials, to the different sub-domains of the structure. Figure 1.7 shows a structural domain divided into several

sub-domains, where a certain amount of material A is distributed into Sub-domain 1; and a different amount of material B is distributed into Sub-domain 2. Furthermore, Sub-domain 3 is considered as a non-design domain, where material distribution is not allowed to change at the current design stage.

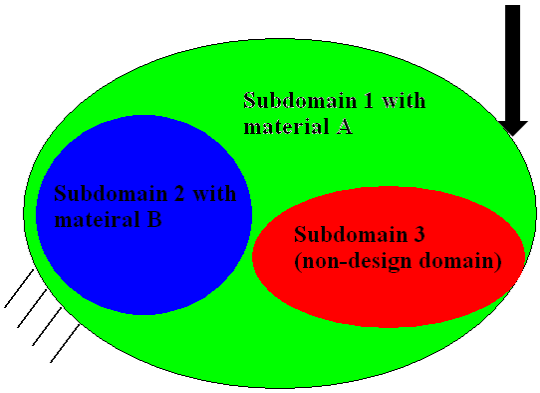

Figure 1.7: A multi-domain topology optimization problem

In the general case, the optimization problem of the MDTO can be written as

$$\begin{aligned} &\text{Minimize } f(\mathrm{X}) \\ &\text{Subject to } h_j(\mathrm{X}) \le 0 \ (j = 1,2,\ldots,m) \\ &\qquad \underline{x}_j \le x_j \le \overline{x}_j \ (j = 1,2,\ldots,m) \end{aligned} \tag{1.2}$$

where $f = f(\mathrm{X})$ denotes the objective function; $h_j(\mathrm{X})$ denotes the j-th constraint function for the volume (or weight) of the j-th substructure in the j-th sub-domain (where $j = 1,2,...,m$); $\mathrm{X}=\{x_1, x_2, \cdots, x_n\}^T$ denotes the vector of the design variables; and $\underline{x}_j$ and $\overline{x}_j$ are the lower and upper bounds of design variable, respectively. Note that $f(\mathrm{X})$ in Eq. (1.2) needs also to satisfy the state equations of the structural analysis problem at hand.

Based on the MDTO technique, Wang et al. [34] proposed a multi-step topology optimization (MSTO) approach that can simplify the architecture of a structure and

thus improve the manufacturability of the design. In this research, instead of conducting a multi-step design for the whole structure as in Wang's work, the multi-step approach is integrated into the MDTO process to achieve more robust crashworthiness design configuration, resulting in a more general multi-domain multi-step topological optimization (MMTO) technique. This is applied to crashworthiness design with advanced three-dimensional design capabilities, and it will be demonstrated through an example in Chapter II.

1.2.5 Multidisciplinary Design Objectives

For ground (military) vehicle body structures, in addition to crashworthiness and blast protection design requirements, other design requirements, including structural stiffness, noise vibration and harshness (NVH), durability, etc., should be considered as well. Design targets developed from each of these disciplines usually impose conflicting requirements on the topology, shape, and size of the body structure; this makes the vehicle body structural design a complicated multidisciplinary design problem.

Some work was done previously with multidisciplinary design goals including crashworthiness objectives. Multidisciplinary topology optimization was studied by Yang [35], where the structural weight was chosen as the objective function, and structural responses such as the compliances, displacements, and the natural frequencies were treated as constraints. Schramm [21] optimized the mass of a bumper beam while under a barrier intrusion (displacement) for a centerline barrier hit, and under a constraint on its first natural frequency. Sobieski et al. [36] used

RSM to minimize the mass of a vehicle when the roof crash performance was coupled to its NVH. Craig [37] conducted multidisciplinary design optimization (MDO) of a full vehicle to minimize mass while complying with crashworthiness and NVH constraints. Yang et al. [38] focused on the methodology development and the application of reliability-based MDO to vehicle crashworthiness design under the constraints of full frontal impact, roof crash, side impact, 50% frontal offset impact, and other safety performance measurements. The MDO of a vehicle system for safety, NVH, and weight was addressed by Kodiyalam et al., in a scalable high-performance computing environment, utilizing several hundred processors in conjunction with approximation methods, formal MDO strategies, and engineering judgment in order to obtain superior design solutions with significantly reduced computing times [39].

In the methodology side, Kodiyalam and Sobieski [40] gave a comprehensive review of the formal MDO methods and laid out the framework requirements to perform MDO. The methods to treat MDO includes the all at once (AAO) method, the multidisciplinary feasibility (MDF) method, the individual discipline feasibility (IDF) method, collaborative optimization (CO), concurrent subspace optimization (CSSO), and bi-level integrated system synthesis (BLISS), etc. In this work, in addition to these methods, an objectives reduction approach (ORA) is proposed and is shown to be feasible and effective in handling a multidisciplinary design problem.

1.2.6 Uncertainty Effects

Like other real-world problems, the crash event of a vehicle is characterized by

non-deterministic processes. Non-deterministic behaviors are essential to these processes. In a vehicle crash event, uncertainties such like the impact velocity, the impact angle, the mass of the vehicle, and the mass and stiffness of a barrier, to name just a few, will influence the crash performance of the vehicle. These uncertainty effects should be considered in the crashworthiness design process to achieve more robust designs of vehicle structures for occupant protection during a crash event.

Due to the lack of computational resources, simulation capabilities, and efficient optimization methodologies, it is often not feasible to include all uncertainty effects in a design problem. Youn et al. [41] investigated two optimization methodologies, the reliability index approach (RIA) and the performance measure approach (PMA), for reliability-based MDO; they demonstrated them by applying them to a crashworthiness design optimization of vehicle side impact with uncertainties taken into consideration. Koch et al. [42] presented an implementation of design for six-sigma (DFSS) for a side impact crashworthiness design problem with consideration of uncertainties in design parameters. In this research, uncertainties are considered throughout, in order to achieve more robust design configurations of both crashworthiness and blast protection designs.

1.2.7 Material Design

Material properties play an important role in structural crashworthiness design. In recent years, the automotive industry has increasingly focused its research on composite materials, due to their superior performance in areas such as high specific energy absorption in crashes, high stiffness-to-weight ratios, high strength-to-weight

ratios, fatigue resistance, and corrosion resistance in comparison with traditional metallic materials. Experimental testing and numerical simulation are widely used to study composite materials' responses under crash loads. Design optimization techniques are used for studying composite material configurations that provide improved crashworthiness capabilities. Carruthers [43] reviewed the energy absorption capability and crashworthiness of composite structures, with the examination of correlations between failure mode and energy absorption, as well as the material, geometrical, and physical parameters relevant to the design of crashworthy composite structures. Ramakrishna [44] conducted a micro-structural design of composite materials for crashworthy structural applications. The effects of microstructure variables, including the type of reinforcements and matrices, reinforcement architecture, and reinforcement/matrix interface bond strength on the energy absorption characteristics of polymer composite materials, were described.

The remaining challenge in this field is the use of specific features of geometry and materials in enabling greater safety, while simultaneously decreasing the weight, without negatively affecting the overall economics of fabrication and production. This requires the design of the microstructures of a composite material to tailor material properties from the base material. The topology optimization technique has great potential applications in this area.

In this research, a scale decomposition approach is proposed to link the macro-level structural design to micro-level material design with crashworthiness objectives; it provides a new way to achieve microstructure configuration design targets from

the global responses of a composite material.

1.3 State of the Art of Blast Protection Design

For ground military vehicles, in comparison to crash loads, blast loads from landmine explosions and ballistic loads from a bullet or a missile usually produce much more damage to the vehicle structure and result in more severe injuries to crew members.

Armor structures are usually employed to protect a military vehicle from these extreme loads. Major requirements for the advanced vehicle armor structure are low weight, flexibility, maintainability, and low life-cycle cost. Low weight is crucial to maintaining excellent road and cross-country mobility, which are directly related to military deployability and survivability. Low weight is also crucial to transportability and sustainability as well as to structural integrity and durability. Flexibility means the armor structure can be shaped or formed to fit various vehicle contours. Maintainability implies two things: the integrated armor system can be easily installed and removed from the vehicle with minimal time and manpower; and the armor can be easily repaired during war time without replacing the whole armor structure. Life-cycle cost is directly related to affordability and the wide application of armor system.

To protect the vehicle structure from blast shock wave acceleration and deformation, one idea is to design protection panel structures that deflect blast waves so as to lower the load level on the structure. Using numerical analysis, Pytleski et al. designed a wedge/wing deflector structure and placed it under a truck's cab [45].

These crew/vehicle protection panels can increase crew survival in tactical wheeled vehicles subjected to mine blasts. However, these protection kits are based on conventional steel/aluminum construction and weigh nearly 0.5 tons; thus they are not suitable for light-weight military vehicle applications.

Another design concept for blast protection is using sacrificial material (composite, foam, etc.) to absorb blast energy. The philosophy is illustrated in Fig. 1.8. In the event of a blast attack, the sacrificial material absorbs energy and undergoes a significant amount of deformation. In order for the blast load not to permanently damage the main structure, the collapse load of the sacrificial layer should be kept below the maximum elastic capacity of the main structure, with all dynamic effects taken into account. The blast loading is given a linearly decaying pressure vs. time curve. The ideal control of the contact pressure between the sacrificial layer and the main structure is obtained by selecting a perfectly plastic material and component as the sacrificial part.

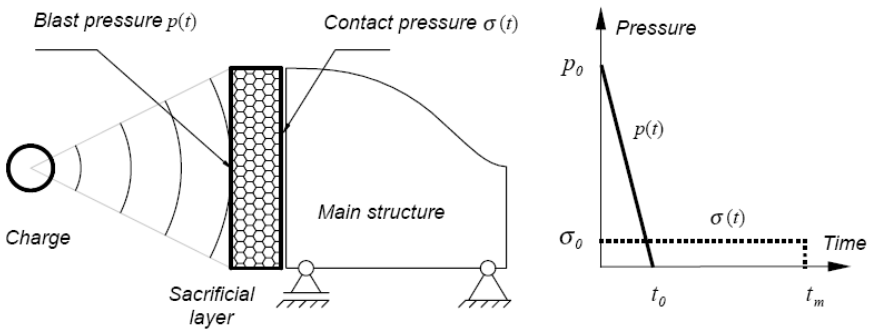

Figure 1.8: Sacrificial material design concept for blast protection

Guruprasad and Mukherjee [46] [47] carried out free-field experiments on sacrificial layers subjected to blast loading. The sacrificial layers consisted of unit

cells of mild steel, showing a near-perfect plastic collapse behavior. The tests showed that the sacrificial layer design efficiently succeeded in protecting the main structure. A sandwich composite panel structure was proposed and tested for blast protection by Condon et al. [48]. It was found that the panel could not restrain the maximum deflection as well as the original alloy panel could, due to the deficiency in the inter-laminar strength of the sandwich panel.

Metal foam is another choice of sacrificial material for blast protection due to its considerable energy absorption capability relative to its low density, a characteristic that is very preferable for light-weight applications. Aluminum foams have already been widely used for crashworthiness designs in today's automotive industry. The porous nature of the foam helps in heat dissipation and also provides acoustic damping. In a design handbook for metal foams [49]; it was shown that the foam is exploited as an energy absorber by mounting a heavy buffer plate in front of it. The blast impulse first accelerates the buffer plate and the kinetic energy acquired by the plate is dissipated by the foam. Gama et al. [50] performed both experimental and FE analysis showing that aluminum foam can delay and attenuate stress waves.

In this research, aluminum foam is utilized in the underbody armor structure of a military vehicle, taking into consideration the major requirements for the advanced vehicle armor structure as stated previously. The profile of the armor structure is designed considering blast loading uncertainties; weight savings are achieved without debasing the blast protection capabilities of the underbody armor structure.

An undesired phenomenon observed when using a cellular material, such as

aluminum foam, for blast protection is that, under certain conditions, the force transmitted to the protected structure can be even higher than when the cellular material is not used. This unexpected phenomenon, the so-called "force enhancement," has been mentioned in several published pieces. The initial framework for investigation of force enhancement phenomenon was established by Monti [51] as early as 1970. Gel'fand [52] first demonstrated pressure amplification by foam material using the experimental method, noting that the amplification might be the result of a transfer of momentum that took place during the full compaction of the foam. The stress or force enhancement phenomenon was observed by Reid et al. [53] [54] in wood and packed ring systems, and by Song et al. [55] in plastic foams. Skew et al. [56] demonstrated a substantial increase in the back wall pressure when a slab of porous polyester and polyether foams was mounted to the back wall of a shock tube. Mazor et al. [57] and Ben-Dor et al. [58] found that the actual blast pressure acting on the structural surface is a function of the response of the surface itself, since this influence the states of the gaseous phase. They studied the phenomenon of a planar shock wave colliding head-on with, and interacting with, open-cell polyurethane foam. Using analytical models and shock-tube experiments they found that the pressure developed at the end wall of the shock tube was increased after introducing foam. From this they concluded that cellular materials act as pressure amplifiers. They also referred to results by Skews et al. [56], however, which showed that the impulse transferred to the end wall of the shock tube was identical to that which was transferred without a sacrificial layer of foam.

Hanssen et al. [59] conducted full-scale free-field blast-loaded pendulum tests; an increase of the swing angle of the blast-loaded pendulum was observed when a foam panel was attached. Hanssen attributed this angle (energy) increase to the continuous transformation of the shape of the initially planar panel surface into a concave shape during the blast. Ouellet [60] conducted both shock tube experiments and free-field blast trials on three polymeric foams of varying thickness and density, and concluded that three different regimes of amplification and attenuation of foam transmitted overpressure can be identified.

Numerical simulation by Olim et al. [61] based on a two-phase flow model (a dust-gas model) supported the experimental results of Skew et al. [56]. This model treats the solid phase as suspension dusts in the gas phase. This is applicable to foam of low density. Li and Meng [62] attributed the stress or force enhancement of cellular material to the formation of a shock wave when a critical impact velocity is reached for intensive loads. They showed that stress enhancement may occur during its propagation through a cellular material. This was demonstrated using a one-dimensional mass-spring model; dimensionless numbers of material properties and loading parameters were identified to give critical conditions for the transmitted force enhancement when a cellular layer was subjected to a blast pulse. Ma and Ye [63] [64] first considered the coupling effects of the foam claddings and the protected main structure using a one-dimensional analytical model.

Despite all these efforts, no published work has been found that gives a detailed explanation of this force enhancement phenomenon; the physical background of this

phenomenon still needs to be discovered. Due to the lack of theoretical support, no practical solutions have been proposed to prevent this undesired phenomenon from happening. As a result, application of cellular material for blast protection design is still limited at the present time.

In this research, the root cause of the force enhancement phenomenon when using a cellular material, such as aluminum foam, for blast protection is thoroughly investigated and understood. The force enhancement is found out to be due to the mismatches of the mass density and the stiffness between the cellular material and the protected structure. Countermeasures are proposed to prevent the force enhancement as will be discussed in detail in Chapter VI.

1.4 Motivation and Research Objective

Based on the above discussion, it is concluded that current structural crashworthiness and blast protection designs present very difficult and complicated challenges, with the following challenges still remaining:

First, an advanced systematic approach has not been developed to treat generalized crashworthiness or blast protection design problems;

Second, it is still a difficult task to get a reliable optimal design for structural crashworthiness or blast protection, i.e., uncertainties have not been systematically considered in crashworthiness and blast protection design problems;

Third, there is a disconnection between the structural design and the material design;

Fourth, considering other multidisciplinary objectives beside crash-related

objective makes a design problem cumbersome and even more challenging to be solved;

And finally, applications of advanced topology optimization techniques in this area are still limited to a few simplified problems.

The objective of this research is to address these challenges in support of future ground vehicle programs with a focus on crashworthiness and blast protection designs. This research is devoted to developing an advanced systematic approach for crashworthiness and blast protection designs of general engineering structural and material systems.

1.5 Dissertation Organization

The remainder of this dissertation is organized as follows:

Chapter II presents the developed magic cube (MQ) approach. Three major dimensions of the MQ: *decomposition*, *design methodology*, and *general consideration* are laid out. Three different layers of each major dimension are introduced and explained.

Chapter III demonstrates the implementation of the MQ approach in solving a complicated system-level crashworthiness design problem.

In Chapter IV, the MQ approach is employed to solve two industry application problems: the elastomeric mounting system (EMS) design and the design for weight reduction of a vehicle system via material substitution.

In Chapter V, the MQ approach is employed to assist a complicated blast protection design of a military vehicle system.

Chapter VII focuses on a detailed investigation of the so called “force enhancement” phenomenon when using metal foams to alleviate blast effects. The root cause of this phenomenon is identified for the first time. A countermeasure design concept of an interim isolating (I-I) structure between the foam and the protected structure is introduced. An application example is given as a demonstration.

Finally, Chapter VIII concludes the dissertation, and summarizes the contributions with suggested future work.

CHAPTER II

The Magic Cube Approach

2.1 Crashworthiness Design of a Thin-walled Tube

Most of the crash energy absorption structures in modern vehicles are made with thin-walled sections because of their high energy-absorption capabilities. Let's consider a simple crashworthiness design problem of a thin-walled square tube, which can represent a typical configuration of stamped component in real vehicles. A piece of reinforcement with an X-shaped cross section is attached inside the tube to help absorb the crash energy. Note that the reinforcement is employed here for demonstration purposes and its topology configuration is subjected to change in a later design stage; also note that the reinforcement may be composed of a different type of material than the thin-walled tube itself.

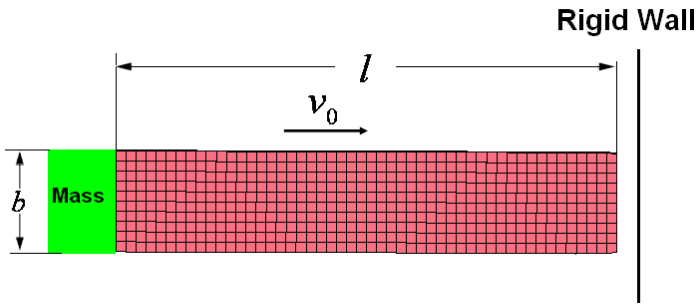

(a)

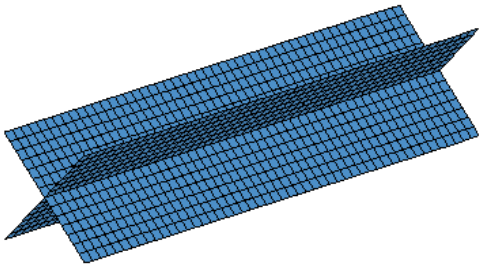

(b)

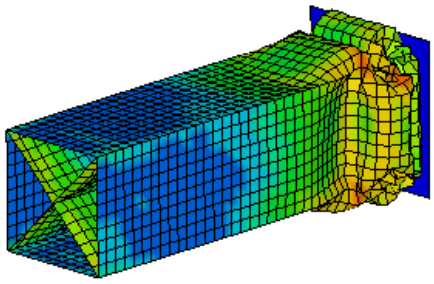

(c)

Figure 2.1: Thin-walled tube with reinforcement crashes into a rigid wall: (a) finite element model and geometrical dimensions; (b) inner reinforcement; and (c) simulation result.

The square tube has the geometry of width b, length l, and wall thickness t. The finite element model of the system has been developed as shown in Fig. 2.1a. Figure 2.1b shows the configuration of the reinforcement with the X-shaped cross section, attached to the inner of the tube. A total mass of m is added to the rear end of the tube to represent the inertia force from the attached vehicle structure. The initial velocity is v_0 and the tube crashes into a rigid wall that is considered to have infinite mass. A snapshot of the simulated deformation of the system after crash is depicted in Fig. 2.1c, using the non-linear, explicit FE code LS-DYNA.

2.2 Space Decomposition

Consider a design problem with the objective of maximizing the energy absorption of the reinforced thin-walled tube system during the whole crash process.

The total weight of the system, including the tube and the reinforcement, is considered to be constrained to a certain value, representing a limited amount of material usage.

The total energy absorption of the system during the whole crash process is denoted by $E_{\mathbf{sys}}$; we have

$$E_{\mathbf{sys}} = E_{\mathbf{tube}} + E_{\mathbf{ref}} \tag{2.1}$$

where $E_{\mathbf{tube}}$ is the energy absorption of the thin-walled square tube; and $E_{\mathbf{ref}}$ is the energy absorption of the reinforcement, during the whole crash process, respectively. In order to maximize the total energy absorption, one needs to maximize both $E_{\mathbf{tube}}$ and $E_{\mathbf{ref}}$, while due to the constraint on the total weight of the system, $E_{\mathbf{tube}}$ and $E_{\mathbf{ref}}$ cannot be maximized simultaneously.

To conduct the design effectively, one idea is to decompose the whole system into two subsystems (components) in space, which are, in the current case, the thin-walled square tube and the inner reinforcement, respectively. The optimal (target) energy absorption of each subsystem (component) can be determined by the following optimization problem, resulting in a target cascading process:

Find the vector

$$\{\mathbf{x}\} = \{E_{\mathbf{tube}}, E_{\mathbf{ref}}\}^T$$

such that

$$\begin{aligned} &\underset{\mathrm{x}}{\text{Maximize}} \quad E_{\mathrm{sys}} \\ &\text{Subject to} \quad \mathrm{W}_{\mathrm{tube}} + \mathrm{W}_{\mathrm{ref}} \le \mathrm{W}_{\mathrm{cons\_total}} \end{aligned} \tag{2.2}$$

where W_{tube} (W_{ref}) denotes the weight of the tube (reinforcement), which is correlated to the energy absorption of the tube (reinforcement); and W_{cons_total} is the constrained total weigh of the system.

Once the optimal (target) energy absorption of the tube and the reinforcement are determined, design processes can be initiated for each subsystem to meet the respective obtained design targets.

With this simple design problem, we have demonstrated the basic concept of *space decomposition* in crashworthiness design. The *space decomposition* approach can be applied to the crashworthiness design of a system, such as an automotive vehicle system, that is much more complicated than the system in the example design problem. In general, due to the complexity of a vehicle system, it is usually difficult to handle a design problem in system level directly. With *space decomposition*, a vehicle system can be decomposed into subsystems and further into components; in this way, a design problem is greatly simplified by cascading system-level design objectives into subsystem-level and component-level design objectives. A target cascading process needs to be carried out to obtain the subsystem-level and component-level design targets. Figure 2.2 demonstrates the implementation of *space decomposition* and target cascading in a pickup truck vehicle system design problem: the vehicle system is decomposed into various subsystems and further into different components; the design target for each component is achieved with detailed design; backward substitutions give designs that meet the subsystem-level design targets, and finally, a design that meets the system-level design objective is obtained.

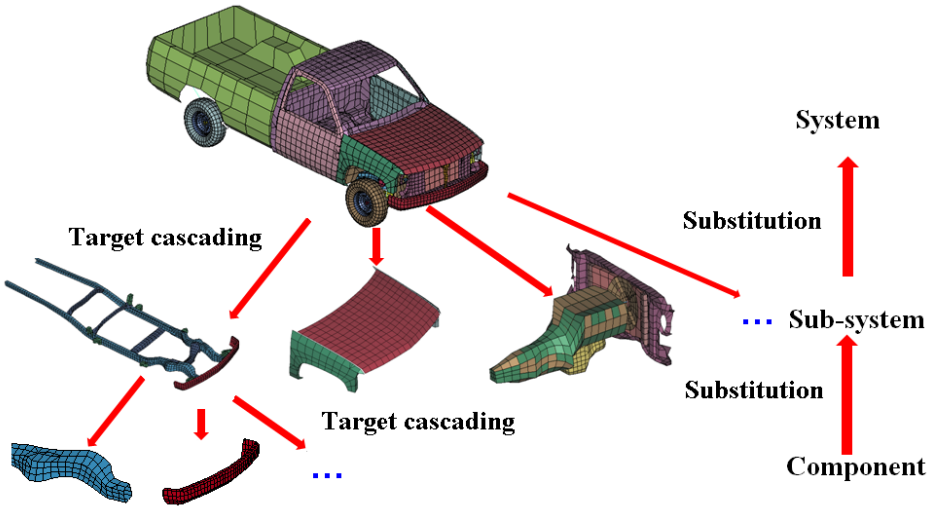

Figure 2.2: Demonstration of space decomposition and target cascading in a pickup truck design problem

2.3 Time (Process) Decomposition

Let's consider another case when only the rear segment of the thin-walled square tube is reinforced, to assure the rear segment does not collapse before the front segment of the thin-walled square tube. The crash force history of the baseline design is depicted in Fig. 2.3. An abrupt jump in crash force occurs at crash time t_1. This results from the reinforcement coming into contact with the rigid wall. A crash force level of F_{target} is set as the target. The design objective in the current problem is to "push" the crash force toward this target force level, aiming to achieve a constant deceleration of the mass attached at the rear end of the tube.

For conducting the design, the whole crash process of the reinforced thin-walled tube system is decomposed into two consecutive crash scenarios as depicted in Fig 2.3. The first scenario takes place from crash time t=0 to $t = t_1$; during this period, only the front segment of the thin-walled tube is crushed. The second scenario is

defined to take place from $t = t_1$ to $t = t_2$, when both the rear segment of the tube and the inner reinforcement are crushed. With the *time (process) decomposition* approach, the original design target is cascaded into two sub-targets, each associate with a specific scenario.

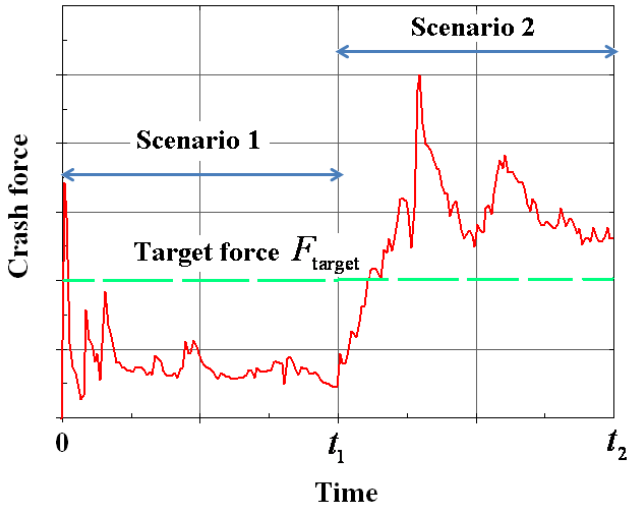

Figure 2.3: Demonstration of time decomposition of the crash force history

Based on *time (process) decomposition*, the *space decomposition* approach is employed to decompose the reinforced thin-walled tube system, this time, into two subsystems (components) as shown in Fig. 2.4.

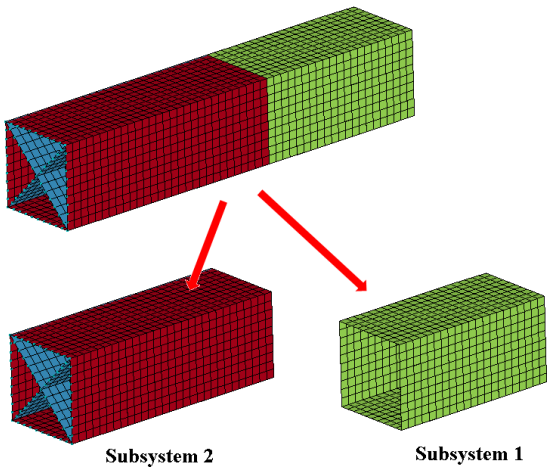

Figure 2.4: Space decomposition of the reinforced thin-walled tube system

The analysis model for the first scenario design is based on Subsystem 1 as shown in Figure 2.4. Appropriate boundary and loading conditions need to be applied to the model of Subsystem 1 to ensure that its crash behavior is similar to that of the system model. The design target for the first scenario is achieved by solving the optimization problem:

Find the wall thickness of the tube $t_{\mathbf{tube}}$

such that

$$\begin{aligned} &\underset{t_{\text{tube}}}{\text{Maximize}} \quad E_{0\sim t_1}(t_{\text{tube}}) \\ &\text{Subject to} \quad F_{\max}(t_{\text{tube}}) \le F_{\text{target}} \\ &\qquad\qquad \underline{t}_{\text{tube}} \le t_{\text{tube}} \le \bar{t}_{\text{tube}} \end{aligned} \tag{2.3}$$

where $E_{0\sim t_1}$ is the absorbed energy of Subsystem 1 during the crash time span of 0 to t_1. $F_{\max}(t_{\mathbf{tube}})$ is the maximum crash force developed during this time span. A similar optimization problem can be formulated and solved to achieve the design target for the second scenario. Once the design target for each crash scenario is achieved, the combined result will yield a design that meets the design objective over the whole

time span. Note that all above optimization problems may not be rigorously defined; they are employed only to demonstrate the proposed decomposition approaches.

With this design case, we have demonstrated the basic concept of *time (process) decomposition* in crashworthiness design. The *time (process) decomposition* approach can be applied to the crashworthiness design involving a process, such as an automotive vehicle crash, that is much more complicated than the crash process in the example design problem. In general, *time (process) decomposition* decomposes a crash process into consecutive crash scenarios, and further into sub-scenarios, in the time domain; the design target can be cascaded into each individual scenario and sub-scenario instead of handling the whole process all at once, thus simplifying the design problem. Figure 2.5 demonstrates the implementation of *time decomposition* in an example vehicle crash process: the crash process is first decomposed into two consecutive crash scenarios, each includes a high crash peak force, see Fig. 2.5a; secondly, in Scenario 1 design, the crash process during time 0 to 22 ms is further decomposed into two consecutive sub-scenarios, each with a local high crash peak force to deal with, see Fig. 2.5b. Note that the crash process should be divided into different crash scenarios and sub-scenarios based on the sequence of the physical phenomena occurring during the crash event, as well as the specific design objective. After the designs for each sub-scenario and each scenario have been completed with the cascaded design targets; a combined design is expected to meet the design target over the whole time span of the crash process.

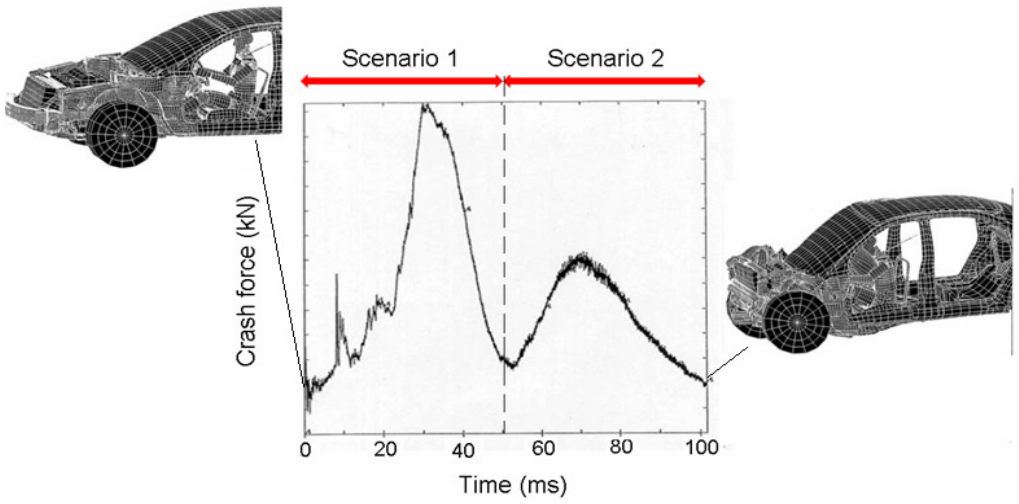

(a)

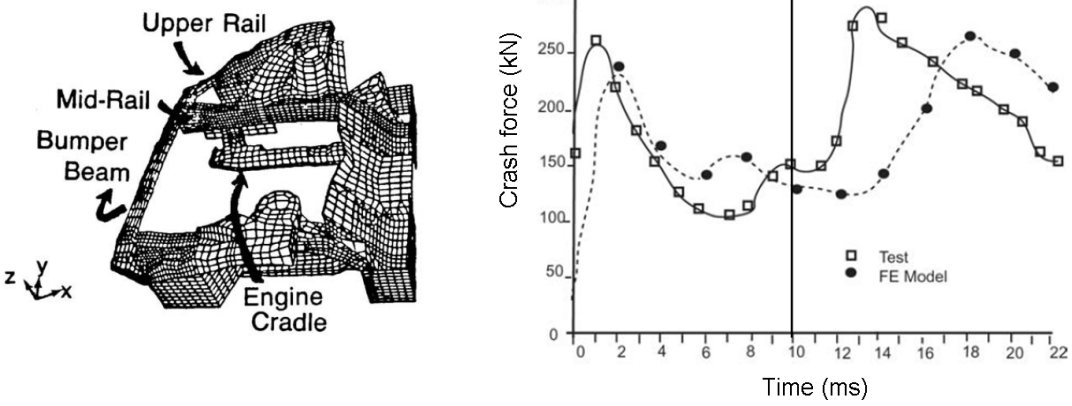

(b)

Figure 2.5: Demonstration of time decomposition of a vehicle crash process

2.4 Scale Decomposition

Again, consider the problem of a thin-walled square tube crashing into a rigid wall. It is noted that in the case of a zero degree impact, the peak crash force is developed at the very beginning of the crash process, as shown in Fig. 2.3. This peak force is undesirable in crashworthiness design. To eliminate this initial peak crash force, an engineering material concept is developed by distributing a

composite porous material to serve as a crash cushion at the frontal portion of this thin-walled tube. This composite material is designed to dissipate the initial peak crash force.

To study the material microstructure design for crashworthiness applications, one needs to investigate the relationship between the features of the material's microstructure and the generalized material properties. The functional relationship between microstructure dimensions and homogenized moduli was determined by Bendsøe and Kikuchi [25].

Consider a plane stress problem.

Assume

$$\sigma_{13} = \sigma_{23} = \sigma_{33} = 0 \tag{2.4}$$

Then, for an isotropic material, the remaining stresses are related to the in-plane strains by the relationship (note that E and ν denote Young's modulus and Poisson's ratio of the material, respectively).

$$\begin{Bmatrix} \sigma_{11} \\ \sigma_{22} \\ \sigma_{12} \end{Bmatrix} = \frac{E}{1-\nu^2} \begin{bmatrix} 1 & \nu & 0 \\ \nu & 1 & 0 \\ 0 & 0 & 1-\nu \end{bmatrix} \begin{Bmatrix} \varepsilon_{11} \\ \varepsilon_{22} \\ \varepsilon_{12} \end{Bmatrix} = \begin{bmatrix} E_{1111} & E_{1122} & 0 \\ E_{2211} & E_{1111} & 0 \\ 0 & 0 & E_{1212} \end{bmatrix} \begin{Bmatrix} \varepsilon_{11} \\ \varepsilon_{22} \\ \varepsilon_{12} \end{Bmatrix} \tag{2.5}$$

A unit cell of the form shown in Fig. 2.6 was assumed. The microstructure consists of an isotropic material with a symmetric hole (dimension a) in the center. The so-called density, μ, of the unit cell is defined by

$$\mu = 1 - a^2 \tag{2.6}$$

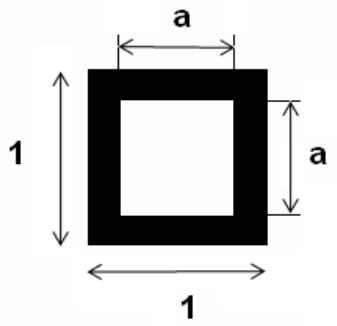

Figure 2.6: Plane stress unit cell [25]

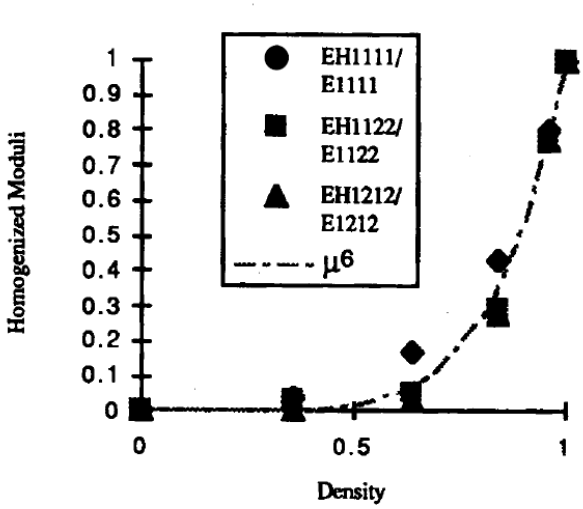

Figure 2.7: Curve fits for homogenized moduli [25]

The homogenized moduli for six different hole-sizes for $\nu = 0.3$ are shown in Fig. 2.7. A μ^6 curve was chosen to approximate the moduli as functions of density, with the figure showing very good agreement.

$$E^H_{1111} = E_{1111}\mu^6 = \frac{E}{1-\nu^2}\mu^6 \tag{2.7}$$

$$E^H_{1122} = E_{1122}\mu^6 = \frac{\nu E}{1-\nu^2}\mu^6 \tag{2.8}$$

$$E^H_{1212} = E_{1212}\mu^6 = \frac{E}{1+\nu}\mu^6 \tag{2.9}$$

The unit cell given in Fig. 2.6 was then considered for the elastic-plastic case. Consider the difference between a unit cell with a hole and a unit cell without a hole.

If stress concentrations around the corners are ignored, then the area of the small section will determine when yielding will occur as shown in Fig. 2.8.

Yielding is approximated by assuming that the small section will predict the onset of yielding for the unit cell with a hole, and is given by:

$$\sigma^{H} = \sigma_{y}(1-a) = \sigma_{y}\left(1-\sqrt{1-\mu}\right) \tag{2.10}$$

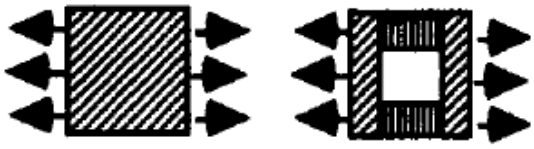

Figure 2.8: Yielding in unit cell with and without a hole [25]

Now, for the thin-walled tube crashing design problem, in order to eliminate the initial peak crash force, layers made of composite materials with different hole- sizes in the unit cells are distributed at the frontal end of the tube as shown in Fig. 2.9. The design objective is to maximize the crash energy absorption while constraining the level of the initial peak crash force.

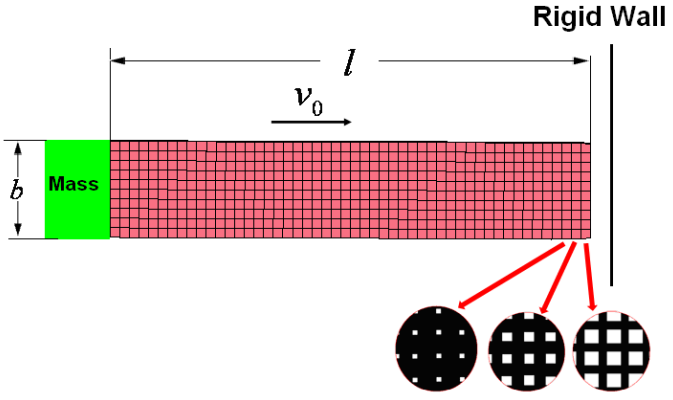

Figure 2.9: A composite material design model for initial peak crash force reduction

The optimal (target) properties of each single layer of composite material (meso-structure) can be obtained through the following optimization problem:

Find the vector

$$\{\mathbf{x}\} = \{E_1^H, \sigma_1^H, E_2^H, \sigma_2^H, \ldots, E_i^H, \sigma_i^H\}^T$$

such that

$$\begin{aligned} &\underset{\mathbf{x}}{\text{Maximize}} \quad E_{0\sim t_f}(\mathbf{x}) \\ &\text{Subject to} \quad F_{\max}(\mathbf{x}) \le F_{\text{target}} \end{aligned} \tag{2.11}$$

where E_i^H and σ_i^H denotes the homogenized modulus and the homogenized yield stress of the i-th layer in the frontal end of the crash tube, respectively. $E_{0\sim t_f}$ is the absorbed energy at the final time, t_f. $F_{\max}(\mathbf{x})$ is the maximum crash force developed during this time period, which is constrained by the target force level, F_{target}.

Once the optimal (target) homogenized modulus and yield stress for each composite material layer (meso-structure) are obtained, they can be further cascaded into the target properties of a single unit cell of the composite material (microstructure). This material design target cascading process is based on the decomposition of the composite material in various scale levels, the so-called *scale decomposition*. *Scale decomposition* can be viewed as a special case of the *space decomposition*, through which a structural material is decomposed into its meso-structure and further into its microstructure, to seek optimal solutions. For a crashworthiness or blast protection design problem, the *scale decomposition* approach helps to expand the search domain for an optimal solution from the structural design fields into the (composite) material design fields, and it is expected to help in searching for a more attractive solution to the design problem.

2.5 Target Cascading Process

Each of the three decomposition approaches developed above requires the corresponding target cascading process as discussed. For the *space decomposition*, the process is to cascade the system-level design target into the subsystem-level design targets, and further into component-level targets. For the *time (process) decomposition*, the process is to cascade the design target for the whole crash process into the design targets of a sequence of time-dependent (process-dependent) crash scenarios. And for the *scale decomposition*, the process is to cascade the design target of a structural material into the design targets of its meso-structure and eventually the microstructure.

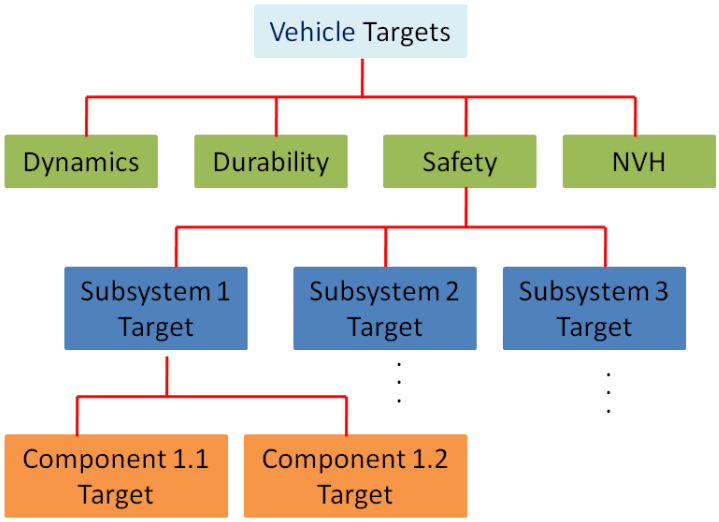

Figure 2.10: Target cascading in a vehicle design

Figure 2.10 demonstrates the target cascading process in a vehicle design problem. The vehicle-level design targets are first cascaded into targets of various disciplines, including vehicle dynamics, durability, noise, vibration and harshness

(NVH), and safety. The safety design targets, or targets from any other discipline, can be further cascaded into the design targets of the various subsystems, with each subsystem's design targets eventually cascaded into the design targets of its components. Through such a target cascading process, a design problem in the vehicle level can be divided into design problems of the subsystems and components with the cascaded sub-targets. These sub-design problems can be analyzed concurrently. This helps save time and reduces cost for product development.

Instead of addressing a real design problem of a vehicle system, the target cascading process is employed in this research to assist the realization of the three decompositions for the crashworthiness design problem, as shown above. Detailed analysis and application of the target cascading methods are outside of the scope of this dissertation.

2.6 Failure Modes Management

Consider the failure modes of the thin-walled square tube crashing into the rigid wall as shown in Fig. 2.1. For simplicity, the inner reinforcement is removed in the current case. The square tube has the geometry of width $b = 80$ mm , length $l = 400$ mm , wall thickness t=1.5 mm. A total mass of $m = 400$ kg is attached to the rear end of the tube; and the initial velocity of the tube is $v_0 = 30$ mph . Two cases are simulated using LS-DYNA: case one is a zero degree impact, and case two is with the rigid wall inclined by 11 degrees in the X-Z plane. The deformed shapes of the tube in the two cases are shown in Fig. 2.11a and 2.11b, respectively. In case one, the tube fails by progressive collapse along its axis; while in case two, the tube

fails by global bending collapse through the plastic hinge formed at the rear end of the tube where the stress is concentrated. Figure 2.11c depicts the crash force histories in the two cases: case 1 features a constant level of crash force throughout the whole crash process with cyclic oscillations; in case two, however, the crash force drops to zero at crash time t=8 ms due to the bending collapse mode. Figure 2.11d further compares the energy absorption histories in the two cases; with the progressive collapse mode (case one), the tube absorbs more than twice the energy as is absorbed with the global bending mode (case two).

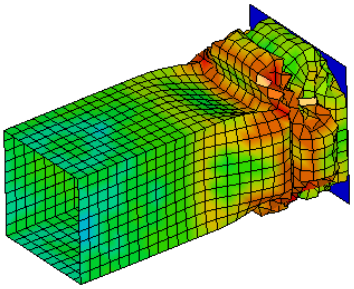

(a)

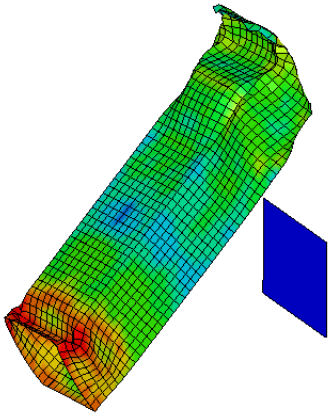

(b)

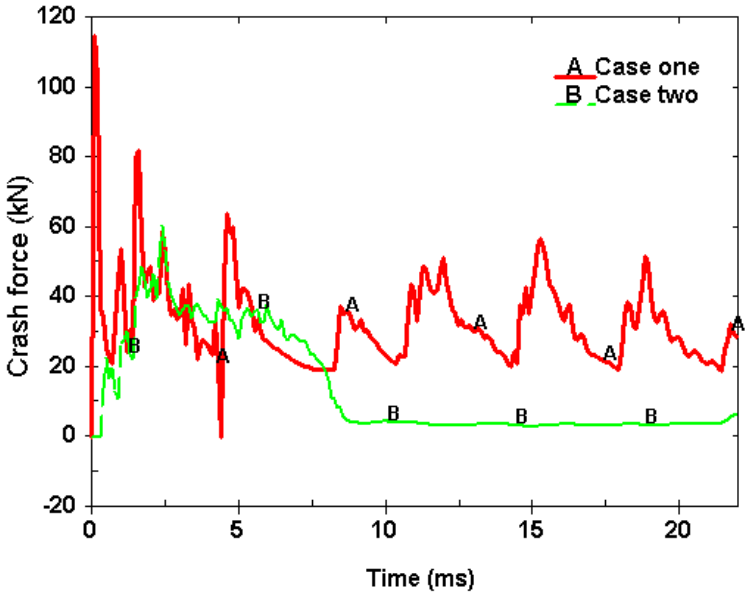

(c)

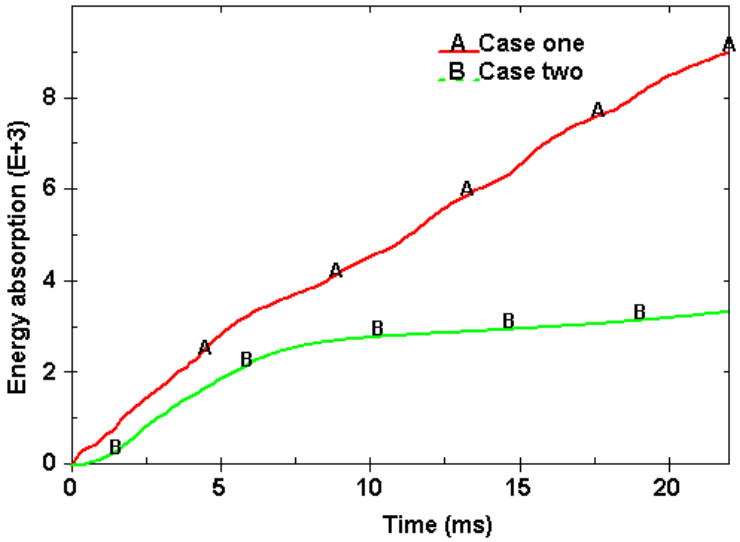

(d)

Figure 2.11: Crashing of a thin-walled square tube into a rigid wall: (a) deformed shape of the tube in case one; (b) deformed shape of the tube in case two; (c) crash force histories; and (d) energy absorption histories.

This example is dedicated to show the effects of failure modes on a structure crash performance.

In crashworthiness design, failure modes that feature more energy absorption, such as the progressive collapse of the thin-walled tube, are usually preferred when

energy absorption is a design target. It is worth noting that in some circumstances, failure modes with less energy absorption, such as the global bending collapse of the thin-walled tube, are desired when the structures are not intended for energy absorption purposes. In fact, in a vehicle crash process, the behaviors of the energy absorption devices and other structures are very complicated. The behaviors involve non-linear phenomena, including impact, large deformation, buckling and yielding, fracture, as well as non-linear contact. In addition, geometry, material nonlinearities, and strain rate also have significant effects on the crash process. The task of the failure modes management is to trigger the appropriate failure modes of the structures during a crash process, according to the specific design requirements.

2.7 Optimization Techniques

As discussed above, the axial progressive collapse failure mode absorbs much more crash energy than the global bending collapse mode of the thin-walled tube. It has been shown in [65], that for a thin-walled tube with specific configuration and crash condition, there exists a critical angle of the rigid wall which the tube is crashed into; if the angle between the normal of the rigid wall and the axis of the tube is less than this critical angle, the tube will fail by progressive collapse; otherwise, the tube fails through the global bending collapse.

Consider a design problem of a thin-walled square tube crashing into a rigid wall as shown in Fig. 2.12. The rigid wall is skewed by an angle α in the X-Z plane and an angle β in the Y-Z plane, respectively.

Using LS-DYNA simulation, a critical angle of $\alpha = \beta = 6^\circ$ is identified for the

crash mode of the tube to transform from the progressive collapse to the global bending collapse. The design objective is to transform the failure mode of this thin-walled tube to the progressive collapse to increase the energy absorption, without changing the weight of the tube itself. To achieve this objective, structural optimization techniques should be employed.

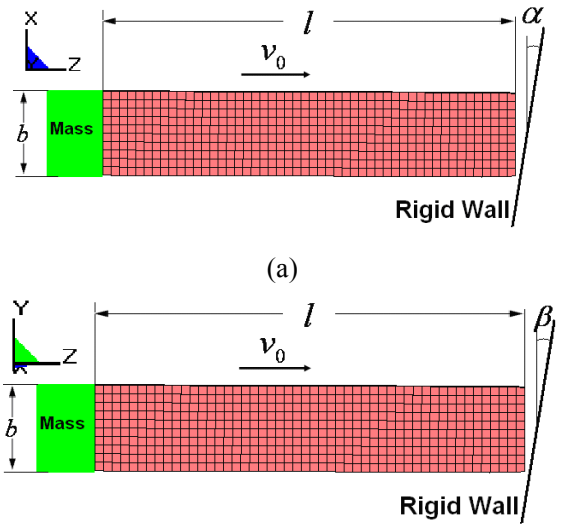

Figure 2.12: A thin-walled square tube crashes into a skewed rigid wall: (a) X-Z view; and (b) Y-Z view.

A direct stress management approach has been proposed to deal with a similar design problem [66], an approach that is essentially a trial-and-error method. In this research, a more advanced multi-domain multi-step topological optimization (MMTO) technique, based on the *time (process) decomposition* concept, is proposed. The MMTO technique provides a systematic process for material distribution in the structural domain with improved crashworthiness. The MMTO technique is employed to solve the current problem.

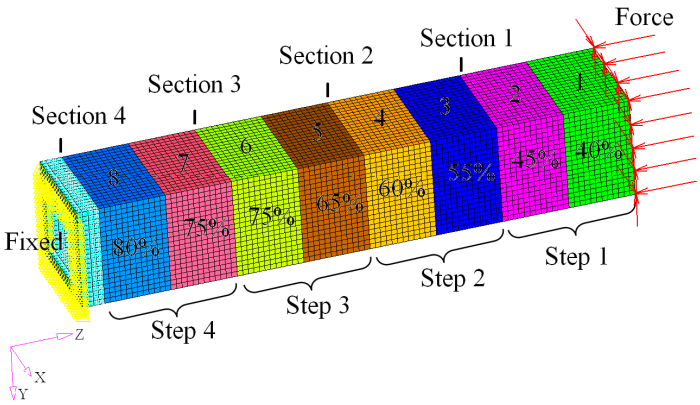

Figure 2.13: Sub-domains, design steps, and force output sections for multi-domain multi-step topology optimization

As shown in Fig. 2.13, the entire design domain is divided into eight sub-domains of equal length for topology optimization, and a non-design domain for applying the boundary condition. The material percentage is increased from the frontal to the rear end of the tube to ensure a sequential crash process of the tube, as well as to prevent the global plastic hinge from occurring at the rear end of the tube. The design process is divided into four steps in the current problem. In the first step, only sub-domains 1 and 2 are set as design domains. Distributed forces are applied to the front end of the tube to represent the crash load; three components of the forces are calculated based on the relevant angle of the tube to the rigid wall, i.e., $F_X = F_Z \tan\alpha$, and $F_Y = F_Z \tan\beta$. The design objective is to minimize the compliance of the tube under given loads. Design variables are the densities of the finite elements and the constraints are the volume (weight) fractions as set in the model shown in Fig. 2.13.

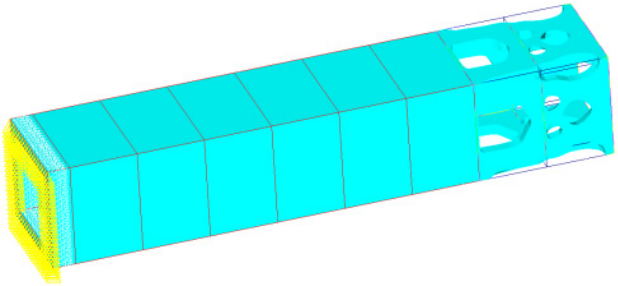

(a)

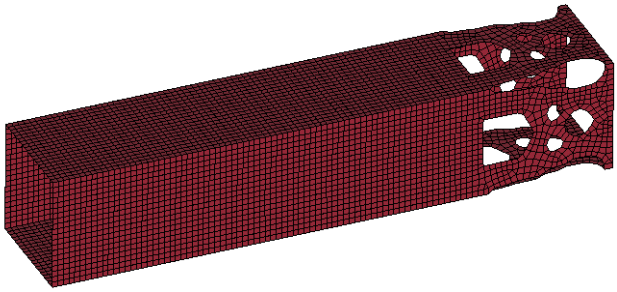

(b)

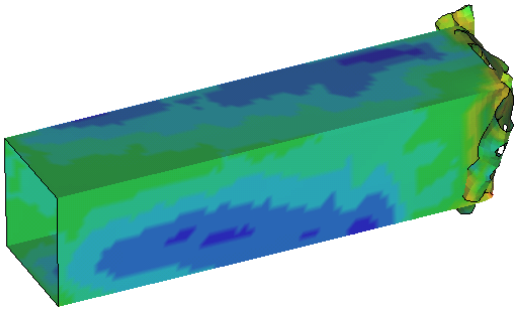

(c)

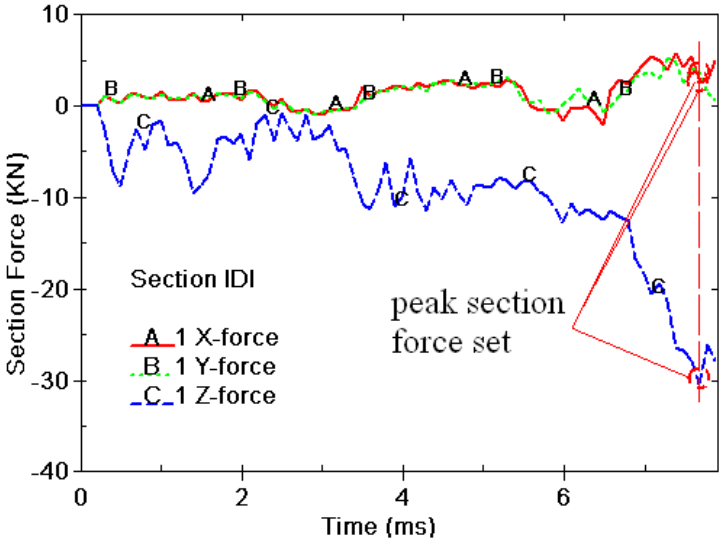

(d)

Figure 2.14: Topology design results after step 1: (a) density contour; (b) topological configuration; (c) deformation of the tube; and (d) section force history.

Figure 2.14a is the element density contour (topological configuration) after design Step 1. A FE model for crash simulation is constructed based on the topological configuration, as shown in Fig. 2.14b. Figure 2.14c shows the deformation of the designed tube, and Fig. 2.14d illustrates the force history of section 1 during the crash process. The peak section forces occur at the moment when the designed portion of the tube is totally crashed and the un-designed portion of the tube is yet to be impacted; these forces are to be used as the loads for Step 2 design.

The same process is applied in design Step 2, when sub-domains 3 and 4 are set as design domains. The structural topology of the final thin-walled square tube obtained from the MMTO process and the deformed shape of the tube after the crash are shown in Fig. 2.15a. It is seen that the tube with the designed topology fails through the progressive collapse mode as expected. To further improve the design, a reinforcing layer with a wall thickness that is much less than that of the original tube is attached to the tube with the designed topology, as shown in Fig. 2.15b. The reinforced tube with the designed topology fails through the progressive collapse mode as well, but with much improved crashworthiness. Figure 2.15c compares the crash force histories in various cases. It is seen that the tube with the designed topology features a more constant crash force as compared to the original tube, while the reinforced tube with the designed topology has a crash force that is even more constant, and two times than the tube with the designed topology. Figure 2.15d further shows energy absorption histories in different cases. It is seen that the tube

with the designed topology absorbs 10% more energy than the original tube, while the reinforced tube with the designed topology absorbs 86% more energy, with no increase in the amount of material used.

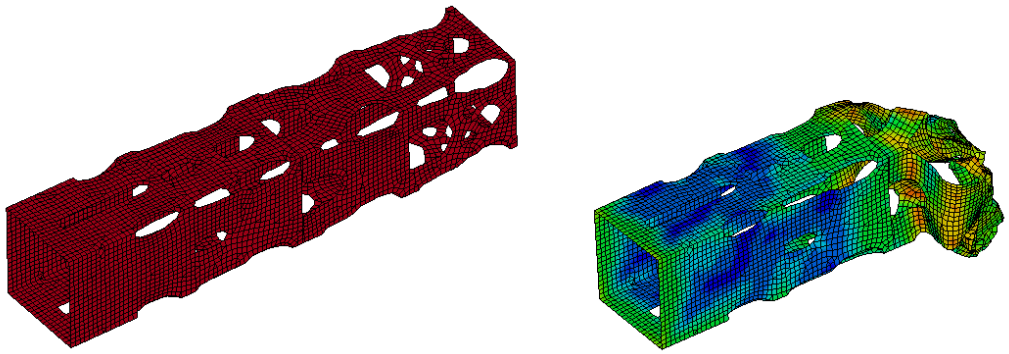

(a)

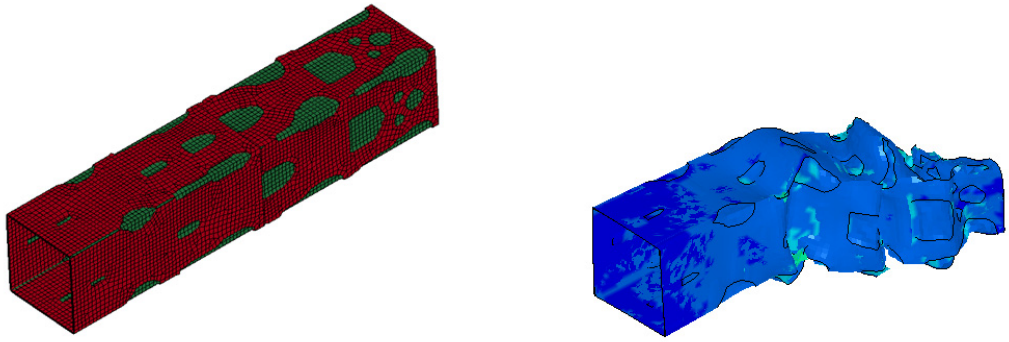

(b)

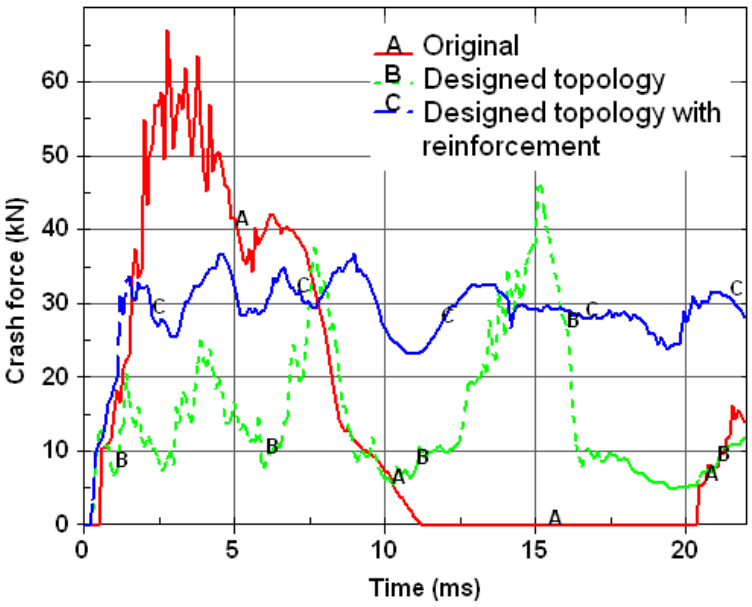

(c)

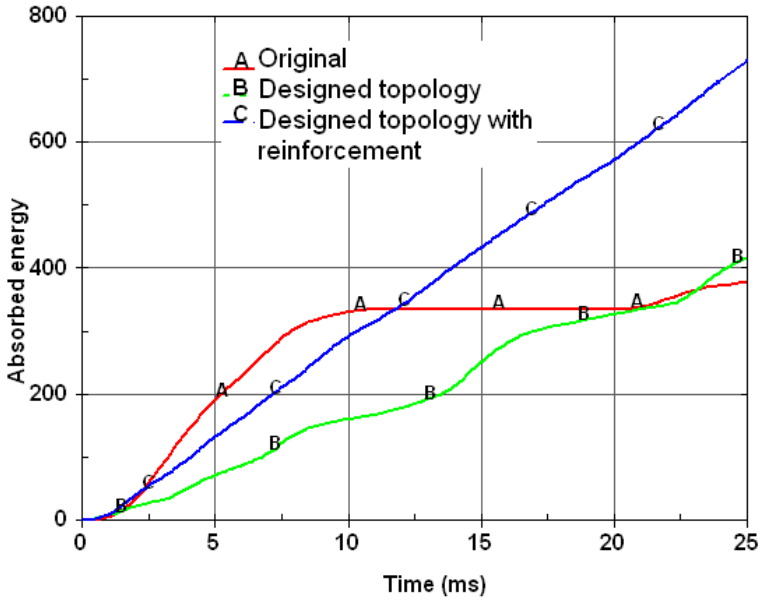

(d)

Figure 2.15: Final design results of a thin-walled square tube: (a) tube with designed topology ; (b) reinforced tube with designed topology; (c) comparison of crash force histories; and (d) comparison of energy absorption histories.

The general procedure of the MMTO is shown in Fig. 2.16.

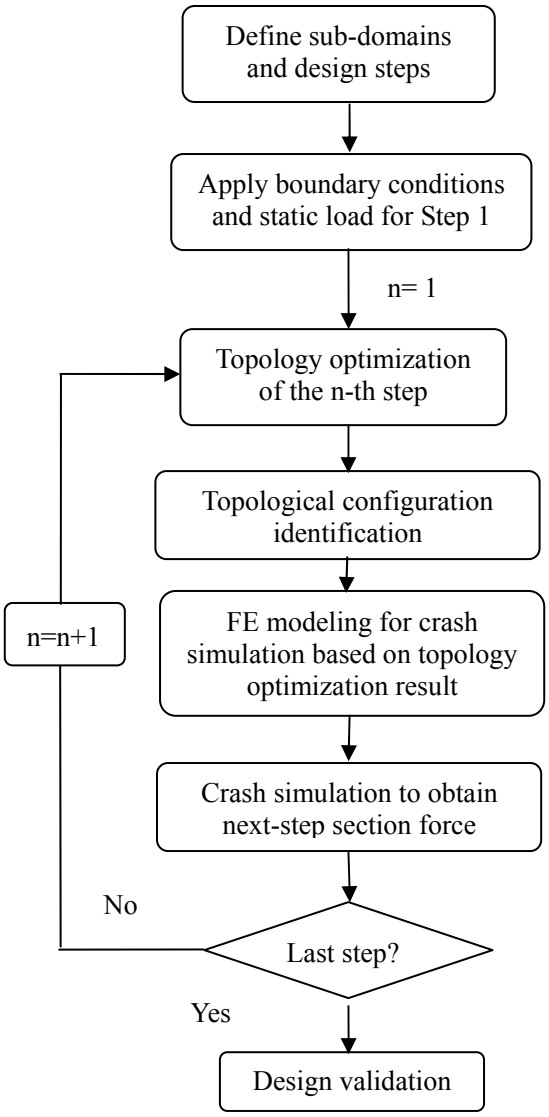

Figure 2.16: Procedure of multi-domain multi-step topology optimization

The MMTO is a representative optimization technique applied for the crashworthiness design. In general, the optimization techniques for crashworthiness design should include the selection of design objectives and constraints, selection of simulation (or approximation) models; determination of design variables (size, shape, or topology); and choosing of optimization algorithm for design space exploration, etc.

2.8 Multidisciplinary Objectives

The thin-walled square tube shown in Fig. 2.1 could be a simplified energy absorption component in a vehicle body structure. It is possible that this component is expected to meet other design requirements, such as stiffness, NVH, styling, in addition to the crashworthiness requirement. This results in a multidisciplinary design problem.

In a multidisciplinary design problem, it is critical to study the relationships (trade-offs) between all of the different objectives, and to handle them in one single design process. Based on a practical engineering design problem encountered in this research, we introduce a systematic approach called the objectives reduction approach (ORA) for the multidisciplinary design problem. It can be used to reduce the total number of the multidisciplinary design objectives in a practical structural optimization problem, without debasing the optimality of the final design, thus simplifying the design problem. The ORA can be explained as follows. First, a series of single objective optimizations (SOO) are conducted for all of the individual objectives in the design problem. Secondly, the resultant SOO designs are evaluated for all the other multidisciplinary objectives. Based on the evaluation results, we can divide the objectives into different groups. In the same group, the objectives are consistent with each other, but when they are in different groups, the objectives are in conflict. Finally, we can choose from each group a representative design objective. By emphasizing the representative objective, the other objectives in the same group can be then reduced, resulting in a much simpler design problem. The ORA is based

on the natural characteristics of an engineering structure in responding to different physical processes, so it can therefore be generalized for the same class of structural design problems including crashworthiness design goals. The general procedure of the proposed ORA is illustrated in Fig. 2.17. We will demonstrate the implementation of this approach through an example design problem of a real engineering system in Chapter IV.

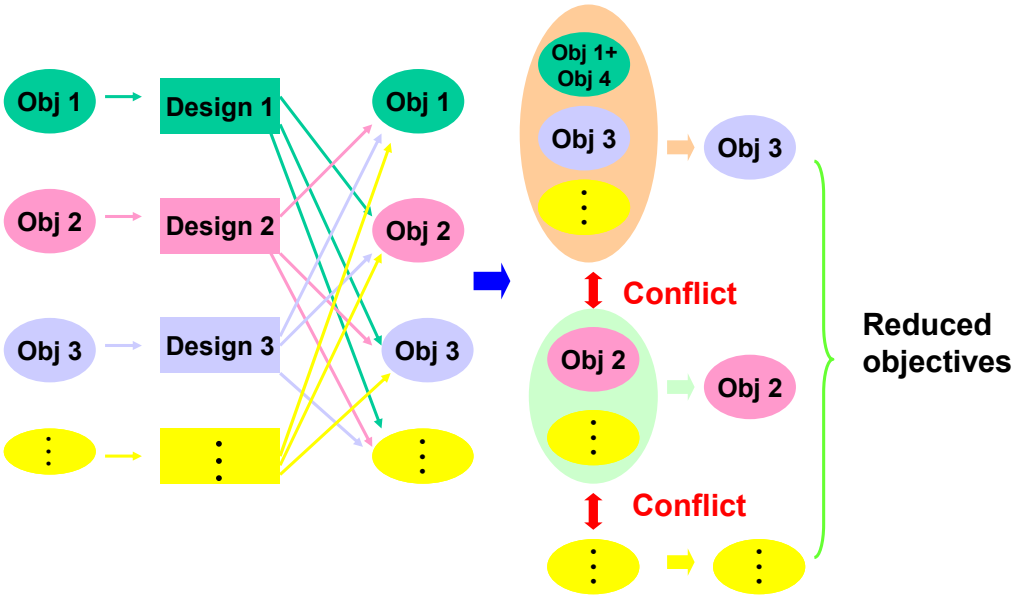

Figure 2.17: Objectives reduction approach

2.9 Loading Conditions

Dangerous loads on a vehicle system can be roughly divided into two categories: the crash loads and the extraordinary dynamic loads. The first category, depending on various crash scenarios, can include frontal (offset) crash load, side crash load, rear crash load, rollover crash load, etc. The second category is almost completely limited to military vehicle systems, and can include landmine blast load, ballistic

penetration load, etc. Compared to crash load, the blast load is much more intense with much shorter time duration. Despite this difference, design strategies for crashworthiness design can be extended to the blast protection design problem, because the major decomposition approaches developed in this research remain valid for the blast protection design problem. In this research, frontal crash load and blast loads from landmine explosions are considered in the design problems.

2.10 Uncertainties

Consider the thin-walled square tube crash problem another time. Assume the rigid wall is skewed in the X-Z plane by an angle of α as shown in Fig. 2.12a. The deformed shapes of the tube under different crash angles are shown in Fig. 2.18. The tube undergoes an axial progressive collapse mode if $\alpha \leq 8^{\circ}$. Eight degrees is the critical angle for the failure mode when the tube transforms from the progressive collapse to the global bending collapse. If there is more than one degree of uncertainty of the skewed angle of the rigid wall that is skewed by eight degrees, the actual deformation of the tube would be unpredictable. This means uncertainty in loading conditions can change the failure mode of a structure, resulting in a non-robust design.

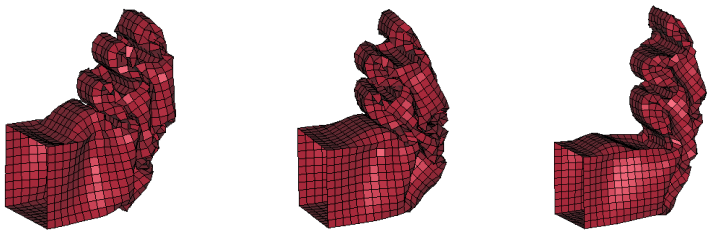

$\alpha = 4^{\circ}$ $\alpha = 6^{\circ}$ $\alpha = 8^{\circ}$

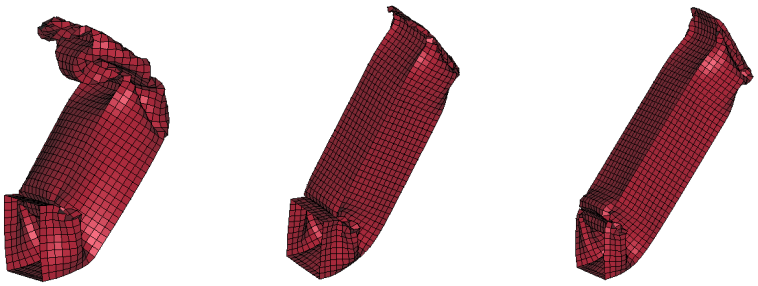

$\alpha = 9^{\circ}$ $\alpha = 11^{\circ}$ $\alpha = 13^{\circ}$

Figure 2.18: Deformed shapes of a thin-walled square tube under various crash angles

Consider the uncertainty of the boundary condition (B.C.) at the distal end of the tube: a fixed B.C. vs. a simple-supported B.C., as shown in Fig. 2.19a. In the case of $\alpha = 8^{\circ}$, the simple-supported B.C. changes the failure mode of the tube from the progressive collapse, as with the fixed B.C., to the global bending collapse, as shown in Fig. 2.19b.

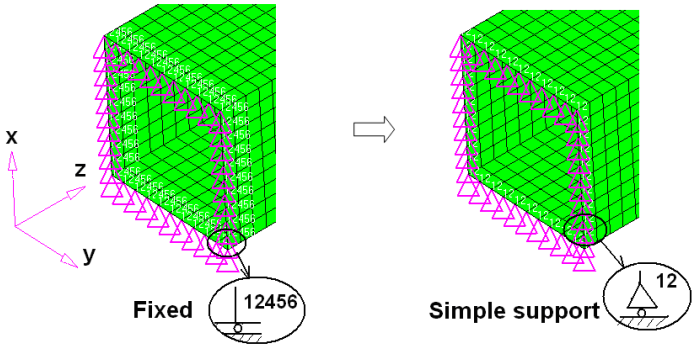

(a)

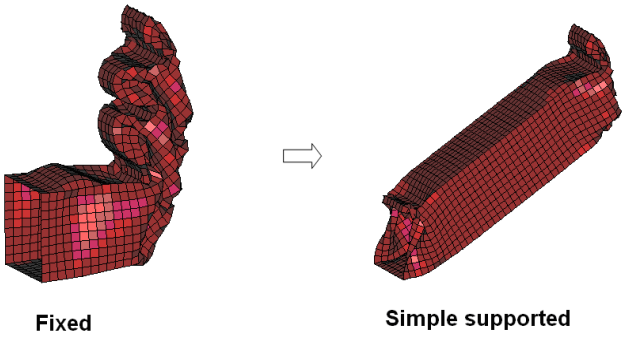

(b)

Figure 2.19: Effects of boundary condition uncertainties: (a) fixed vs. simple-supported; and (b) deformed shape of the thin-walled tube with different boundary conditions.

Consider another uncertainty of the B.C.: variation of the friction coefficient μ between the tube and the rigid wall. The crash force histories with three different values of μ are compared in Fig. 2.20. It is seen that the uncertainty of the friction coefficient can influence the level of the crash force.

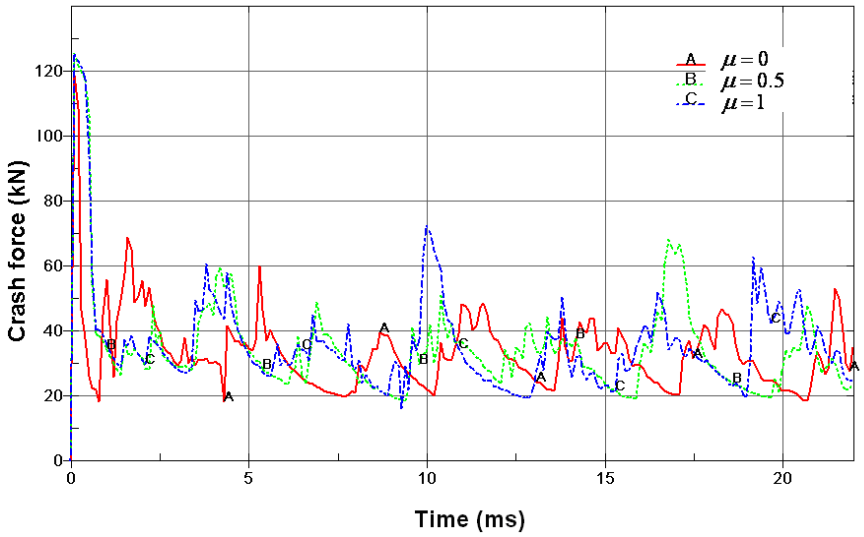

Figure 2.20: Crash force histories of a thin-walled tube with various friction coefficients

Through this example, we have demonstrated that uncertainties in boundary conditions may result in totally different responses of a structural component during a crash process.

The FE model of the thin-walled square tube includes a small imperfection (uncertainty) as shown in Fig. 2.21b. This artificially introduced uncertainty is critical for the model to predict the failure mode of the tube, as happens in a real-world test. Without this imperfection (uncertainty), a "perfect" FE model of the tube will yield an incorrect collapse mode of the tube as shown in Fig. 2.21a, in which all the side plates buckle outside, a mode would never happen in reality. In fact, the FE method is a numerical method in nature; it is usually difficult for such a method to

capture accurately the bifurcation point of a thin-walled structure without artificially introducing imperfections to the model.

(a)

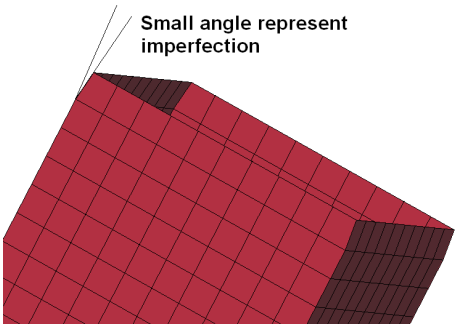

(b)

Figure 2.21: Modeling uncertainty: (a) incorrect collapse mode of the tube predicted by a "perfect" finite element model; and (b) introduction of imperfection (uncertainty).

In general, uncertainties in modeling come from information loss or form an inaccurate representation in the process of transforming a real engineering problem into a mathematical model. Another typical modeling uncertainty is related to the mesh size in the FE model. Figure 2.22 shows four levels of mesh size of the thin-walled square tube FE model. Figure 2.23 compares the crash force histories of the tube predicted by the FE models with various mesh sizes. It is seen that a coarse mesh (mesh level 1) gives a higher initial peak crash force and mean crash force level. As the mesh size decreases, the initial peak and the mean crash force level converge.

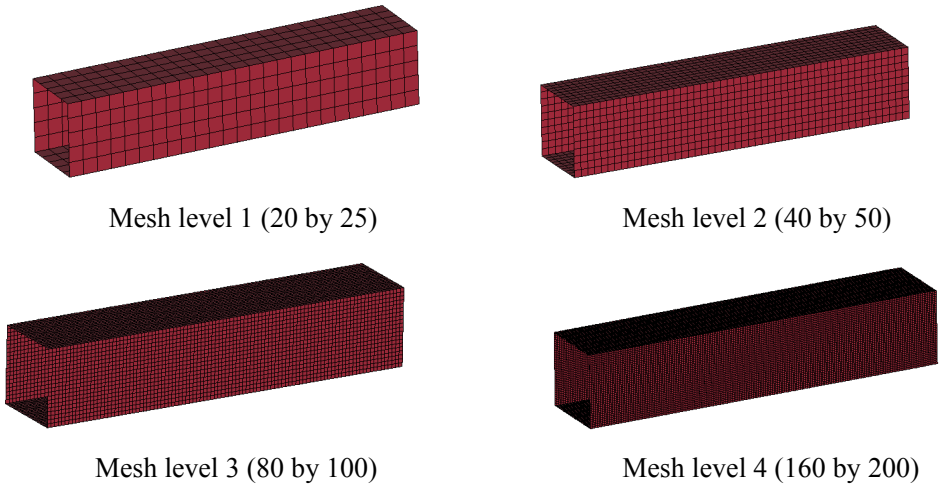

Figure 2.22: Mesh size variation of a thin-walled square tube finite element model

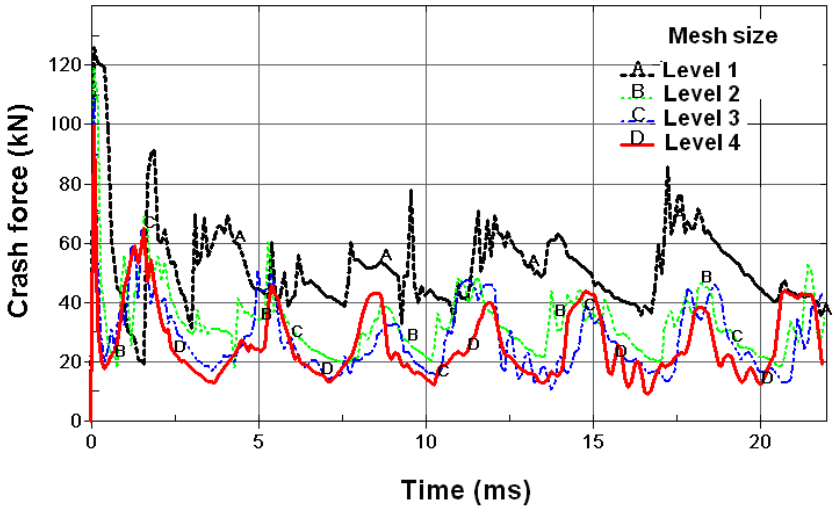

Figure 2.23: Crash force histories predicted by finite element modeling with various mesh sizes

We have shown through this example that uncertainties in the modeling process can affect the crashworthiness analyses.

For a design problem, considering uncertainties in the design process usually results in a more robust design result. This can be demonstrated through an example optimization problem of a test function with two input variables, as shown in Fig. 2.24. The test function is to be maximized in the design domain. It is noticed that there exist two different local maxima. The first one (point A) is higher in absolute

value, but among its nearby points, the function hardly drops. In contrast, the second local maximum (point B) has a lower value but is more stable when moving throughout the function domain. In other words, if uncertainties of the input variables are considered, the design at point B will give a more robust maximum of the function.

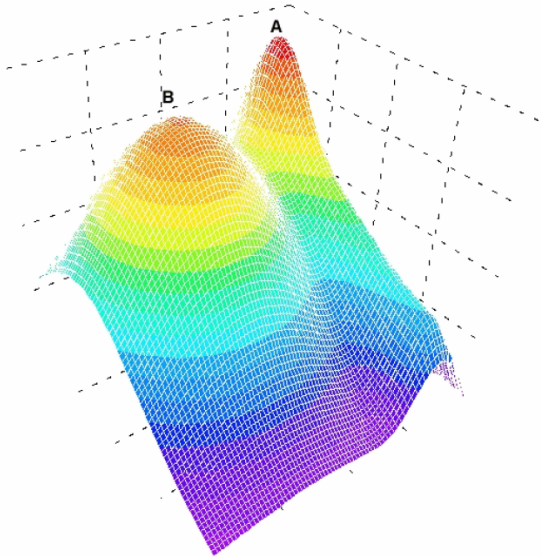

Figure 2.24: Considering uncertainties results in a more robust design

In crashworthiness design, unlike the case of the mathematical function optimization problem as above, an "optimal" design obtained under deterministic design conditions (without considering uncertainties) could behave in a completely different manner in the crash process when a critical parameter or condition of the system is changed (even if only slightly) due to the uncertainties. In other words, an optimal design may no longer be optimal if uncertainties in the system are considered. This has been previously demonstrated through the example thin-walled tube crash problem. In summary, uncertainties should be included in crashworthiness designs to achieve design robustness.

2.11 Summary

The objective of this research is to develop a generalized approach for vehicle crashworthiness and blast protection designs, to be employed in a systematic way to assist problem solving by integrating all aspects as discussed above. This objective is realized by an innovative Magic Cube (MQ) structure as shown in Fig. 2.25.

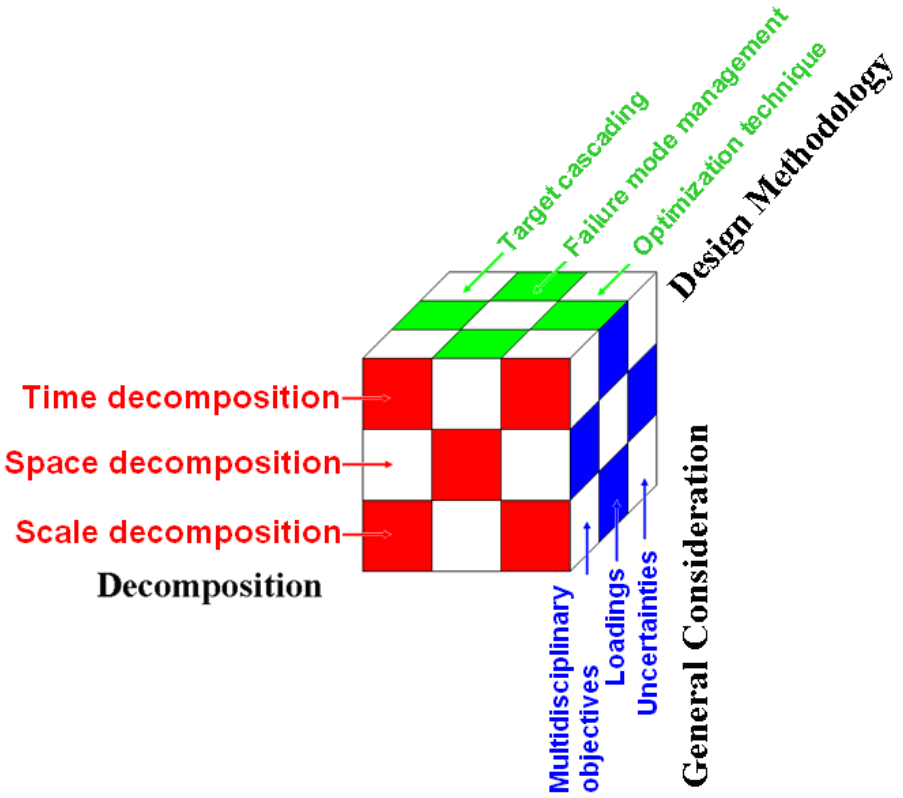

Figure 2.25: The magic cube (MQ) for crashworthiness and blast protection designs

The MQ consists of three major dimensions: *decomposition*, *design methodology*, and *general consideration*. The *decomposition* dimension includes the major decomposition approaches developed for the crashworthiness design problems, and it can be applied to the blast protection design problems. It has three layers: *time (process) decomposition*, *space decomposition*, and *scale decomposition*. The *design*

methodology dimension is related to the methodologies employed in the design process; three layers in this dimension are: *target cascading*, *failure mode management*, and *optimization technique*. The *general consideration* dimension has three layers, which are *multidisciplinary objectives, loadings,* and *uncertainties*. All these layers are coupled with each other to form a 27-element magic cube (MQ). A complicated crashworthiness or blast protection design problem can be solved by employing the appropriate approaches in the MQ, which can be represented by the corresponding elements of the MQ. The application of the MQ approach to general crashworthiness and blast protection problems are discussed in the following chapters.

CHAPTER III

Crashworthiness Design of a Vehicle System Using the Magic Cube Approach

In this chapter, the proposed Magic Cube (MQ) approach is employed on the crashworthiness design of a representative vehicle system; the aim is to show the feasibility and effectiveness of this approach in solving a complicated system-level crashworthiness design problem.

3.1 Problem Description

A representative vehicle is crashed (100% frontal) into a rigid wall at a speed of 35 mph. The finite element (FE) analysis is conducted to simulate the event using LS-DYNA, see Fig. 3.1a. It is obvious from Fig. 3.1b that there exist two large peaks in the crash force history curve predicted by the simulation; the second peak force is unacceptable because it results in a large cabin deceleration, with the potential of injuring the occupants as illustrated in Fig. 3.1c. An ideal crash force history curve is proposed which has a constant level during the whole crash process. An improved design is sought in the following to push the crash force toward this ideal curve, aiming to achieve a less severe cabin deceleration, thereby reducing

potential occupant injuries.

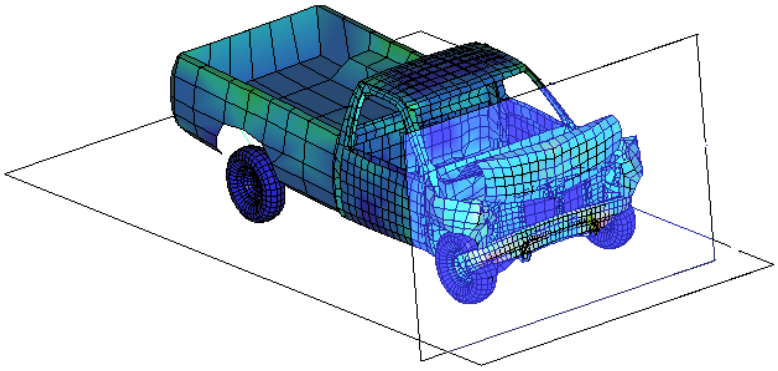

(a)

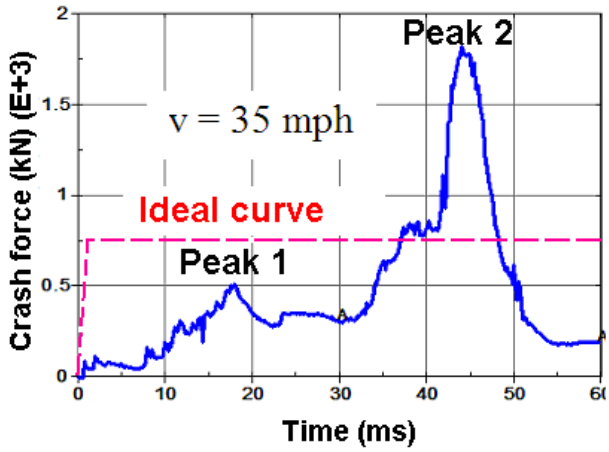

(b)

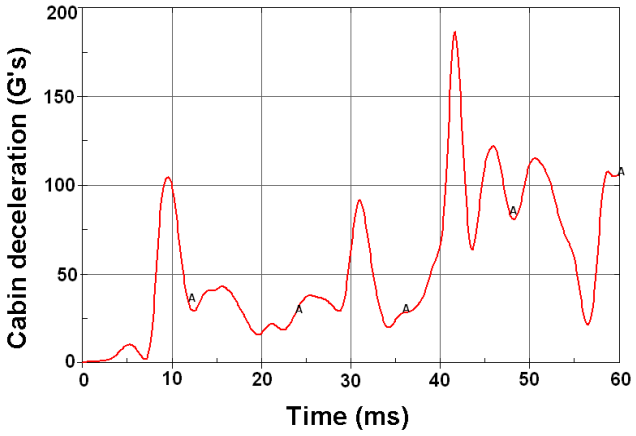

(c)

Figure 3.1: A vehicle system crashworthiness design problem: (a) finite element simulation of the vehicle crash; (b) crash force history and ideal curve for design improvement; and (c) cabin deceleration history.

3.2 Implementation of Time Decomposition

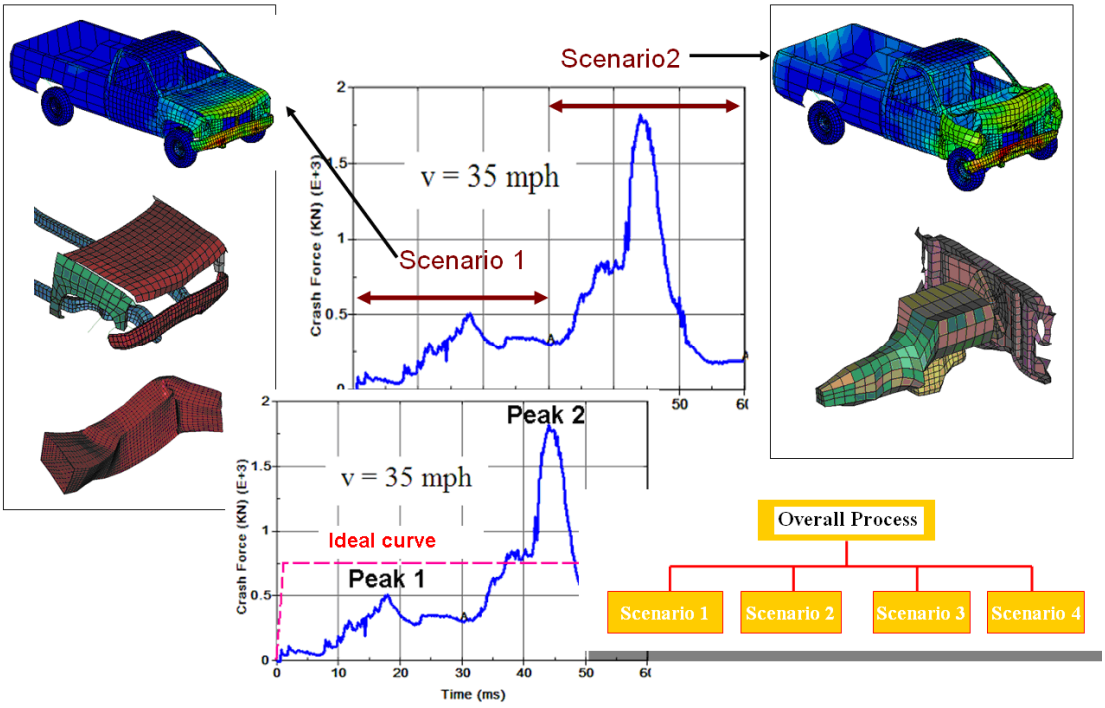

Figure 3.2: Time decomposition of the vehicle crash process at the system level

The *time decomposition* approach is first employed to simplify the design problem. As shown in Fig. 3.2, the overall crash process is decomposed into two major scenarios; the first scenario includes the peak force at $t = 17$ ms, and the second scenario includes the peak force at $t = 44$ ms. It is found from the FE analysis that the peak force in the first scenario is associated with the coupled deformation of the following components and assemblies: after frame, frontal frame and bumper assembly, roll bar, and sheet metal assembly, as shown on the left side of Fig. 3.2. The peak force in the second scenario is understood to be associated with the failure of the engine mounts and the rebound of the large engine mass. We define Scenario 1 as the crash process that takes place in the time domain 0 to 30 ms, and Scenario 2 as that which takes place in the interval between 30 and 60 ms. Due

to varying physics in different scenarios, the design problem can be decomposed in the time domain as two consecutive design tasks.

By employing the *time decomposition*, the original design task is much simplified, and a sequence of design processes can be considered.

3.3 Meta Model for Space Decomposition

After employing *time decomposition* to simplify the design problem as two consecutive design tasks, the *space decomposition* approach is to be utilized in Scenario 1 design to obtain the design target for each assembly and component through the target cascading process. To assist this design process, a meta-model with a computational cost that is lower than the computational cost of the original FE model needs to be developed. The reason for this relies on the following fact: the target cascading process for the *space decomposition* is to be formulated as an optimization problem, and this optimization problem needs to be solved efficiently to obtain the assembly and component design targets; the FE model is computationally expensive and is not suitable for this purpose. Base on this, a lumped mass-spring (LMS) model has been developed to serve as such a meta-model to replace the FE model for the target cascading process, while still having an extremely low computational cost. In the LMS model, the level of simplification is very high; this model, however, can provide sufficient information for the implementation of the target cascading to obtain the design targets for the assemblies and the components in Scenario 1 design.

The LMS model uses non-linear springs, called energy absorbers (EA), and

lumped masses to represent the corresponding vehicle components with no limitation in number. The equation of motion to be solved in each simulation iteration is

$$M\frac{d^2u}{dt^2}+C\frac{du}{dt}+Ku=0\,,\ \left.\frac{du}{dt}\right|_{t=0}=v_0\ ,\ u(0)=0 \tag{3.1}$$

where M , C, and K are the mass, damping, and stiffness matrices of the structural system, respectively, u is the displacement vector, and t the time. The initial velocity is v_0. In Eq. (3.1) the stiffness and the damping matrices are non-linear, and they change with the strain rate and deflection of the EAs, respectively. There are no external forces applied to the system; hence, any force exerted by a barrier is simulated using a large mass with zero velocity.

Since the only integration variable is time (no spatial variable defining a domain exists), the problem does not have boundary conditions to satisfy, and therefore, the time integration is the main task of the computational program. There are two main integration algorithms provided in applied mathematics, namely, explicit and implicit algorithms.

In this research, an explicit algorithm called the second order Adams-Bashforth algorithm [67] is implemented. The formulas are expressed as

$$\left.\frac{du}{dt}\right|_{i+1}=\left.\frac{du}{dt}\right|_{i}+\Delta t\left(\frac{3}{2}\left.\frac{d^2u}{dt^2}\right|_{i}-\frac{1}{2}\left.\frac{d^2u}{dt^2}\right|_{i-1}\right),i>0$$

$$u|_{i+1}=u|_{i}+\Delta t\left(\frac{3}{2}\left.\frac{du}{dt}\right|_{i}-\frac{1}{2}\left.\frac{du}{dt}\right|_{i-1}\right),i>0 \tag{3.2}$$

where i is the integration index ($i=0$ is time zero), and Δt is a time step used for integration. Notice that these formulas need the acceleration of the mass to start the

integration process; hence, the first step in the integration is the computation of the acceleration from the initial conditions. This is achieved using

$$\left.\frac{d^2u}{dt^2}\right|_i = \frac{1}{m}\left(\sum_{k=1}^{N} F_k\big|_i\right) \tag{3.3}$$

where m is any mass in the system; N is the number of EAs connected to that mass; and F_k is the force generated in the k^{th} EA connected to that mass. This force is produced by the initial conditions, namely, the initial velocity of the vehicle.

In addition, Eq. (3.2) needs information, not only from the previous time step, but from the two previous time steps (i and $i-1$). Therefore, the first integration step is treated separately using the Euler forward integration formulas:

$$\left.\frac{du}{dt}\right|_{i+1} = \left.\frac{du}{dt}\right|_i + \Delta t \left.\frac{d^2u}{dt^2}\right|_i, i = 0$$

$$u\big|_{i+1} = u\big|_i + \Delta t \left.\frac{du}{dt}\right|_i, i = 0 \tag{3.4}$$

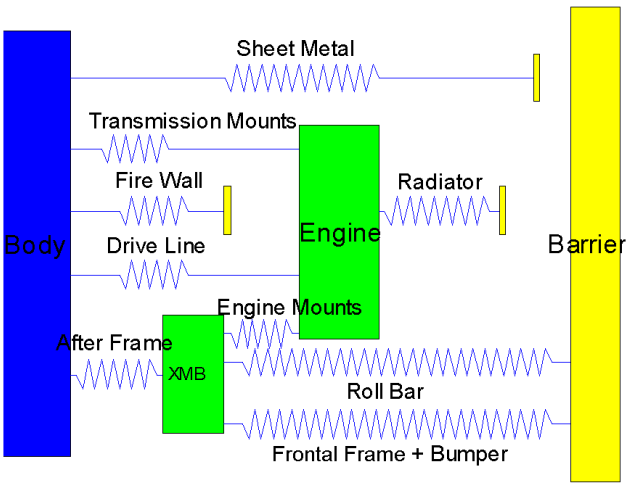

Figure 3.3: Lumped mass-spring model of the representative vehicle

The developed LMS model of the vehicle for design is shown in Fig. 3.3. The

lumped masses in the LMS model are calculated based on the FE model of the vehicle. LS-DYNA simulations are performed to obtain the force-deflection curves for each EA in the LMS model, using the assembly or component FE model. Figure 3.4b illustrates an example force-deflection curve obtained for the frontal frame and bumper assembly shown in Fig. 3.4a. Note that the control points (d_i, F_i) ($i = 1, 2, \ldots, 7$) on the force-deflection curve characterize the crash performance of the assembly, and will be used as design variables in the following target cascading process.

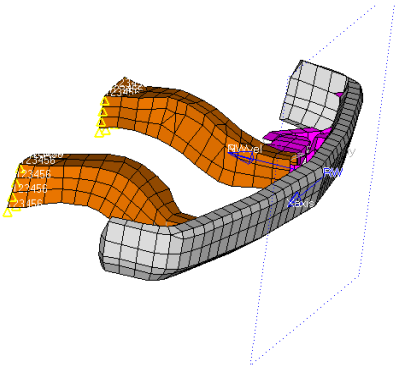

(a)

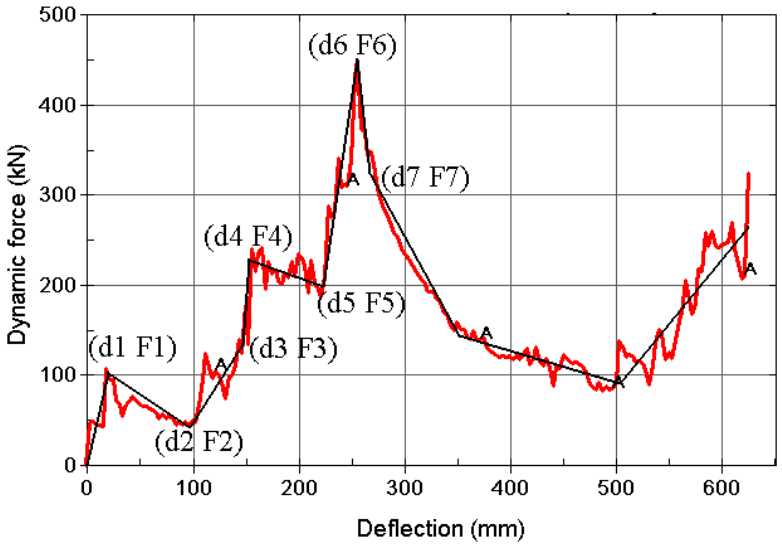

(b)

Figure 3.4: Example force-deflection curve obtained from a finite element simulation: (a) frontal frame and bumper assembly; and (b) force-deflection curve of (a) and control points.

The developed LMS model is finely tuned to be in good correlation with the FE model, see Fig 3.5, so that it can be utilized for the *space decomposition* and target cascading process.

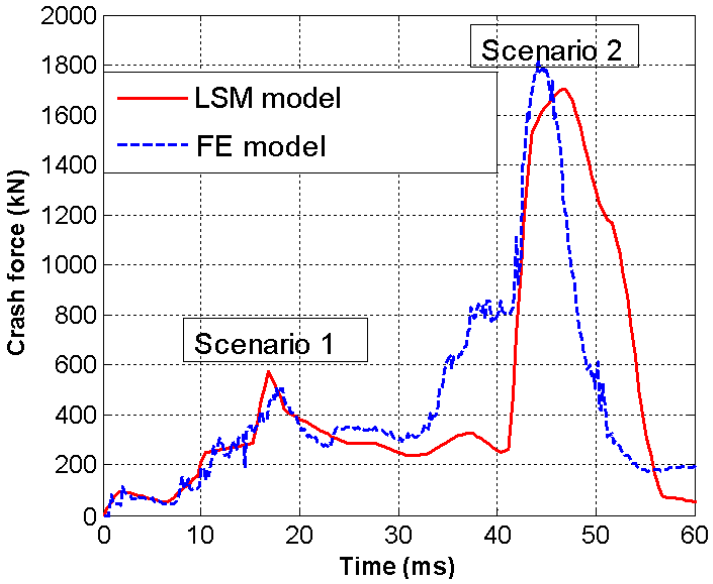

Figure 3.5: The LMS model is well correlated to finite element model

3.4 Space Decomposition and Target Cascading

With the implementation of the *time decomposition* approach, the original design problem has been decomposed as two consecutive design tasks, corresponding to the two major crash scenarios, respectively. The objective of Scenario 1 design is to increase the crash force to the ideal value in the time range of 0 to 30 ms; this is equivalent to maximizing the crash energy absorption of the system in the considered time period. To achieve this design objective, the following procedure should be followed:

1) Identify the relevant assemblies and components that contribute to the crash performance of the vehicle in Scenario 1;

2) Obtain the design targets for each identified assembly and component

through the target cascading process;

3) Design the assemblies and components to meet the cascaded targets;

4) Substitute the designed assemblies and components to the vehicle system for design validation.

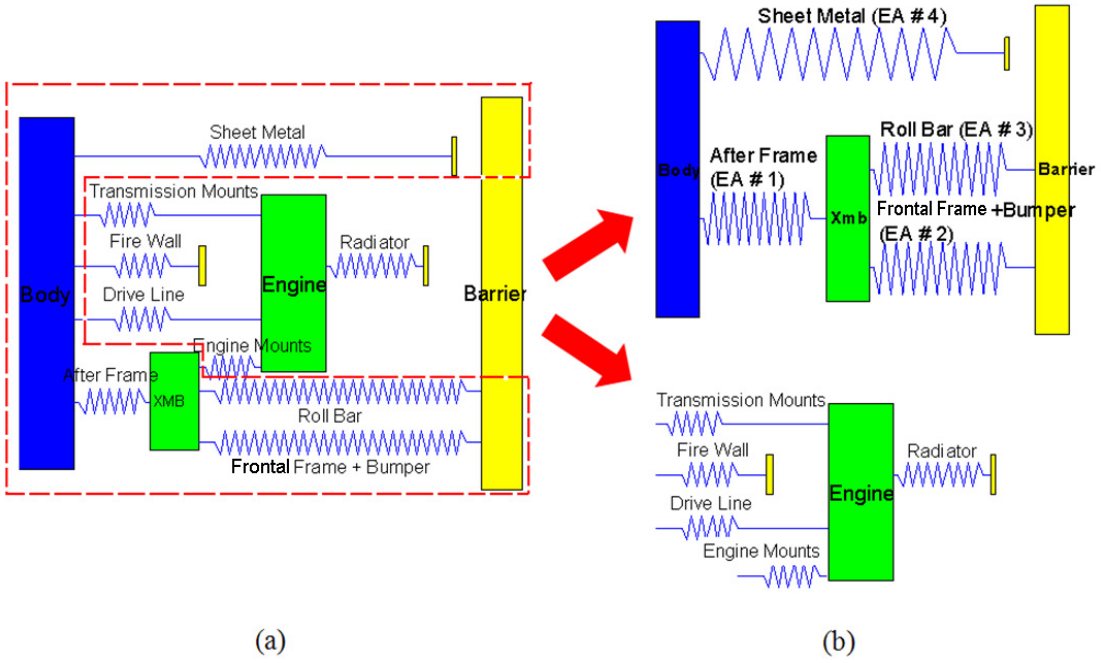

Figure 3.6: Space decomposition of the representative vehicle system: (a) original system; and (b) decomposed subsystems.

Based on the crash analyses using both the FE model and the LMS model, it is found that only the assemblies and components inside the dotted line of Fig. 3.6a contribute to the crash performance of the vehicle in Scenario 1 and should be considered in Scenario 1 design. Figure 3.6 illustrates the implementation of the *space decomposition* approach based on the LMS model. The original vehicle system is decomposed into two subsystems. The subsystem containing the assemblies and components related to the crash performance of Scenario 1 will be designed, while the subsystem including the engine and the associated components is

omitted in the current design task. Note that the implementation of the *space decomposition* approach in the current problem can be considered as a model reduction process since the design objective remains the same while the degrees of freedom (DOF) of the simulation model is reduced.

To obtain the design targets for each assembly and component in the subsystem to be designed, the target cascading process is carried out based on the subsystem LMS model. For the target cascading process, the following optimization problem is defined:

Find the vector

$$\{\mathbf{x}\} = \{d_{11},...,d_{17},F_{11},...,F_{17},d_{21},d_{22},d_{23},F_{21},F_{22},F_{23},d_{31},d_{32},d_{33},F_{31},F_{32},F_{33},d_{41},d_{42},d_{43},F_{41},F_{42},F_{43}\}^T$$

such that

$$\begin{aligned} &\underset{\mathrm{x}}{\text{Maximize}} \quad E_{0\sim 30ms}(\mathbf{x}) \\ &\text{Subject to} \quad F_{\max}(\mathbf{x}) \le 750KN \\ &\qquad\qquad \underline{x}_i \le x_i \le \overline{x}_i,\ (i = 1,2,\ldots,32) \end{aligned} \tag{3.5}$$

where d_{ij} and F_{ij} denote the deflection and force of the j-th control point on the force-deflection curve of the i-th assembly (or component) ($i = 1,2,3,4$; for $i = 1$, $j = 1,2,\ldots,7$; for $i \neq 1$, $j = 1,2,3$). $\underline{x}_i$ and $\overline{x}_i$ are the lower and upper bounds of the design variable x_i, respectively. $E_{0\sim 30ms}$ is the absorbed energy of all of the four EAs during time span of 0 to 30 ms. $F_{\max}(\mathbf{x})$ is the maximum crash force developed during this time period. An upper limit of 750 kN is set as the target force level to ensure the deceleration of the vehicle, with a total mass about 2000 kg, to be less than 40 G, so as to reduce the risk of occupant injury. A Matlab program is developed to perform the crash analyses using the LMS model and to solve the

optimization problem for target cascading.

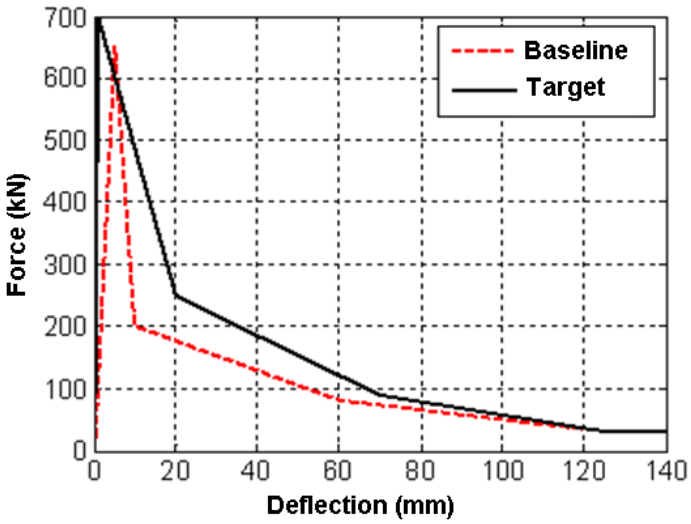

(a)

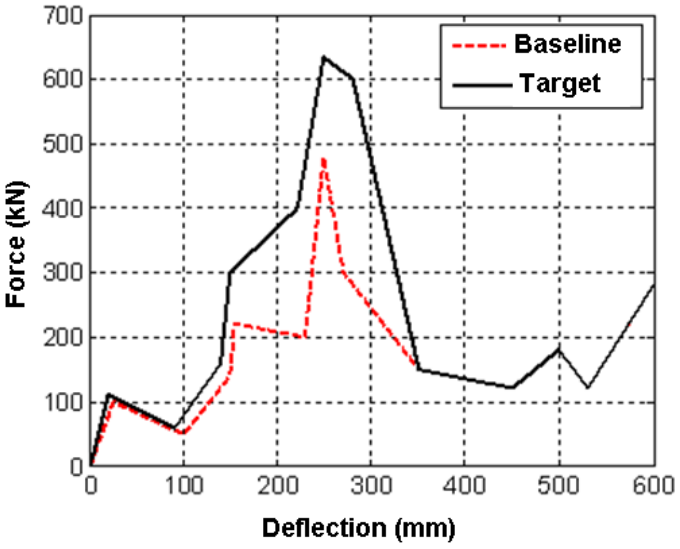

(b)

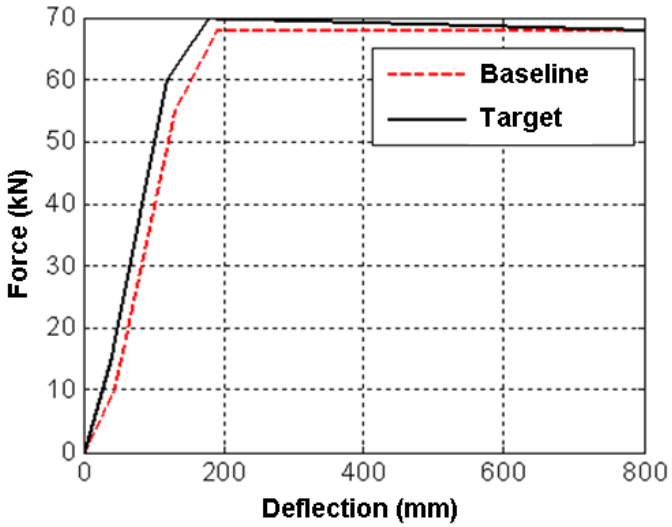

(c)

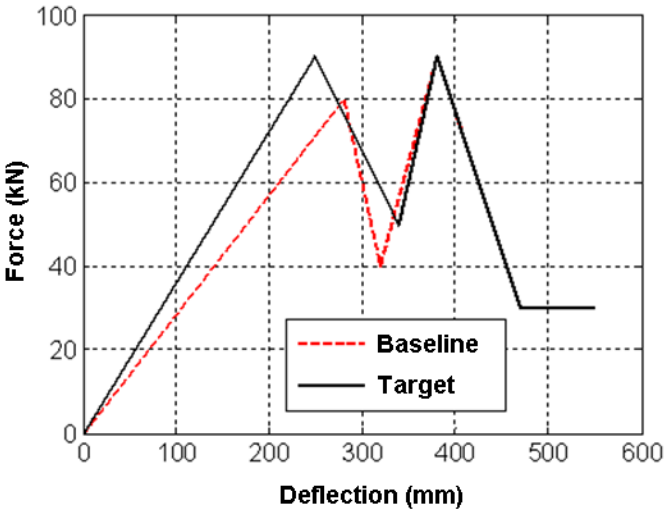

(d)

Figure 3.7: Baseline vs. cascaded design targets of energy absorbers: (a) after frame; (b) frontal frame and bumper assembly; (c) roll bar; and (d) sheet metal assembly.

The baseline and the cascaded targeting force-deflection curves of all four EAs are plotted in Fig. 3.7. As seen, the fundamental change that needs to be made is related to the frontal frame and bumper assembly. The target force-deflection curve in Fig. 3.7b should be used as the design target for the frontal frame and bumper assembly design. Figure 3.8a shows that the suggested design with all cascaded targets met can increase the energy absorption of the system by 38.2% in Scenario 1,

compared to the baseline design. Figure 3.8b further depicts that the crash force is pushed to the target value of 750 kN with the suggested design.

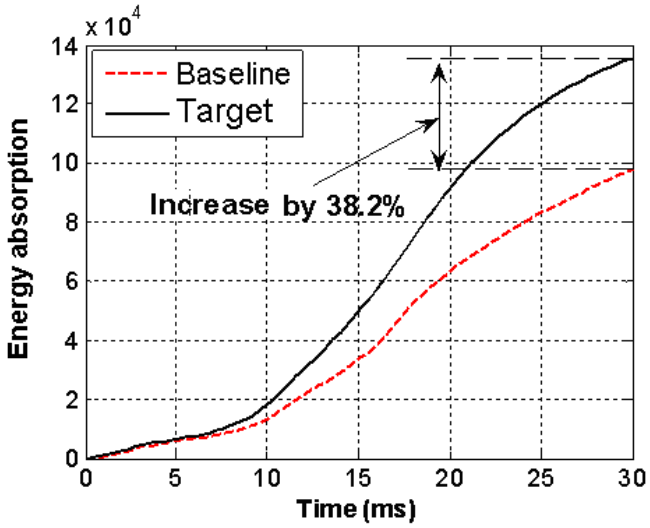

(a)

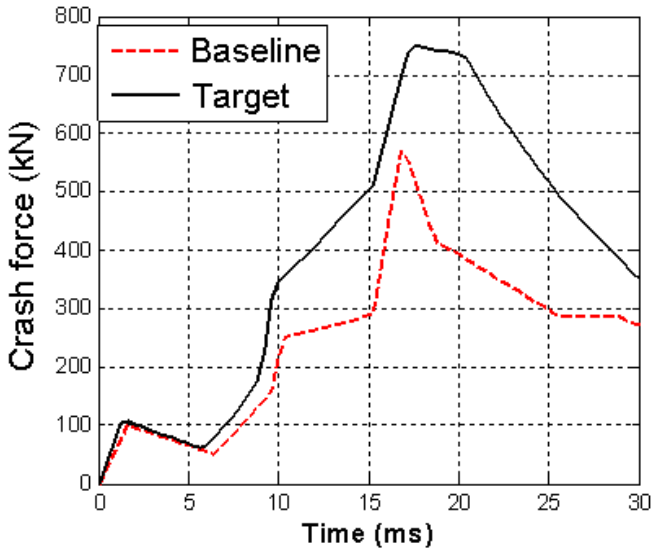

(b)

Figure 3.8: Design improvement in Scenario 1 by the suggested design: (a) energy absorption history; and (b) crash force history.

3.5 Design Results

To simply the problem, suppose that the design targets for all other assembly

and components in the subsystem have been met except for the frontal frame and bumper assembly. To meet the design target of the frontal frame and bumper assembly, optimization techniques such as the MMTO can be utilized. Here, for demonstration purposes, a simple design strategy is employed by properly increasing the wall thicknesses of the frontal frame and the bumper, to approximately meet the design target of the assembly. Fig. 3.9 plots the obtained force-deflection characteristic of the frontal frame and bumper assembly after design, together with that of the baseline design, based on LS-DYNA analyses.

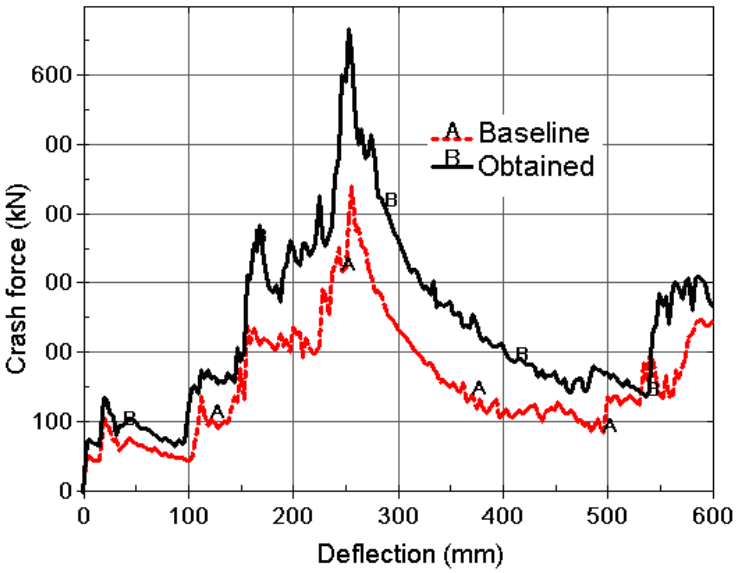

Figure 3.9: Force-deflection curves of the designed frontal frame and bumper assembly, and the baseline design

Once the cascaded design targets for all the assemblies and components are met, the last step is to substitute the designed assemblies and components into the vehicle system for design validation. Figure 3.10a shows the target improvement of the crash force history at the vehicle level based on the LMS model, and Fig. 3.10b

depicts the actual obtained crash force history at the vehicle level based on the FE model and LS-DYNA analysis. It is seen that with the design change, the crash force in the time range of Scenario 1 (0 to 30 ms) has been pushed toward the ideal curve, resulting in more crash energy absorption of the system in Scenario 1. As a result, the crash force in the time range of Scenario 2 has been substantially reduced, since the total crash energy to be absorbed is constant. At this point, the design task for Scenario 1 has been successfully accomplished.

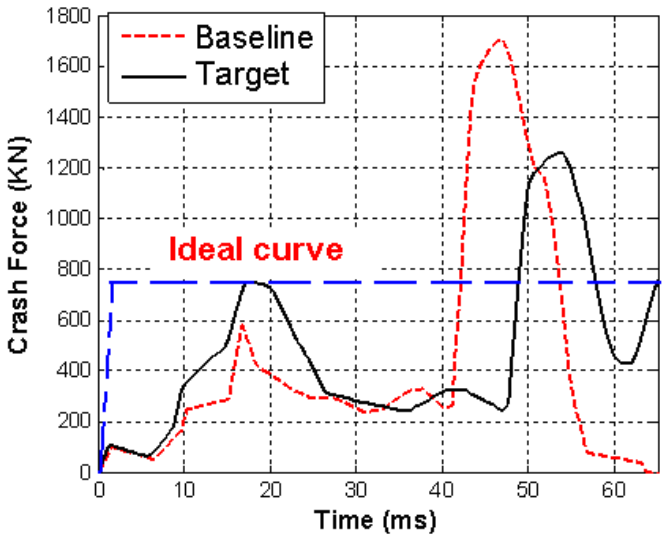

(a)

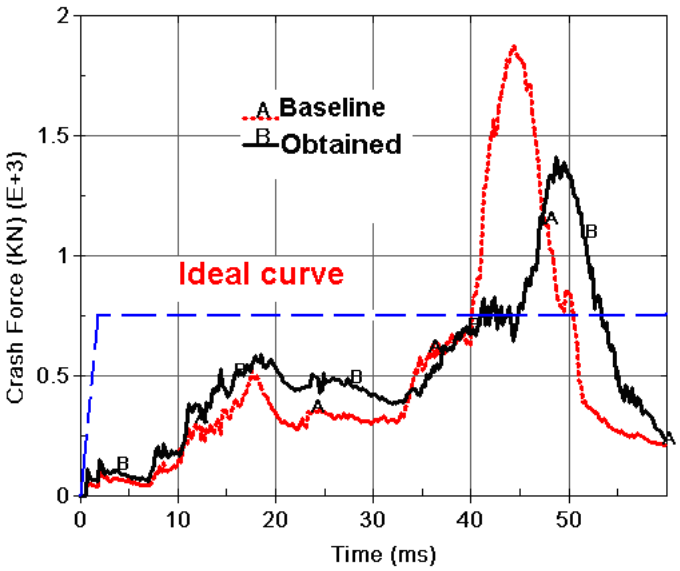

(b)

Figure 3.10: Vehicle-level design improvement after Scenario 1 design: (a) target improvement of crash force history based on the LMS model; and (b) obtained improvement of crash force history based on finite element simulation.

The objective of Scenario 2 design is to further push the crash force history curve towards the ideal curve in the time range of 30 to 60 ms, based on the improved design after the Scenario 1 design process. From the simulation, it is understood that the high peak force in Scenario 2 is associated with the failure of the engine mounts and the rebound of the large engine mass. This high peak force is transmitted to the passenger cabin through the drive line, causing rapid deceleration of the cabin.

To reduce the peak crash force in Scenario 2, the engine mounts need to be re-designed to successfully absorb the force caused by engine rebound. A design optimization problem is defined and solved to obtain the target force-deflection curve for the engine mounts based on the LMS model, as plotted in Fig. 3.11. Again, various optimization techniques can be employed to design the engine mount

structure to achieve this target characteristic curve. For the current problem, non-linear spring elements with the target force-deflection characteristic of the engine mounts are adopted in the FE model. Figure 3.12a shows the target improvement of the crash force history at the vehicle level with the re-designed engine mounts, based on the LMS model. Figure 3.12b depicts the actually obtained crash force history at the vehicle level with the re-designed engine mounts, based on the FE model and LS-DYNA analysis. It is seen that with the re-designed engine mounts, the peak crash force in Scenario 2 is substantially reduced and the crash force history curve approximates the ideal curve; the crash energy is absorbed through an expanded range of the crash force in the time domain. With that, the design task for Scenario 2 has been successfully accomplished.

As a result of this design process, the cabin deceleration level has been substantially reduced as shown in Fig. 3.12c.

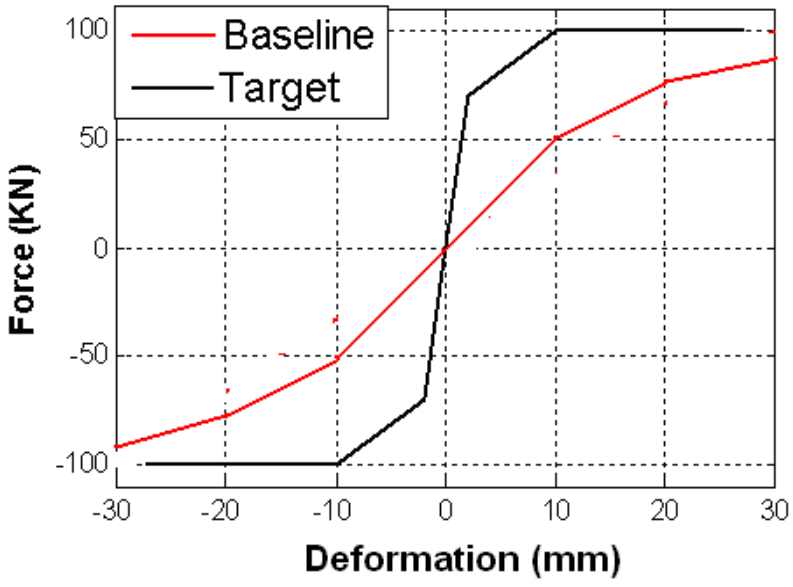

Figure 3.11: Design target of engine mounts

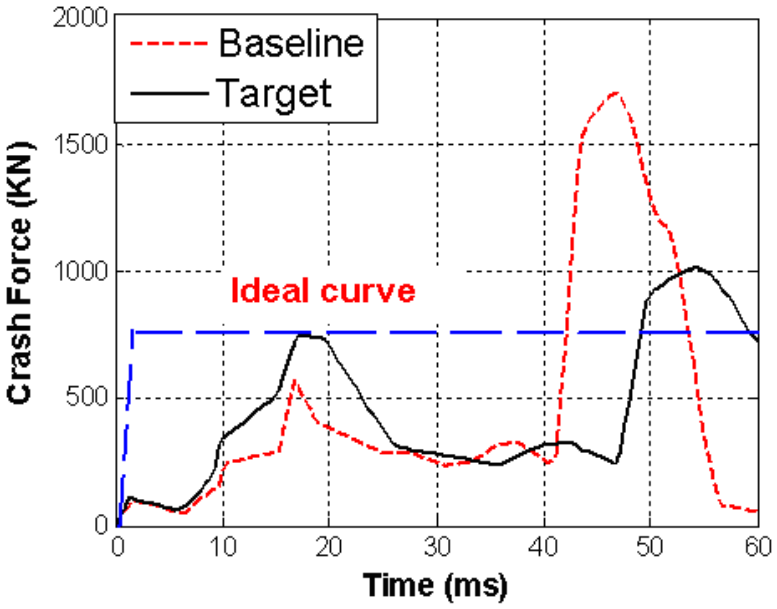
Baseline
Target
Ideal curve
Crash Force (KN)
Time (ms)
2000
1500
1000
500
0
0
10
20
30
40
50
60

(a)

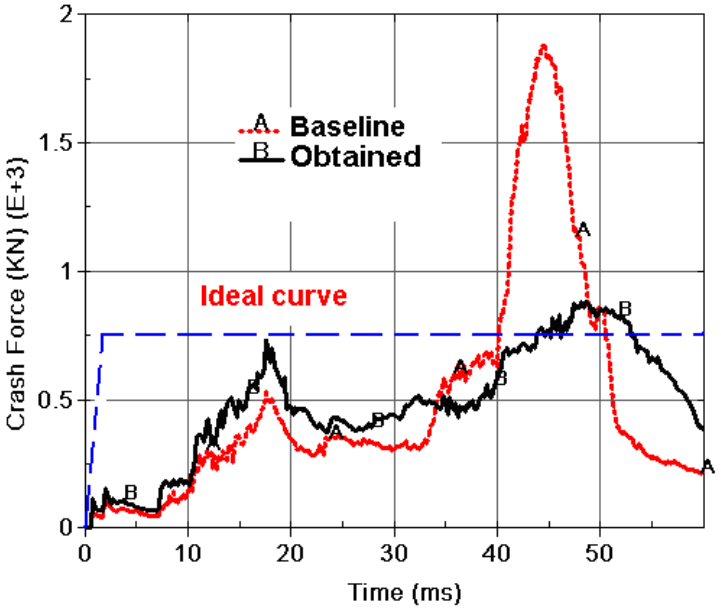
A Baseline
B Obtained
Ideal curve
Crash Force (KN) (E+3)
Time (ms)
2
1.5
1
0.5
0
0
10
20
30
40
50

(b)

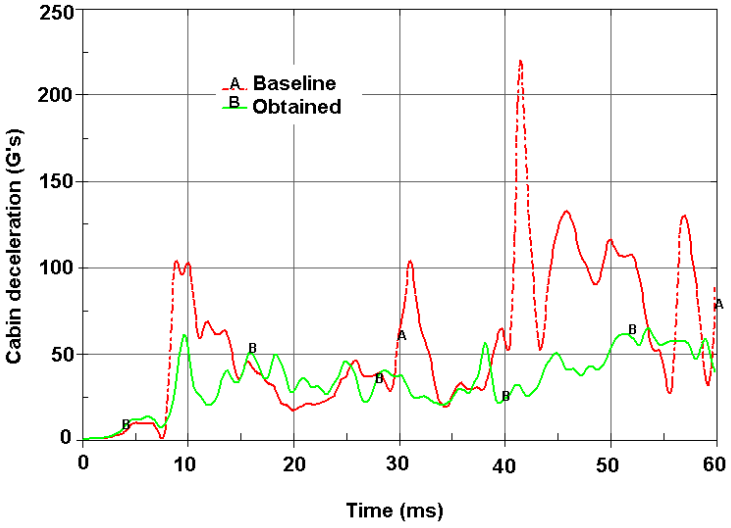

(c)

Figure 3.12: Vehicle-level design improvement after Scenario 2 design: (a) target improvement of crash force history based on the LMS model; (b) obtained improvement of crash force history based on finite element simulation; and (c) improved cabin deceleration history.

In this example design problem, approaches related the following layers of the magic cube have been employed: *time decomposition, space decomposition, target cascading* and *loading*. The employed approaches can be represented by four elements of the magic cube as shown in Fig. 3.13.

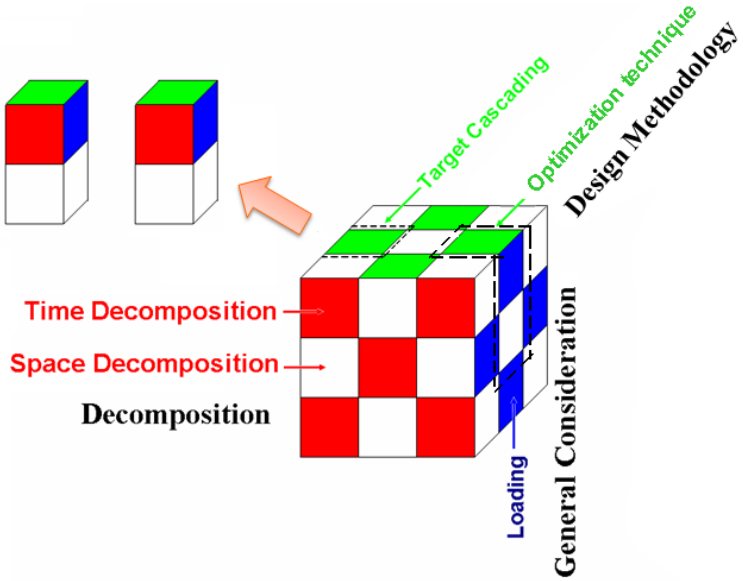

Figure 3.13: Elements of the magic cube for the vehicle crashworthiness design problem

3.6 Conclusion

The crashworthiness design problem of a representative vehicle system has been solved with the implementation of the MQ approach, showing the feasibility and effectiveness of this approach in solving such a complicated system-level crashworthiness design problem.

CHAPTER IV

Industry Applications of the Magic Cube Approach

In this chapter, the Magic Cube (MQ) approach is employed to solve two industry application problems: the elastomeric mounting system (EMS) design and the design for weight reduction of a vehicle system via material substitution.

4.1 Elastomeric Mounting System Design

An EMS can be extensively applied to control noise, vibration, and harshness (NVH) in the aerospace, automotive, and marine industries, and other related fields. An EMS can be made compact, and they are cost-effective and easy to maintain. Therefore, EMS has been used to isolate vehicle structures from engine vibration since the 1930s [68]. Extensive efforts have been made since then to improve the performance of the elastomeric mounts [69] [70] [71]. Another typical EMS in automotive vehicles is the cabin-frame (as well as bed-frame) mounting system, which is used to isolate the cabin (and bed) from the vibration of the vehicle frame and to reduce the noise level to improve riding comfort.

An EMS generally consists of at least three mounts. It can be modeled as a rigid body with the elastomeric mounts that support the rigid body. The rigid body can

represent, for example, a powertrain unit, a cabin, or a bed in a vehicle that has six degrees of freedom (DOF). The rigid body can translate and rotate about the three-independent Cartesian axes. The mounts are usually modeled as springs and dampers with viscous elastic or viscoelastic properties in each of the three principal directions. The behavior of the EMS depends not only on the performance of the individual mounts but also on the complete system configuration. The design of an EMS involves the selection of materials for desired mechanical properties and the determination of the locations and orientations of the individual mounts.

The development of EMS has mostly been concentrated on the improvement of quasi-static (amplitude-dependent) and dynamics (frequency-dependent) properties. The traditional "trial-and-error" methods in EMS design are highly dependent upon the engineer's experience and the flexibility allowed when modifying the system. Extensive experiments and analyses are required to meet the design criteria even in one aspect of the system performance, and this turns out to be very time-consuming. When multidisciplinary system performance objectives are considered, it becomes much more difficult to find a suitable design. A computerized automated design method such as optimization with reliable modeling techniques is highly desirable. Various objectives of optimization have been considered in the literature. One objective of the optimization is to tune the natural frequencies of the mounting system to a desired range to avoid resonance, and to improve the isolation of vibration and shock [72] [73] [74] [75] [76]. Swanson et al. [77] also showed that the forces transmitted through the mounts can be directly minimized in order to

obtain a truly optimal design of the mounting system. Ashrafiuon [78] further used these criteria to minimize the dynamic forces transmitted from the engine to the body. Other studies in the literature also used these two objectives [79] [80] [81].

No work has been found in the literature related to the stability analysis of the general purpose EMS in the area of crash load; similarly, little work has been undertaken to consider multidisciplinary design objectives. In this research, we derived an eigenvalue problem base on a second-order approximation of the original non-linear dynamic equation of the EMS for the stability analysis. The eigenvalue problem can be solved to determine the buckling load and the related buckling mode of the system. The stability-related objective is for the first time introduced to the design optimization of EMS, which can then be used to improve system behavior that results from the non-linear bifurcation. In addition to the objective of stability, other design objectives, including quasi-static, dynamic, and durability targets, are also considered. Optimization with the multidisciplinary objectives leads to a very practical and reliable design in all aspects of the EMS.

In the practical EMS design, uncertainties of the system parameters have to be considered. For example, manufacturing variation will induce uncertainties in the stiffness of the individual mounts, and assembly errors may cause uncertainties in the locations and orientations of these mounts. In order to estimate the reliability and robustness of the optimal design, a reliability assessment is essential. Approximation techniques developed to assess the reliability of a component or system can be broadly categorized into two groups: a) random sampling methods,

and b) analytical methods. The selection of methods depends on the problem involved. In this research, a prevalent method, a Monte Carlo simulation, is used to assess the reliability of the optimal design.

4.1.1 EMS Analyses

The EMS considered in this research is modeled as a rigid body that is supported by a number of elastomeric mounts. It is assumed that all of the mounts are seated on a rigid base. Note that this assumption can be easily extended to consider a flexible base. As shown in Fig. 4.1, the origin of the global co-ordinate system is at the center of gravity (C.G.) of the rigid-body, while the X- and Y-axes are parallel to the base, with Z being normal to the base. The rigid body consists of six independent DOF, which include three translational and three rotational coordinates.

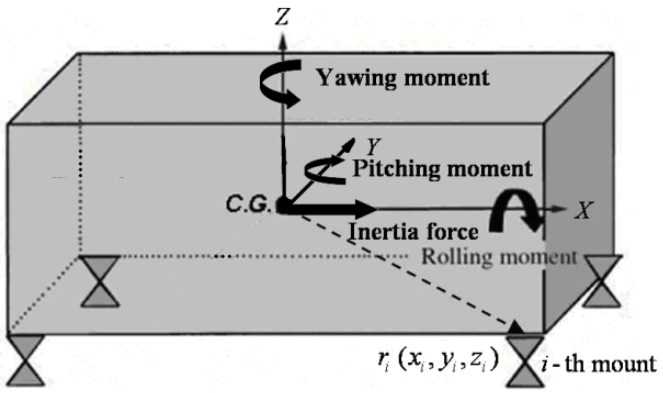

Figure 4.1: A rigid body on elastomeric mounts

Quasi-static, Frequency Response, and Eigenvalue Analyses

Assume that $\{\mathbf{r}_c\} = \{x_c, y_c, z_c\}^T$ is the translational displacement vector of the

C.G. of the rigid body, and $\{\boldsymbol{\Theta}\} = \{\theta_x, \theta_y, \theta_z\}^T$ is the linear angle vector that represents a small rotation of the rigid body about its C.G., where θ_x, θ_y, and θ_z are components of the rotation with respect to three axes of the global coordinate system. Then a complete set of independent generalized coordinates for the EMS can be defined as

$$\{\mathbf{q}\} = \{\mathbf{r}_c^T, \quad \boldsymbol{\Theta}^T\}^T \tag{4.1}$$

Under the assumption of "small" motion, the EMS equation can be linearised about its initial configuration and thus written as

$$[\mathbf{M}]\{\ddot{\mathbf{q}}\} + [\mathbf{C}]\{\dot{\mathbf{q}}\} + [\mathbf{K}]\{\mathbf{q}\} = \{\mathbf{p}\} \tag{4.2}$$

where [**M**] denotes the inertia matrix, [**C**] denotes the damping matrix, [**K**] denotes the stiffness matrix, and $\{\mathbf{p}\}$ is the force vector (including the torques) applied at the body C.G.

The stiffness and damping matrices are contributed from each mount, and in general we have

$$[\mathbf{K}] = \sum_{i=1}^{N} [\mathrm{K_i}], \quad [\mathbf{C}] = \sum_{i=1}^{N} [\mathbf{C_i}] \tag{4.3}$$

where N is the total number of the mounts that support the rigid body, and

$$[\mathbf{K_i}] = \begin{bmatrix} [\mathbf{k_i}] & -[\mathbf{k_i}][\tilde{\mathbf{r}}_\mathrm{i}] \\ -[\tilde{\mathbf{r}}_\mathrm{i}]^T[\mathbf{k_i}] & [\tilde{\mathbf{r}}_\mathrm{i}]^T[\mathbf{k_i}][\tilde{\mathbf{r}}_\mathrm{i}] \end{bmatrix} \tag{4.4}$$

is the stiffness contribution matrix from the i-th mount. Here $[\tilde{\mathbf{r}}_\mathrm{i}]$ is a skew matrix of the position vector $\{\mathbf{r_i}\}$, while $\{\mathbf{r_i}\} = \{x_i, y_i, z_i\}^T$ is the position vector of the i-th mount, and we have

$$[\tilde{\mathbf{r}}_\mathbf{i}] = \begin{bmatrix} 0 & -z_i & y_i \\ z_i & 0 & -x_i \\ -y_i & x_i & 0 \end{bmatrix} \tag{4.5}$$

where x_i, y_i, z_i are the coordinates of the i-th mount measured at the body-fixed coordinate system (as shown in Fig. 4.1). $[\mathbf{k}_\mathbf{i}]$ is the stiffness matrix of mount i measured in the global coordinate system.

Assuming a (linear) viscous elastic mount, $[\mathbf{k}_\mathbf{i}]$ can be expressed as

$$[\mathbf{k}_\mathrm{i}] = [\mathbf{A}_\mathrm{i}][\mathbf{k}'_\mathrm{i}][\mathbf{A}_\mathrm{i}]^T \tag{4.6}$$

where $[\mathbf{k}'_\mathrm{i}]$ is the stiffness matrix of the i-th mount measured in the mount local coordinate system, and $[\mathbf{A}_\mathrm{i}]$ is the transposition matrix, which can be defined, for example, using Euler angles.

Assuming a viscous damping matrix for the i-th mount, namely,

$$[\mathbf{c}'_\mathrm{i}] = \eta_i[\mathbf{k}'_\mathrm{i}] \tag{4.7}$$

where η_i is the loss factor of the i-th mount, then the viscous damping matrix that contributes to the global damping matrix [**C**] in Eq. (4.3), of mount i, can be obtained as

$$[\mathbf{C}_i] = \eta_i[\mathbf{K}_i] \tag{4.8}$$

Based on Eq. (4.2), for a frequency response problem, we have

$$\left([\mathbf{K}] + j\omega[\mathbf{C}] - \omega^2[\mathbf{M}]\right)\{\mathbf{q}\} = \{\mathbf{p}\} \tag{4.9}$$

where {**q**} and {**p**} are the amplitudes of the body C.G. displacement and force vectors, respectively, and ω is the excitation frequency.

For the quasi-static analysis, assume that

$$\{\mathbf{p}\} = -[\mathbf{M}]\{\mathbf{a}\} \tag{4.10}$$

is the inertia force applied on the body, where $\{\mathbf{a}\}$ is a given acceleration vector of the rigid body. Then we have

$$[\mathbf{K}]\{\mathbf{q}\} = \{\mathbf{p}\} \tag{4.11}$$

Finally, for the modal analysis, we have

$$\left([\mathbf{K}] - \lambda_n[\mathbf{M}]\right)\boldsymbol{\varphi}_n = 0 \tag{4.12}$$

where λ_n donates the n-th eigenvalue of the EMS, and $\boldsymbol{\varphi}_n$ is the corresponding eigenvector.

Note that the displacement at each mount due to the rigid body motion $\{\mathbf{q}\}$ can be obtained as

$$\{\mathbf{U_i}\} = \{\mathbf{r_c}\} + [\tilde{\mathbf{r}}_\mathbf{i}]^T\{\boldsymbol{\Theta}\} \tag{4.13}$$

The force transmitted to the base through the i-th mount can be then obtained as

$$\{\mathbf{F_i}\} = -[\mathbf{k_i}]\{\mathbf{U_i}\} \tag{4.14}$$

Stability Analysis

Consider a perturbation on the rigid body from its equilibrium position, one that results in a displacement $\{\mathbf{q}\} = \{\mathbf{r}_c^T,\ \boldsymbol{\Theta}^T\}^T$. The potential energy due to the perturbation can be then written as

$$V = \{\mathbf{r}_c\}^T\{\mathbf{F}\} + \{\boldsymbol{\Theta}\}^T\{\boldsymbol{\tau}\} \tag{4.15}$$

where $\{\mathbf{F}\} = \{F_x, F_y, F_z\}^T$ denotes the external force vector applied on the C.G., $\{\boldsymbol{\tau}\} = [\tilde{\mathbf{r}}_c][\mathbf{F}]$ denotes the torque vector resulted from the perturbation of the C.G. and the force applied, and $[\tilde{\mathbf{r}}_c]$ is the skew matrix of the vector $\{\mathbf{r}_c\}$. Note that $\{\tau\}$ defined in this research is a higher-order non-linear effect, which is considered here because it provides a major contribution to the stability condition. Equation (4.15) can be then rewritten as

$$V = \{\mathbf{q}\}^T \{\mathbf{p}\} + \frac{1}{2} \lambda_b \{\mathbf{q}\}^T [\mathbf{K_G}] \{\mathbf{q}\} \tag{4.16}$$

where $\{\mathbf{p}\} = \{\mathbf{F}^T, \ 0\}^T$, $\lambda_b = |\mathbf{F}|$ denotes the amplitude of $\{\mathbf{F}\}$, and $[\mathbf{K}_G]$ is so-called the geometry stiffness matrix,

$$[\mathbf{K}_G] = \begin{bmatrix} 0 & \mathbf{B} \\ \mathbf{B}^T & 0 \end{bmatrix} \tag{4.17}$$

where

$$[\mathbf{B}] = \frac{1}{2} \begin{bmatrix} 0 & -\gamma & \beta \\ \gamma & 0 & -\alpha \\ -\beta & \alpha & 0 \end{bmatrix} \tag{4.18}$$

and where α, β, γ are direction cosines of the force vector $\{\mathbf{F}\}$ measured at the global coordinate system.

The internal energy stored in the EMS due to the perturbation can be written as

$$U = \frac{1}{2} \{\mathbf{q}\}^T [\mathbf{K}] \{\mathbf{q}\} \tag{4.19}$$

The total energy stored in the EMS due to the perturbation then becomes

$$\Pi = U - V \tag{4.20}$$

The stability condition of the mechanical system requires the Hessian matrix of

Π to be positive, resulting in a critical condition:

$$\det\left[\frac{\partial^2 \Pi}{\partial q_i \partial q_j}\right] = 0 \tag{4.21}$$

or a corresponding eigenvalue problem

$$([\mathbf{K}] - \lambda_b [\mathbf{K}_G])\{\boldsymbol{\varphi}_b\} = 0 \tag{4.22}$$

where λ_b denotes the critical buckling force, and $\{\boldsymbol{\varphi}_b\}$ is the corresponding buckling mode.

4.1.2 Optimization Problems of EMS

Assuming $\{\mathbf{x}\} = \{x_1, x_2, \ldots, x_n\}^T$ stands for a vector of the design variables, an optimization problem of the general mounting system can be written as:

Find $\{\mathbf{x}\}$ such that

$$\begin{aligned} &\underset{\mathbf{x}}{\text{Minimize}}\ f(\mathbf{x}) \ (\text{or } -f(\mathbf{x})) \\ &\text{Subject to}\ h_j(\mathbf{x}) \le 0,\ (j = 1, 2, \ldots, m) \\ &\underline{x}_i \le x_i \le \bar{x}_i,\ (i = 1, 2, \ldots, n) \end{aligned} \tag{4.23}$$

where x_i denotes a design variable, which can be a location, orientation, stiffness, or damping variable of an individual mount. $\underline{x}_i$ and $\bar{x}_i$ are the lower and upper bounds of x_i, $(i = 1, 2, \ldots, n)$, $f(\mathbf{x})$ denotes the objective function, and $h_j(\mathbf{x})$, $(j = 1, 2, \ldots, m)$ are constraint functions. $f(\mathbf{x})$ can be defined as one of, or a combination of, the following:

1) Displacement and rotation of the body C.G., i.e.

$$f_1 = (1-\alpha)\sqrt{\{r_c\}^T \{r_c\}} + \alpha\sqrt{\{\Theta\}^T \{\Theta\}} \tag{4.24}$$

where $\alpha\ (0 \le \alpha \le 1)$ is a given weighting parameter.

2) The mean eigenvalue of the system is [82]

$$f_2 = \lambda_0 + \alpha \left(\sum_{i=1}^{m} \frac{w_i}{(\lambda_{n_i} - \lambda_{0_i})^n} \right)^{-1/n} \tag{4.25}$$

where λ_{n_i} $(i = 1,2,\ldots,m)$ are the eigenvalues to be optimized (defined in Eq. (4.12)), $n = 1,\ 2,\ -2$, or otherwise, is a parameter used to define different design problems. w_i $(i = 1,2,\ldots,m)$ are given weighting coefficients, λ_{0_i} $(i = 1,2,\ldots,m)$ are given target eigenvalues, λ_0 and α are constants which are used only for adjusting the dimension of the objective function.

3) Critical buckling force of the system

$$f_3 = \lambda_b \tag{4.26}$$

where λ_b is defined in Eq. (4.22).

4) Maximum mounting force

$$f_4 = \max\{F_i, i = 1,2,\ldots,N\} \tag{4.27}$$

where $F_i = \sqrt{\{\mathbf{F_i}\}^T \{\mathbf{F}_i\}}$ is the magnitude of the transmitted force $\{\mathbf{F}_i\}$ at the i-th mount.

4.1.3 Design Sensitivities

Design sensitivities of the objective functions defined in the previous section can be obtained as the following:

The sensitivity of objective function f_1 defined in Eq. (4.24) can be calculated as

$$\frac{\partial f_1}{\partial x} = -\{v\}^T \frac{\partial [K]}{\partial x}\{q\} \tag{4.28}$$

where $\{v\}$ is the solution of Eq. (4.9) (when a frequency response problem is considered) or Eq. (4.11) (when a quasi-static response problem is considered) with a load vector

$$\{p\} = \left\{ (1-\alpha)\frac{\{r_c\}^T}{\sqrt{\{r_c\}^T\{r_c\}}} \quad \alpha \frac{\{\Theta\}^T}{\sqrt{\{\Theta\}^T\{\Theta\}}} \right\}^T \tag{4.29}$$

The sensitivity of objective function f_2 defined in Eq. (4.25) can be calculated as

$$\frac{\partial f_2}{\partial x} = \frac{(f_2 - \lambda_0)^{n+1}}{\alpha^n} \sum_{i=1}^{m} \frac{w_i}{(\lambda_{n_i} - \lambda_{0_i})^{n+1}} \frac{\partial \lambda_{n_i}}{\partial x} \tag{4.30}$$

where

$$\frac{\partial \lambda_{n_i}}{\partial x} = \frac{\{\phi_{n_i}\}^T \frac{\partial [K]}{\partial x}\{\phi_{n_i}\}}{\{\phi_{n_i}\}^T [M]\{\phi_{n_i}\}} \tag{4.31}$$

For the buckling problem defined in Eq. (4.22), the sensitivity of the critical buckling force can be calculated as

$$\frac{\partial f_3}{\partial x} = \frac{\partial \lambda_b}{\partial x} = \frac{\{\phi_b\}^T \frac{\partial [K]}{\partial x}\{\phi_b\}}{\{\phi_b\}^T [K_G]\{\phi_b\}} \tag{4.32}$$

The sensitivity of the maximum mounting force can be obtained as

$$\frac{\partial f_4}{\partial x} = \frac{\{F_m\}^T}{\sqrt{\{F_m\}^T\{F_m\}}} \frac{\partial \{F_m\}}{\partial x} \tag{4.33}$$

where m is the number of the mount that experiences the maximum mounting force,

and

$$\frac{\partial\{F_m\}}{\partial x} = \{v\}^T \frac{\partial[k_m]}{\partial x}\{q\} - \frac{\partial[k_m]}{\partial x}\{U_m\} \tag{4.34}$$

where $\{v\}$ is the solution of Eq. (4.9) (when a frequency response problem is considered) or Eq. (4.11) (when a quasi-static response problem is considered) with a load vector

$$\{p\} = [I - [\tilde{\Theta}] \quad [\tilde{r}_m]]^T [k_m] \tag{4.35}$$

where, $\left[\tilde{\Theta}\right]$ and $\left[\tilde{r}_m\right]$ are the skew matrices of vectors $\left\{\Theta\right\}$ and $\left\{r_m\right\}$, respectively.

Furthermore, the sensitivity of the global stiffness matrix with respect to the design variables can be expressed as follows:

$$\frac{\partial[K]}{\partial x} = \sum_{i=1}^{N} \frac{\partial[K_i]}{\partial x} \tag{4.36}$$

For the design variables related to the locations of the mounts ($x = l$), we have

$$\frac{\partial[K_i]}{\partial l} = \begin{bmatrix} 0 & [k_i]\dfrac{\partial[\tilde{r}_i]}{\partial l} \\ \dfrac{\partial[\tilde{r}_i]^T}{\partial l}[k_i] & \dfrac{\partial[\tilde{r}_i]^T}{\partial l}[k_i][\tilde{r}_i] + [\tilde{r}_i]^T[k_i]\dfrac{\partial[\tilde{r}_i]}{\partial l} \end{bmatrix} \tag{4.37}$$

For the design variables related to the orientations of the mounts ($x = \theta$), we have

$$\frac{\partial[K_i]}{\partial \theta} = \begin{bmatrix} \dfrac{\partial[k_i]}{\partial \theta} & \dfrac{\partial[k_i]}{\partial \theta}[\tilde{r}_i] \\ [\tilde{r}_i]\dfrac{\partial[k_i]}{\partial \theta} & [\tilde{r}_i]^T \dfrac{\partial[k_i]}{\partial \theta}[\tilde{r}_i] \end{bmatrix} \tag{4.38}$$

where

$$\frac{\partial[k_i]}{\partial\theta}=\frac{\partial[A]}{\partial\theta}[k_i'][A]^T+[A][k_i']\frac{\partial[A]^T}{\partial\theta} \tag{4.39}$$

For the design variables related to the mounts stiffness coefficients ($x = s$), we have

$$\frac{\partial[K_i]}{\partial s}=\begin{bmatrix}\dfrac{\partial[k_i]}{\partial s} & \dfrac{\partial[k_i]}{\partial s}[\tilde{r}_i] \\ [\tilde{r}_i]\dfrac{\partial[k_i]}{\partial s} & [\tilde{r}_i]^T\dfrac{\partial[k_i]}{\partial s}[\tilde{r}_i]\end{bmatrix} \tag{4.40}$$

where

$$\frac{\partial[k_i]}{\partial s}=[A]\frac{\partial[k_i']}{\partial s}[A]^T \tag{4.41}$$

4.1.4 Reliability Assessment for Optimal Design

For reliability analyses of the EMS, the probabilistic performance measurement can be defined as

$$G(\mathbf{X})=\frac{d_{\max}}{d}-1 \text{ or } G(\mathbf{X})=\frac{d}{d_{\min}}-1 \tag{4.42}$$

where $\{\mathbf{X}\}$ is a random vector representing the uncertainties of the design parameters, $d_{\max}$ ($d_{\min}$) is the maximum (minimum) value of the design target, and d is the actual value of the design target. Here, a failure event is defined as $G(\mathbf{X}) \le 0$. The probability of failure p_f is defined as

$$p_f = P\{G(\mathbf{X}) \le 0\} \tag{4.43}$$

which is generally calculated by the integral

$$p_f = \int\cdots\int_{G(\mathbf{X})\le 0} f_{\mathbf{X}}(\mathbf{X})\mathbf{dX} \tag{4.44}$$

where $f_{\mathbf{X}}(\mathbf{X})$ is the probability density function (PDF) of $\{\mathbf{X}\}$ and the probability is evaluated by the multidimensional integration over the failure region $G(\mathbf{X})$.

The reliability R is the probability that the EMS works properly, and it is given by

$$R = P\{G(\mathbf{X}) > 0\} = 1 - p_f \tag{4.45}$$

It is very difficult or even impossible to analytically compute the multidimensional integration in Eq. (4.44). Some approximation methods, such as the first order reliability method (FORM) [83] or the asymptotic second-order reliability method (SORM) with a rotationally invariant reliability measure [84], have been developed to provide efficient solutions, while maintaining a reasonable level of accuracy. In this research, however, we simply use a Monte Carlo simulation to investigate the robustness of the optimal design. The reason for this lies in the fact that calculating the response function of the general purpose EMS defined in this research is not expensive, so the large number of function evaluations for an effective Monte Carlo simulation can be performed without a high computational cost.

4.1.5 Example Design Results

As an example design problem, we consider an EMS that is employed in an innovative concept vehicle shown in Fig. 4.2. The demonstration system has a vessel supported by four mounts made of elastomeric bushings; the mounts are connected to the frame of the vehicle.

In the current problem, the vessel is assumed to be a rigid body with a total mass of 256.7 kg. The moment of inertia matrix is

$$\mathbf{I} = \begin{bmatrix} 7.7 & -1.1 & 3.7 \\ -1.1 & 52.0 & 1.0 \\ 3.7 & 1.0 & 55.2 \end{bmatrix} Kg \cdot m^2 \tag{4.46}$$

The bushings are modeled as springs shown in Fig. 4.3 with axial stiffness coefficient $k_x' = 1.4e5$ N/m and radial stiffness $k_y' = k_z' = 1.4e6$ N/m. The three orthogonal local coordinate axes of each bushing are originally parallel to the axes of the global coordinate system. Damping effects of the bushings are neglected. The locations of the body C.G. and each bushing are listed in Table 4.1. The major load considered in the current design consists of the inertia forces of the vessel when the vehicle has accelerations or decelerations during braking or steering. The load is assumed as a worst case of a 10 g inertia force applied to the C.G. of the body in the X-Y plane with an angle θ counter clockwise from the positive X axis as shown in Fig. 4.4. Various loading conditions are considered by varying the angle θ with the constant amplitude of the load.

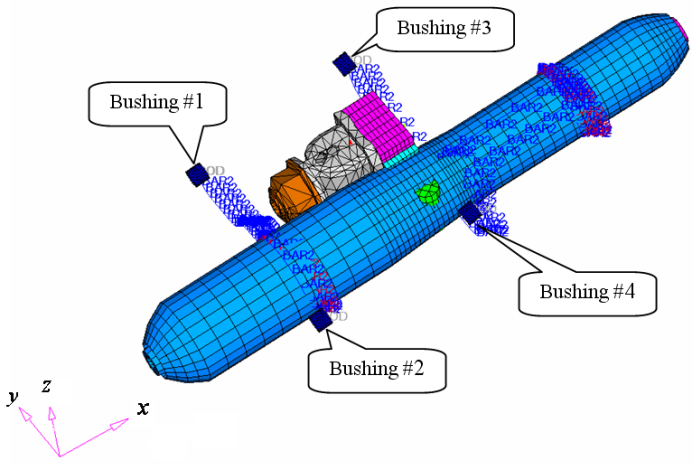

Figure 4.2: Example EMS

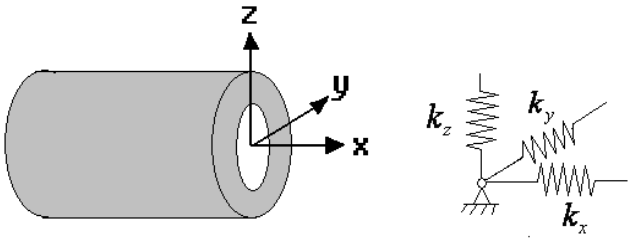

Figure 4.3: The bushing model with stiffness in three principal directions without viscous damping

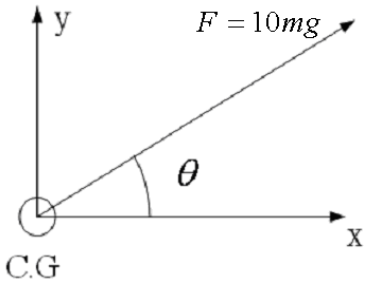

Figure 4.4: Load vector and its direction in the X-Y plane

Table 4.1: Bushing locations of the example EMS

	X(mm)	Y(mm)	Z(mm)
Body C.G.	0	0	0
Bushing 1	-459.8	521.5	-77.2
Bushing 2	-457.0	-352.0	-76.6
Bushing 3	206.0	520.9	77.4
Bushing 4	206.2	-372.6	78.0

The design variables considered in the current design problem are the orientation angles of the bushings about the Z-axis. The design variable vector is therefore $\{\mathbf{x}\} = \{\alpha_1,\ \alpha_2,\ \alpha_3,\ \alpha_4\}^T$, where α_i represents the orientation angle of the i-th bushing ($i = 1, 2, 3, 4$) with the lower and upper bounds being $-\pi/2$ and $\pi/2$

for all orientation angles. Four design objectives are considered as follows:

1) The maximum body C.G. displacement should not exceed 20 mm.

2) The fundamental eigenfrequency of the system should be greater than 10 Hz.

3) The critical buckling force should be greater than 100 kN.

4) The maximum bushing force should be less than 12 kN.

Note that the above listed objectives are only for demonstration purposes, and may not reflect the actual requirements of the EMS design.

The original design assumes that all four bushings are oriented with their axial directions parallel to the X-axis of the global coordinate system, i.e., $\{\mathbf{x}\} = \{0, \quad 0, \quad 0, \quad 0\}^T$. This design provides a very weak support for the vessel along the forward-afterward direction, which results in a maximal 45mm forward-afterward movement of the vessel when the G-force is applied along the same direction.

To improve the EMS design, firstly, a design optimization is carried out to minimize the body C.G. displacement for the G-force along the X-direction, i.e.,

$$\underset{\mathbf{x}}{\text{Minimize}} \quad f(\mathbf{x}) = \{f_1(\theta), \ \theta = 0\} \tag{4.47}$$

The optimal angles obtained are listed in Table 4.2, which shows that all bushings should be oriented at nearly 90 degrees. This new design is referred to as Design 1. The objective function of the new design has been improved from the original 45 mm to 5 mm in this case for the given loading direction. However, the optimality of this design is highly dependent on the loading direction assumed.

Table 4.2: Optimal values for different objectives

Design case	Design description/design objectives	Optimal angles (deg)
0	Original design	[0.0 0.0 0.0 0.0]
1	Minimizing the amplitude of the body C.G. displacement while $\theta = 0^\circ$	[83.0 86.8 -81.7 -87.2]
2	Minimizing the amplitude of the body C.G. displacement for arbitrary θ	[61.6 -28.4 -4.5 85.5]
3	Maximizing the fundamental eigenfrequency	[-53.8 43.7 40.9 -52.7]
4	Maximizing the mean value of all the six eigenfrequencies	[-47.7 51.1 41.3 -46.2]
5	Maximizing the critical buckling force	[-81.9 65.3 62.4 -72.3]
6	Minimizing the maximum bushing force	[85.9 69.1 -89.9 72.5]
7	Maximizing the mean value of all the six eigenfrequencies while constraining the maximum bushing force transmitted through each bushing	[24.3 82.3 15.4 -37.7]

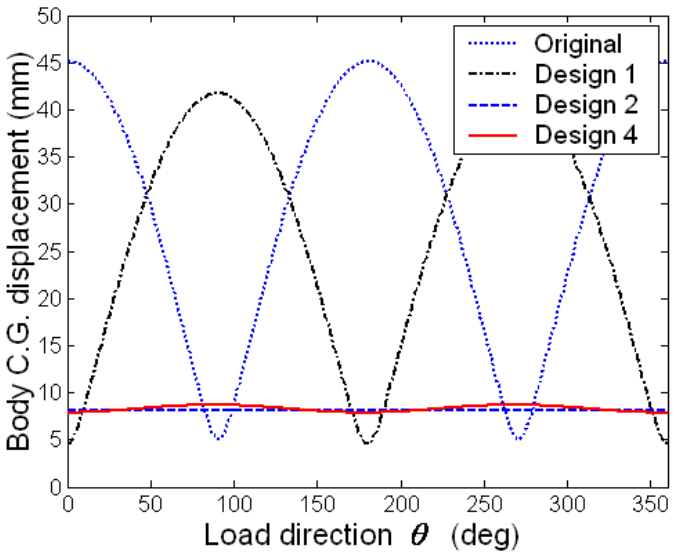

Figure 4.5: Load-dependent designs of the example EMS

Figure 4.5 illustrates the variation of the body C.G. displacement in different

loading directions. It is obvious that both the original design and Design 1 are highly load-dependent, that is, they produce small displacement only for certain loading directions. Both designs may fail to meet the design objective if the load is applied along a totally different direction.

Secondly, we allow the load to vary in its direction, and to minimize the maximal body displacement with respect to all possible load directions. The optimization problem is then given as

$$\underset{\mathbf{x}}{\text{Minimize}} \ f(\mathbf{x}) = \max\left\{ f_1(\theta), \text{ for all } \theta \right\} \tag{4.48}$$

It can be seen from Fig. 4.5 that the new design (which is referred to as Design 2), will eliminate the load-dependency of the original design and Design 1. The maximum body C.G. displacement is 8.2 mm for all possible loading directions, which can satisfy the design objective.

In order to meet the eigenfrequency requirement, thirdly, two optimization processes are carried out to maximize the eigenfrequencies of the EMS. Design 3 serves to maximize the fundamental eigenfrequency with an optimization problem defined as

$$\underset{\mathbf{x}}{\text{Maximize}} \ f(\mathbf{x}) = \lambda_1 \tag{4.49}$$

Design 4 is developed to maximize the mean-value of all of the six eigenfrequencies of the system. The design problem is defined as

$$\underset{\mathbf{x}}{\text{Maximize}} \ f(\mathbf{x}) = \left(\sum_{i=1}^{6} \frac{1}{\lambda_i} \right)^{-1} \tag{4.50}$$

The optimization results for Design 3 and Design 4 are listed in Table 4.3. It is seen that the lowest eigenfrequency can be increased to more than twice the original value. We noticed that the optimal value obtained in Design 4 is very close to that obtained from Design 3; this is because the lowest eigenfrequency λ_1 has a large contribution to the mean-eigenvalue defined in Eq. (4.50). It will be shown later that Design 4 is slightly better than Design 3 in terms of all other objectives considered (refer to Table 4.3).

Table 4.3: Comparison of design objectives with different designs

Design case / **Objectives**		0	1	2	3	4	5	6	7
Maximum body C.G. displacement (mm)		45.1	41.8	8.2*	9.1	8.7	22.1	47.4	16.6
Natural frequencies (Hz)	**1**	7.4	7.7	14.9	16.4*	16.4*	10.6	7.1	10.4*
	2	16.2	16.6	16.7	16.4	16.8*	16.5	16.5	16.2*
	3	16.8	21.6	17.4	18.0	17.7*	21.8	22.2	19.1*
Critical buckling force (MN)		1.2	1.5	2.4	2.6	2.6	2.6*	1.0	1.0
Maximum bushing force (kN)		8.6	11.8	11.5	12.9	12.5	14.7	7.4*	11.0*

Note: numbers with asterisks (*) are objectives or constraints.

Design 4 will also eliminate the load-dependency of the original design for the quasi-static loading case as shown in Fig. 4.5. This can be interpreted by the fact that the eigenfrequencies of the system represent the system stiffness in a global sense, and this characteristic is independent of the external loads. Moreover, Design 4 results in smaller body C.G. displacement than Design 3 (see Table 4.3) since it also increased higher eigenfrequencies of the system.

Design 5 serves to maximize the critical buckling force so as to obtain the most stable EMS. The optimization problem is given as

$$\underset{\mathbf{x}}{\text{Maximize}} \; f(\mathbf{x}) = \lambda_b \tag{4.51}$$

where λ_b is defined in Eq. (4.22), and the optimization is for all possible loading directions. Figure 4.6 shows the critical buckling force obtained from the design process, and compares it with the critical buckling force when the original design or Design 4 is used. It can be seen that the original design yields a low buckling force when θ is near 90° and 270°. This can be explained as follows: when force is applied along these two directions, the mounting system along the direction of force is much stiffer than that of the perpendicular direction; the system, however, has only a very small resistance to the yaw motion of the vessel. This results in a condition of very low stability for the system. It is also seen from Fig. 4.6 that the optimal design can significantly improve the stability by a factor of nearly three. It is important to note that Design 4 (from the eigenvalue optimization) is as good as the current design (Design 5). This indicates that maximizing system eigenvalues can also improve the stability of the system.

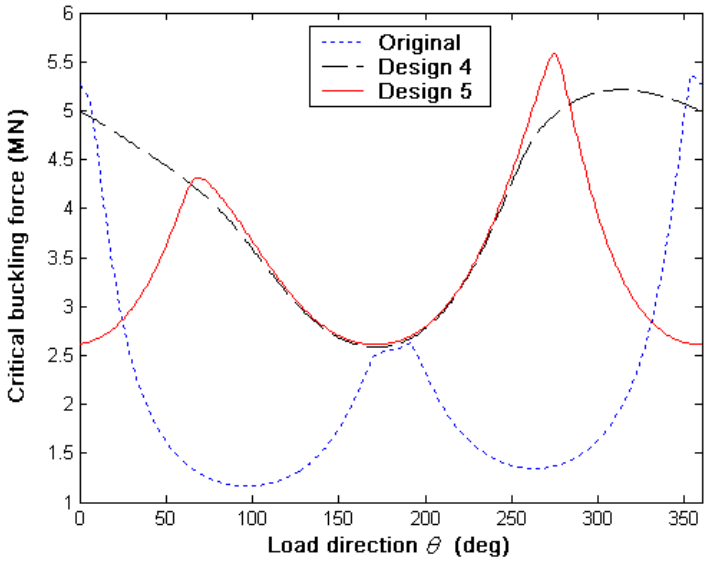

Figure 4.6: Comparison of critical buckling force in different designs

Figure 4.7 illustrates the dependency of the critical buckling force on the axial stiffness of the bushings. It is obvious that the stability of the original design strongly depends on the axial stiffness of the bushings. This indicates that when the axial stiffness becomes smaller and smaller, the stability of the system will become a critical issue, although the current system does not have a stability problem. Figure 4.7 also shows that Design 5 results in a buckling force that is linearly dependent on the axial stiffness, but with a much higher minimum value. At the same time, Design 4 has almost no dependency on the variation of the axial stiffness. In other words, Design 4 is a much better design in terms of absorbing the uncertainty of the bushing stiffness.

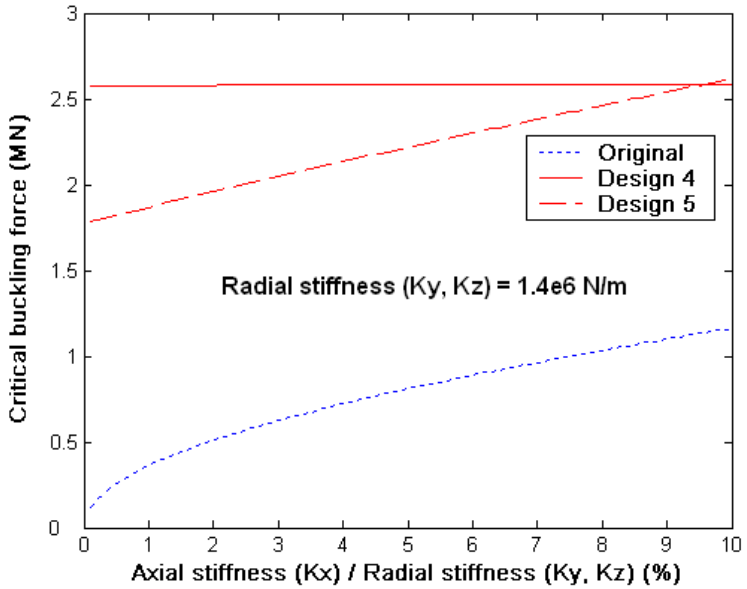

Figure 4.7: Comparison of critical buckling force in different designs by considering variation of bushing axial stiffness

From the above study, keeping in mind the objectives reduction approach (ORA), as proposed in section 2.8, we conclude that the first three design objectives are consistent and can be included in the same group, say, group 1. Maximizing the mean eigenfrequency of the system (Design 4) is chosen as a representative objective of the group, because the resulting design can meet all the first three design objectives. With this, our design task becomes much simpler.

The last single design task is to minimize the forces transmitted through the bushings. The goal is to minimize the maximum bushing force carried by all of the bushings. This objective is set to reduce the failure of the bushing. For this purpose, the design problem is defined as

$$\underset{\mathbf{x}}{\text{Minmize}}\ f(\mathbf{x}) = \max\{\overline{F}_i(\theta), i = 1, 2, 3, 4 \text{ and for all } \theta\} \tag{4.52}$$

The resultant design (Design 6) has significantly reduced the maximum bushing

forces, for example, from 14.7 kN in Design 5 to 7.4 kN in the current design (and other comparisons are shown in Table 4.3). However, as can be seen in Table 4.3, the new design turns out to be a poor design with respect to the other three design objectives considered in this example. It is also seen in Table 4.3 that Design 4 is good for the first three design tasks, but it is among the worst for the last objective (minimizing the maximum bushing force). Keeping the ORA in mind, we can conclude now that the last design objective is in a different group, say, group 2, which is in conflict with group 1 as defined before. There are some trade-offs between the two groups. In order to meet the requirements of the multidisciplinary objectives using one design, we define an optimization problem, which constrains the maximum force transmitted through each bushing to 11 kN and maximizes the mean-eigenvalue defined in Design 4, namely,

$$\begin{aligned} &\underset{\mathbf{x}}{\text{Maximize}} \;\; f(\mathbf{x}) = \left(\sum_{i=1}^{6} \frac{1}{\lambda_i} \right)^{-1} \\ &\text{Subject to} \;\; \bar{F}_i(\theta) \le 11 \text{ kN}, \;\; (i = 1,2,3,4 \text{ and for all } \theta) \end{aligned} \tag{4.53}$$

The final results are listed in Table 4.2 as Design 7, which has met all of the design objectives; it is, therefore, considered as the final design to be obtained from the design process. Figure 4.8 compares the maximum bushing forces obtained for three different designs (Design 4, 6, and 7) in terms of the loading direction. Note that different design requirements may result in a different design decision. However, the process proposed in this work is general enough to deal with various design requirements.

Table 4.2 summarizes the results for all of the design cases considered in this

example. Table 4.3 summaries the objective values obtained for different designs.

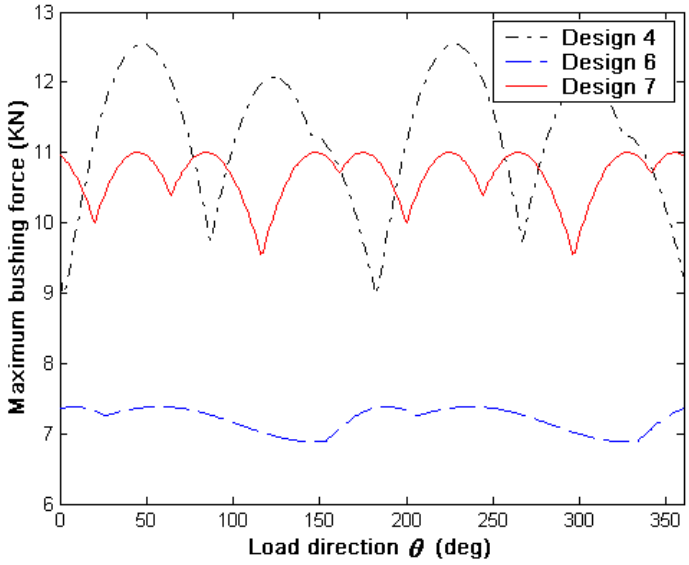

Figure 4.8: Comparison of maximum bushing force with different designs

The design sensitivity analyses for the final design (Design 7) are performed for the quasi-static response. Figure 4.9 illustrates the sensitivity of the body C.G. displacement with respect to the four design variables. As shown in Fig. 4.9, body C.G. displacement is more sensitive to the orientation angle of the bushing 1. The sensitivity analyses will have two usages here: 1) to determine the influence of the design variables if additional design changes are required, and 2) to predict which design variable will have the largest effect on the uncertainty of the final design. Similar sensitivity analyses can be performed for other objective functions, but they are omitted here.

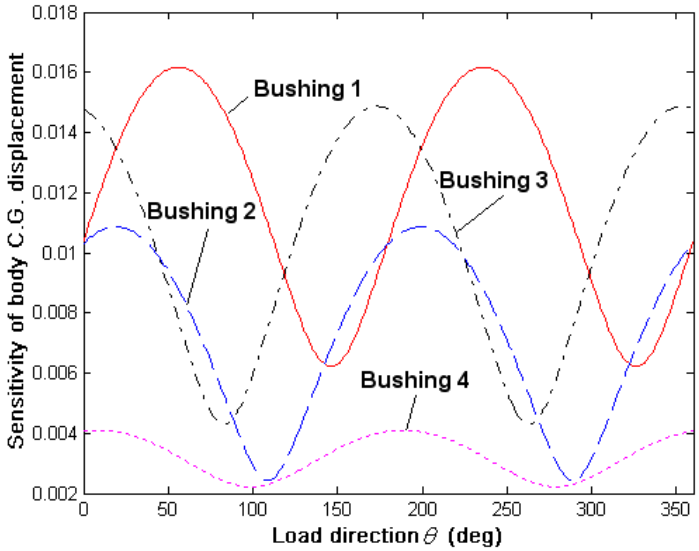

Figure 4.9: Design sensitivity of body C.G. displacement on bushing orientation angles

It is crucial to provide a reliability assessment for the optimal design. In this study, only the reliabilities with respect to the four design variables $\alpha_i, (i = 1,2,3,4)$ are considered. It is assumed that all four design variables are normally distributed with the same standard deviation of five degrees. The mean values of these design variables are the optimization results of Design 7. Figure 4.10a shows an example probability density distribution of the first design variable.

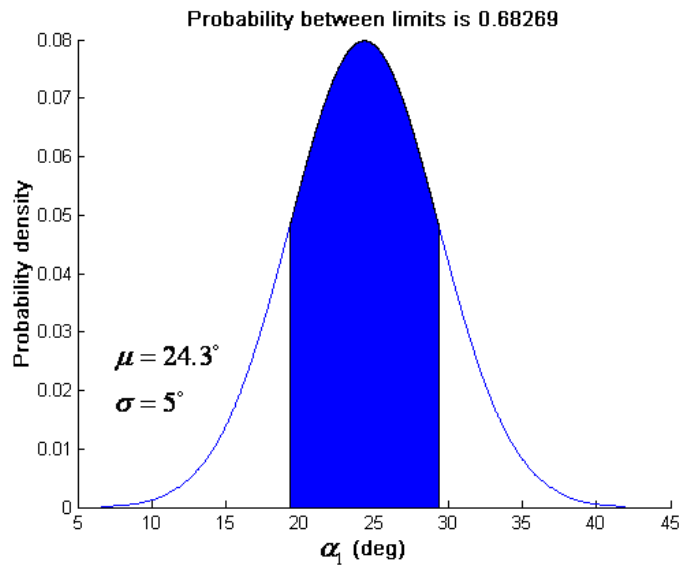

(a)

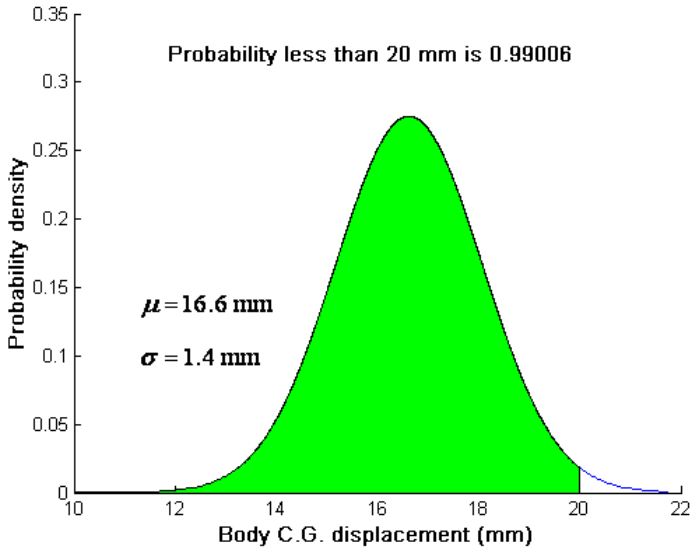

(b)

Figure 4.10: Reliability assessment of the example EMS design: (a) design variable probabilistic distribution; and (b) body C.G. displacement probabilistic distribution.

We then calculated the design reliabilities for all four objectives defined in this example, namely, body C.G. displacement, fundamental eigenfrequency, critical buckling force, and the maximum bushing force. First, we assume that the example EMS will fail if the body C.G. moves a distance of more than 20 mm. The probabilistic performance measure is then defined as

$$G_1(\mathbf{X}) = \frac{20 \text{ mm}}{d} - 1 \tag{4.54}$$

The probability of failure p_f is next obtained by using the Monte Carlo simulation, which is 0.01 with the reliability $R = 1 - p_f = 0.99$. Figure 4.10b shows the probability density distribution of the body C.G. displacement. The result indicates that the system response in terms of the body C.G. displacement has 99% reliability if the optimal design is used.

Secondly, consider the reliability in the case where the first eigenfrequency of the system is greater than 10 Hz; the probabilistic performance measure is then defined as

$$G_2(X) = \frac{\lambda_1}{10 \text{ Hz}} - 1 \tag{4.55}$$

By using the Monte Carlo simulation, we have $p_f = 0.26$, and $R = 1 - p_f = 0.74$, which means that the optimal design has 74% reliability with respect to the first eigenfrequency of the system.

The probabilistic performance measure for the critical buckling force is defined as

$$G_3(X) = \frac{\lambda_b}{100 \text{ kN}} - 1 \tag{4.56}$$

We find $p_f = 0.0$ and $R = 1 - p_f = 1.0$, which means the optimal design is completely reliable when the critical buckling force is considered.

Finally, the probabilistic performance measure for the maximum bushing force is defined as

$$G_4(X) = \frac{12 \text{ kN}}{\max(\bar{F}_i(\theta),\, i = 1, \ldots, 4)} - 1 \text{ for all } \theta \tag{4.57}$$

We now have $p_f = 0.43$ and $R = 1 - p_f = 0.57$, which means the optimal design is 57% reliable in terms of the maximum bushing force.

In this design problem, approaches related the following layers of the magic cube have been employed: *optimization technique, multidisciplinary objectives, loadings,* and *uncertainties.* The employed approaches are depicted in the magic cube as shown in Fig. 4.11.

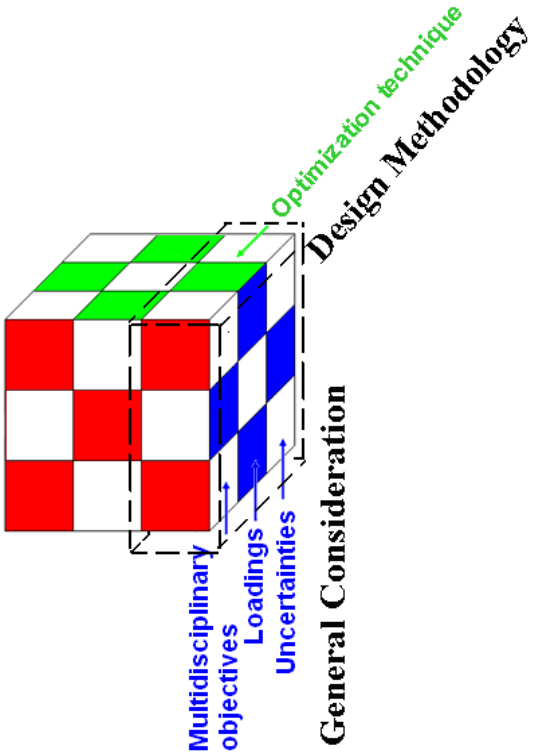

Figure 4.11: Elements of the magic cube for the EMS design problem

4.2 Design for Weight Reduction via Material Substitution

4.2.1 Industry Background

A practical problem from automotive industry is how to substitute the traditionally used mild steel in a truck (frontal) frame with the high strength steel (HSS), without debasing the crash performance of the vehicle. The aim is to reduce

the weight of the vehicle (frame) through down-gauged wall thickness of the (frontal) frame using HSS. The *space decomposition* and *target cascading* in the MQ approach are employed to assist the problem solving as demonstrated in the following.

4.2.2 Simulation Model

The FE model of the representative vehicle developed in Chapter III is employed in the current problem as the baseline design; the crash performance of the vehicle has been simulated using LS-DYNA as shown in Fig. 3.1.

4.2.3 Building Subsystem Model Using Space Decomposition

To simplify the design process, the *space decomposition* approach is employed to obtain the frontal frame subsystem model shown in Fig. 4.12. The crash performance of the frontal frame predicted by this subsystem model should represent that expected according to the vehicle system model, including the deformed shape of the frontal frame, the crash load level, and the energy absorption level, etc. This is ensured by the target cascading process, and realized by applying the appropriate boundary conditions to the frontal frame subsystem model, conditions such as attaching proper masses and constraining corresponding DOF at the rear end of the frontal frame, as shown in Fig. 4.12.

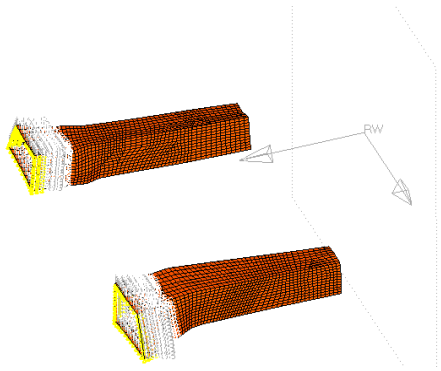

Figure 4.12: The frontal frame subsystem model after space decomposition

(a)

(b)

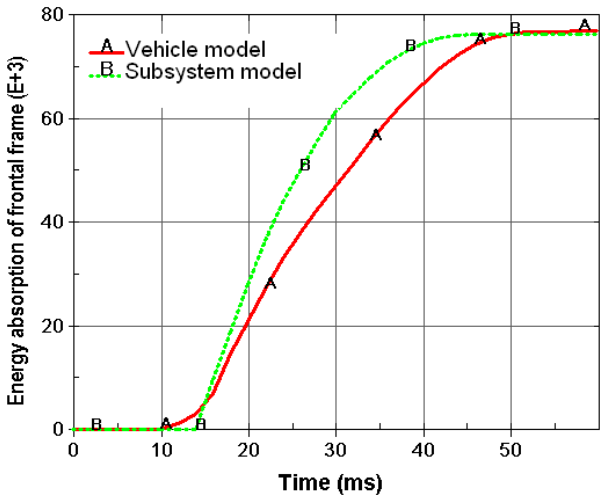

(c)

Figure 4.13: Validation of the frontal frame subsystem model: (a) deformed shape in vehicle model; (b) deformed shape in subsystem model; and (c) energy absorption histories.

To validate the subsystem model, the deformed shape and the crash energy absorption history of the frontal frame predicted by both the subsystem model and the vehicle model are compared in Fig. 4.13. It is seen that the deformed shape and the energy absorption history of the frontal frame predicted by these two models match very well. Once validated, this high fidelity frontal frame subsystem model can be utilized in the design process with much less computational cost than the vehicle model. *Space decomposition*, again, helps to simplify the design problem.

4.2.4 Analytical Model for Design

For design purposes, an analytical formulation developed by Wierzbicki and Abramowicz [85] is employed to predict the mean crash force of the frontal frame. For the crushing of a box column of a rectangular cross section $c \times d$, and wall thickness of H, the mean crash force P_m can be predicted as

$$P_m = 13.05\sigma_0 H^2 (C/H)^{1/3}\{1+(0.33V/CD)^{1/q}\} \tag{4.58}$$

Here, $C = 1/2(c+d)$, V is the impact velocity, and σ_0 is the plastic flow stress of the material; for elastic-perfectly plastic material, $\sigma_0 = \sigma_y$, and σ_y is the yield stress of the material; for work-hardening material, such as HSS, the plastic flow stress σ_0 has a value between σ_y and the ultimate stress σ_u, as illustrated in Fig. 4.14.

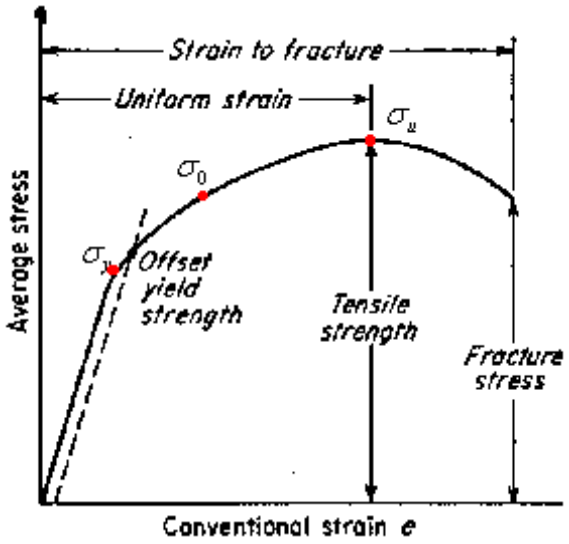

Figure 4.14: The plastic flow stress on the engineering stress-strain curve

We assume

$$\sigma_0 = \sigma_y(1-\lambda) + \sigma_u\lambda \tag{4.59}$$

where λ is defined as the material index, which depends on the type of HSS in use. The crash force vs. displacement of the baseline design of the frontal frame is shown in Fig. 4.15; from this curve, the mean crash force can be obtained as $P_m = 355\,\text{kN}$.

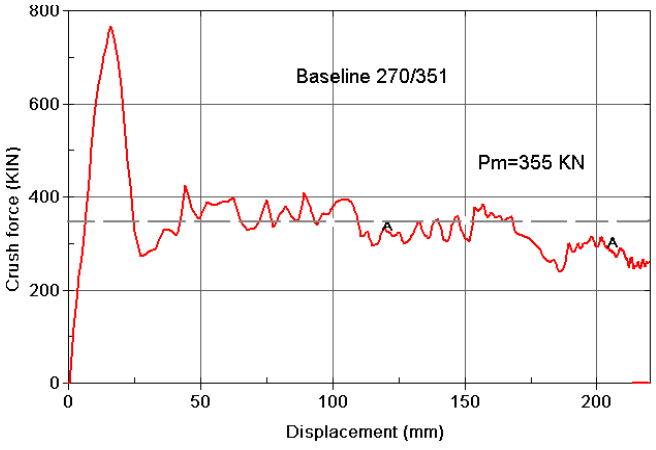

Figure 4.15: Crash force vs. displacement of the baseline design

For the baseline design, H =3.137 mm, and C =110 mm, which is an

approximate characteristic dimension of the example frontal frame. The material used in the baseline design has a yield stress $\sigma_y = 270$ MPa , and ultimate stress $\sigma_u = 351$ MPa . By substitute Eq. (4.59) into Eq. (4.58), the material index can be expressed as

$$\lambda = \frac{P_m}{13.05(\sigma_u - \sigma_y)H^2(C/H)^{1/3}\{1+(0.33V/CD)^{1/q}\}} - \frac{\sigma_y}{\sigma_u - \sigma_y} \tag{4.60}$$

Using Eq. (4.60), the material index for the steel used in the baseline design can be identified as λ=0.8. The plastic flow stress of the steel is then estimated as 334.8 MPa using Eq. (4.59).

4.2.5 Design Results

The properties of all HSS with various yield and ultimate stresses employed in the current study are listed in Table 4.4.

Table 4.4: Properties of steels used in the example design problem

No.	Steel grade	σ_y (MPa)	σ_u (MPa)	Total elongation	n Value (5-15%)	r (Bar)	K value (MPa)
0	Baseline	270	351				
1	DP 300/500	300	500	30-34	0.16	1	762
2	DP 400/700	400	700	19-25	0.14	1	1028
3	DP 500/800	500	800	14-20	0.14	1	1303

Figure 4.16 shows the crash force vs. displacement of a design using HSS DP 300/500 and the wall thickness of the baseline design, which is $H = 3.137$ mm . The

mean crash force for this design is calculated as P_m=439 kN. The material index of HSS DP 300/500 is then identified as $\lambda = 0.6$ using Eq. (4.60), and the plastic flow stress of HSS DP 300/500 is obtained as $\sigma_0 = 420$ MPa using Eq. (4.59).

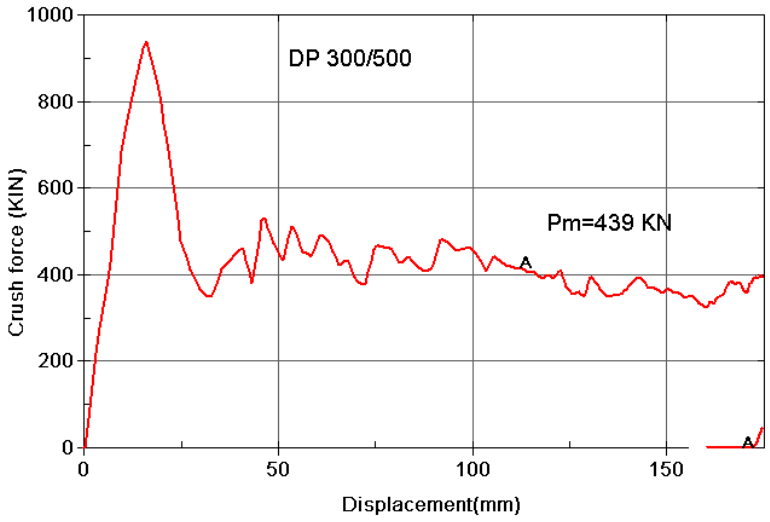

Figure 4.16: Crash force vs. displacement with HSS DP300/500 and wall thickness of the baseline design

The mean crash force of the baseline design is set to be the design objective represented as $P_{m\_obj} = 355$ kN. The reduced wall thickness of a design with HSS to achieve the target mean crash force can be obtained using

$$H = \left\{ \frac{P_{m\_obj}}{13.05\sigma_0 C^{1/3}\left[1+(0.33V/CD)^{1/q}\right]} \right\}^{3/5} \tag{4.61}$$

which is a recast of Eq. (4.58). For a design with HSS DP300/500, the down-gauged wall thickness of the frontal frame is obtained as H=2.75 mm.

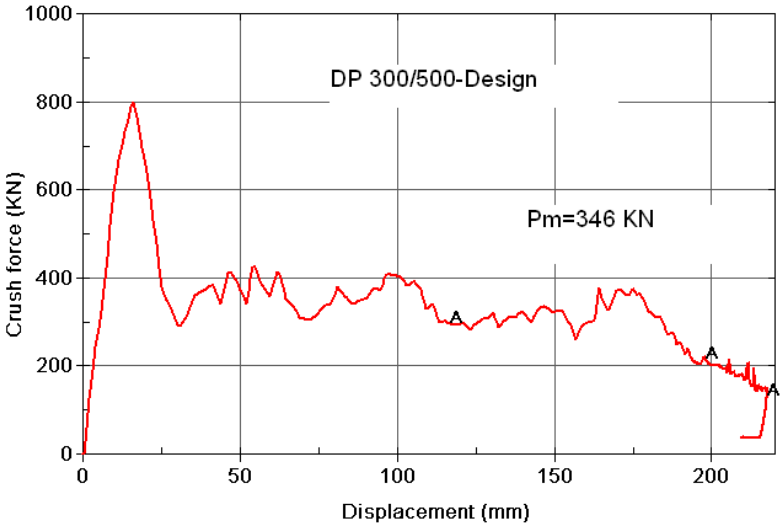

Figure 4.17: Crash force vs. displacement with HSS DP300/500 and down-gauged wall thickness

Figure 4.17 plots the crash force vs. displacement of a designed frontal frame with HSS DP300/500 and down-gauged wall thickness; the mean crush force is obtained as 346 kN, which is only 2.5% lower than the objective value. After substituting the designed frontal frame subsystem with HSS DP300/500 back into the vehicle model, the energy absorption history of the subsystem is predicted using the vehicle model, as shown in Fig. 4.18. It is seen that the design with HSS DP300/500 and the wall thickness of the baseline design decreases the energy absorption level of the frontal frame subsystem in the whole vehicle system, compared to the baseline design; while a design with down-gauged wall thickness pushes the energy absorption level back to where it was in the baseline design, meaning the same crash performances results from each of the two designs.

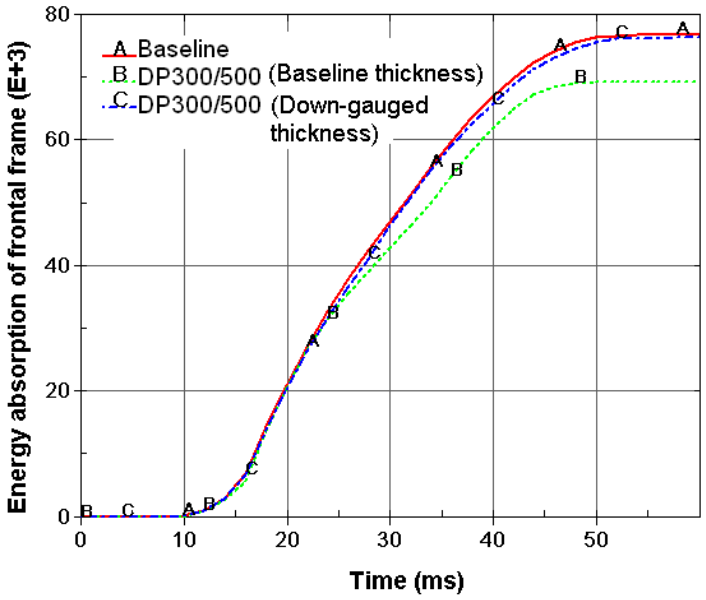

Figure 4.18: Energy absorption histories of the frontal frame with different designs using the vehicle model

Table 4.5: Weight reduction of the frontal frame in designs with various HSS

Design case	Steel grade	Weight reduction (%)
0	Baseline	0
1	DP 300/500	12.3
2	DP 400/700	24.1
3	DP 500/800	29.9

Table 4.5 summarizes the percentages of the weight reduction of the frontal frame with designs using various HSS. The higher the yielding stress and the greater the ultimate stress of the material in usage, the more weight reduction a design can achieve with the same level of crash performance.

4.3 Conclusions

Quasi-static, frequency response, and eigenvalue analyses of a general purpose

elastomeric mounting system was presented. Elastic stability of the EMS was investigated for the first time with the development of a general formulation that determines the critical buckling force and buckling mode of the system. The optimization problem of EMS was defined with multidisciplinary design objectives. Design sensitivities of the multidisciplinary objectives were derived. An example EMS in an innovative concept vehicle was optimized to meet multidisciplinary design objectives with the implementation of the proposed objectives reduction approach (ORA), showing the feasibility and effectiveness of the ORA in handling such a multidisciplinary design problem. Reliability assessment of the optimal design was conducted in order to consider uncertainties of the system parameters that may arise due to manufacturing and assembling variations. The developed formulations and approaches can be applied to a wide range of EMS design problems including body mounting systems and power-train mounting systems.

In another industry application problem, high strength steel (HSS) materials were used as a substitute for the baseline mild steel material utilized in the frontal frame of a representative vehicle, and *space decomposition* and *target cascading* in the MQ approach were employed to assist the design process. Weight reductions of the vehicle (frontal frame) were achieved without diminishing the crash performance.

CHAPTER V

Blast Protection Design Using the Magic Cube Approach

In this chapter, the Magic Cube (MQ) approach is employed to assist in a complicated blast protection design of a military vehicle system; one major design objective is to reduce the weight of the underbody armor structure of the vehicle while taking into consideration of loading uncertainties.

This chapter is organized as follows: blast load, blast injury mechanisms, and occupant injury assessments are introduced first, followed by the numerical models for blast simulations that were developed based on the LS-DYNA system. The *space decomposition* in the MQ approach is then employed to decompose the complicated blast protection system into three subsystems, which are driver seat, restraint system (seat belts), and underbody armor structure, respectively. The effects of seat design and restraint system on blast protection capabilities of the vehicle system are briefly discussed. The rest of this chapter is dedicated to the design of the underbody armor structure for weight savings with consideration of loading uncertainties.

5.1 Blast Load and Blast Injury

5.1.1 Blast Load

Blast load is a type of extraordinary dynamic load that results from an explosion, in which a great deal of energy is released within a very short period of time. (The duration of a blast can be less than 1.0 ms). The analytical modeling of blast has been done by Kingery [86] and Beshara [87] [88]. The incident portion of the blast wave is called the "shock front." When the shock wave of an air burst leaves the point of the explosion, it travels as an incident wave until it strikes some object. Upon striking the object, a reflected wave is generated, which travels back towards the explosion's origin. At some point, a certain distance from the explosion's center, the reflected wave catches up with the incident wave, producing a single vertical wave front called "Mach Stem." Structures below the point of the intersection of the reflected wave and the incident wave will experience a single shock, whereas surfaces or objects above this point will experience a shock that results from the incident and reflected waves. At a reasonable distance from the center of the explosion, blast waves from any explosive source have the same behavior. Figure 5.1 illustrates the pressure-time history of a blast wave. The pressure jumps to the peak value of the overpressure, P_0, within a very short period (less than 0.1 ms). The pressure then decays to atmospheric pressure with $p = 0$, at time t_0. After that, the pressure decays to a partial vacuum of very small amplitude and eventually returns back to atmospheric pressure. The portion of the pressure-time history below zero is called the "negative phase" and the portion above zero is called the "positive

phase." In most blast studies the negative phase of the blast wave is ignored, with only the phenomena associated with the positive phase being considered.

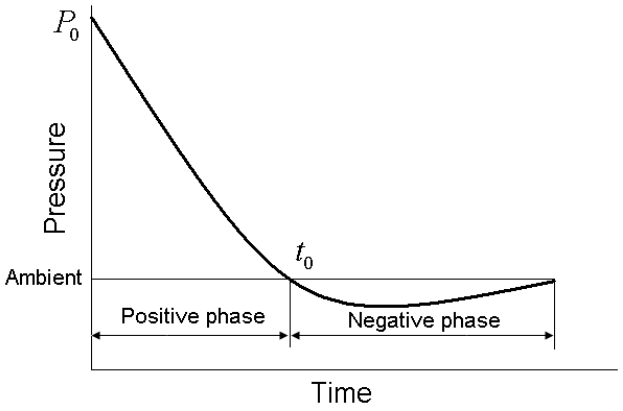

Figure 5.1: Blast pressure-time evolution

In the positive phase, the pressure p at any time t is described in terms of the peak overpressure P_0, a dimensionless wave form parameter k, and a positive phase duration time t_0. Two functions are often used for calculating the positive pressure:

$$p = P_0(1 - t/t_0) \tag{5.1}$$

which is a simple triangular form, or more accurately,

$$p = P_0(1 - t/t_0)e^{-kt/t_0} \tag{5.2}$$

By selecting a value for k, various decay characteristics can be indicated. Curves with very rapid decay characteristics are typical of nuclear explosions, and curves with slower decay rates are typical of explosions with large volumes of product gases.

Theoretically, for a perfectly spherical charge in the air, the relationship between P_0, the distance of the point of measure from the centre of the explosion R, and the

instantaneous energy release E, take the form

$$p_0 = KE / R^3 \tag{5.3}$$

Here, K is a non-dimensional parameter, and E is measured in joules. Experiments show that the explosion of TNT generates blast energy of approximately 4600 joules/gram. In fact, the definition of a "standard" gram of TNT is that which yields blast energy of 4610 joules. The definition of a standard ton of TNT is an energy release of one million kilo-calories. Taylor [89] gave the relationship as

$$P_0 = 0.155E / R^3 \tag{5.4}$$

The peak pressure at radius R does not depend on atmospheric density, whereas the time t since the beginning of the explosion for the shock front to reach a radius R depends on $\rho_a^{1/2}$ and is given by

$$t = 0.926\, R^{5/2} \rho_a^{1/2} E^{-1/2} \tag{5.5}$$

when the ratio of specific heats, $\gamma = 1.4$ and ρ_a is the density of air.

5.1.2 Blast Injury Mechanisms

Blast load from conventional mines can damage a vehicle system and injure personnel through the following mechanisms:

1) Blast overpressure: landmine blasts enter through the floor and firewall and blow out the windows; this can cause ear and lung damage;

2) Vehicle shock acceleration and deformation: the floor acceleration and deformation cause substantial lower leg injuries to the occupants;

3) Gross vehicle movement: lower leg, spinal, and head injuries result from

large gross vertical movement upward and the subsequent return to the ground;

4) Loss of vehicle control: the sudden change of direction because of blast force can result in a rollover accident;

5) Fragmentation: fragments are generated when landmines are detonated under tires. Large pieces of tires or parts of the wheel or brakes can penetrate the floor and kill occupants.

5.1.3 Blast Injury Assessment

The goal of blast protection design of a vehicle system is to minimize crew injury levels under blast loads as much as possible. Due to the novelty of this research field, as well as the confidential nature of most research conducted, minimal data are available for injury assessment under blast loads. The injury criteria used for the head and pelvis were developed by Alem [90] using the Hybrid III ATD dummy; Black et al. [91] and Draeger et al. [92] obtained feet injury criteria based on experimentation with cadavers. It is worth noting that in most cases, the loading rates and event durations involved with mine blast loading fall well outside the rates and durations used to develop the injury criteria available.

In this research, based on the fact that most blast loads come from underneath a vehicle system, injury indices such as pelvis acceleration and feet velocities are used for design assessments. The kinetic energy of the whole body of a crew member is also used as an injury assessment index in cases when detailed injury assessments of specific body parts are not necessary for design assessment.

5.2 Numerical Models

The development of a comprehensive blast protection system requires the understanding of the blast loading effects on the vehicle structure and the crew. The blast process is both difficult and expensive to test. Moreover, testing of (vehicle) structural damage processes from the blast loads are no easy task either. Numerical techniques, such as the FE method, are employed for blast process simulation as well as for structural damage analyses.

5.2.1 Blast Simulation Models

For blast simulation, several hydrodynamic codes, including CTH, AUTODYN, and LS-DYNA, are capable. Existent numerical models developed for blast simulations can be roughly divided into two categories: the numerical models based on the Lagrange/Euler method, and the empirical models for blast pressure approximation.

Arbitrary Lagrangian-Eulerian (ALE) Model

For blast impact simulation, the complexity of the problem lies in the following difficulties: the high speed wave front propagation, the flow of various materials, and the large structural deformation. Currently, the most appropriate numerical method for this type of problem is the Arbitrary Lagrangian Eulerian (ALE) method.

In a numerical model of a continuum, the material is divided into discrete finite sections, over which the conservation and constitutive equations are solved. The scheme of spatial discretization leads to different numerical methods. Lagrangian

meshes are used to treat many problems effectively. But in the cases where the material is severely deformed, Lagrangian elements become similarly distorted since they deform with the material. The approximation accuracy of the elements then deteriorates, particularly for higher order elements. Furthermore, the Jacobian determinants may become negative at quadrature points, either aborting the calculations or causing severe local inaccuracies. These types of problems are more suited to Eulerian elements. In Eulerian meshes, the elements are fixed in space and material convects through the elements. Eulerian finite elements thus undergo no distortion due to material motion; however, the treatment of constitutive equations and updates is complicated because of the convection of material through the elements. The Arbitrary Lagrangian Eulerian (ALE) methods that have been developed combine the advantages of Eulerian and Lagrangian methods. The ALE solver allows for a type of "automatic remapping" in the simulation. For a blast simulation, the vehicle structure can be completely Lagrangian (the nodes move with the material motion), while the detonation material (TNT) and the surrounding fluid (air, water, etc.), using the Eulerian mesh, can be remapped during simulation so that severe distortion is avoided.

The ALE method has been implemented in the hydrodynamics code CTH as well as in some commercial codes, such as LS-DYNA. In the LS-DYNA ALE model, both the Eulerian mesh modeling the explosive charge and the surrounding fluid (water, air), and the Lagrangian mesh of the investigated structure, need to be generated. The time and space distribution of the blast pressure profile are

calculated through the Eulerian mesh by utilizing the equation of state (EOS) for high explosives. The mix of the air and explosive reaction products is modeled using multi-material capabilities (*ALE_MULTIMATEIRAL_GROUP_OPTION) in LS-DYNA. The blast pressure wave traveling through the air interacts with the structure by means of a gas-structure interfacing algorithm in LS-DYNA (*CONSTRAINED_LAGRANGE_IN_SOLID). Physical quantities such as stress, displacement, velocities, and accelerations in the structure are computed.

At any given time, the pressure in a high explosive element is given by

$$p = Fp_{eos}(V, E) \tag{5.6}$$

where p_{eos}, is the pressure from the EOS (either type 2 or 3 in LS-DYNA); F, is called burn fraction, which multiplies the EOS for high explosive, and controls the release of chemical energy for simulating detonations.

The Jones-Wilkins-Lee (JWL) EOS model for explosive detonation product is given by [93]

$$p = A\left(1 - \frac{\omega}{R_1 V}\right)e^{-R_1 V} + B\left(1 - \frac{\omega}{R_2 V}\right)e^{-R_2 V} + \frac{\omega E}{V} \tag{5.7}$$

where, $p = p(x, y, z, t)$ is the pressure field, V is the volume of the material at pressure p divided by the initial volume of the un-reacted explosive, E is the internal energy per unit initial volume, and A, B, R_1, R_2 and ω are adjustable parameters. For example, for TNT, A=3.712 Mbar, B=0.0323 Mbar, $R_1 = 4.15$, $R_2 = 0.95$, and $\omega = 0.30$ [94].

The air is usually modeled to represent the medium in which the blast wave

propagates. A linear polynomial EOS is usually used to simulate the proper air behavior, and the pressure is given by

$$P = C_0 + C_1\mu + C_2\mu^2 + C_3\mu^3 + (C_4 + C_5\mu + C_6\mu^2)E \tag{5.8}$$

where $\mu = \frac{\rho}{\rho_0} - 1$ with $\frac{\rho}{\rho_0}$ being the ratio of current density to initial density, and $C_{(\bullet)}$ being constants. For gases to which the gamma law EOS applies, including atmospheric air, $C_0 = C_1 = C_2 = C_3 = C_6 = 0$, and $C_4 = C_5 = \gamma - 1$, with γ as the ratio of specific heats. Therefore, for air, Eq. (5.8) reduces to

$$p = (\gamma - 1)\frac{\rho}{\rho_0}E \tag{5.9}$$

The units of E are the units of pressure.

One drawback of the ALE method is its high computational cost, and it is therefore appropriate only for simulating blast events with small standoff distances, making it inappropriate for blast protection design purpose. For blast events with large standoff distances, as in the case of blast on a vehicle system, it is usually convenient to divide the blast simulation into two decoupled stages. The first stage is the blast load prediction, which aims to achieve the appropriate blast loads. The simulated blast loads will then be used as the input in the second stage to analyze structure and crew responses. Several empirical models have been developed for blast load prediction with acceptable accuracy and much less computational effort than the ALE model.

Empirical Model

One of the empirical models for blast pressure prediction is based on the CONWEP air blast function developed by Kingery and Bulmarsh [86]. This model, which has been implemented as the *LOAD_BLAST loading card in LS-DYNA, can predict the blast overpressure under certain conditions: the free air detonation of a spherical charge and the surface detonation of a hemispherical charge; the surface detonation approximates the conditions of a mine blast. The model takes into consideration the angle of incidence of the blast, θ, the incident pressure, p_{in}, and the reflected pressure, p_{ref}. The predicted blast overpressure is expressed as

$$p(t) = p_{ref}\cos^2\theta + p_{in}(1+\cos^2\theta - 2\cos\theta) \tag{5.10}$$

with p_{in} and p_{ref} given by

$$p_{in} = p_{i0}(1-t/t_0)e^{-bt/t_0}$$

$$p_{ref} = p_{r0}(1-t/t_0)e^{-at/t_0} \tag{5.11}$$

where p_{i0} and p_{r0} are the peak incident overpressure and the peak reflected overpressure, respectively. a and b are decay coefficients, and t_0 is the positive phase duration time.

The model uses the following inputs to calculate the pressure: equivalent mass of TNT; coordinates of the point of explosion; and the delay time between when the LS-DYNA solution starts and the instant of explosion. The model does not account for shadowing by the intervening objects or the effects of confinement.

In this work, the CONWEP empirical model is adopted for blast load prediction

by virtue of its computational efficiency and acceptable accuracy, which is verified by a benchmark problem as follows.

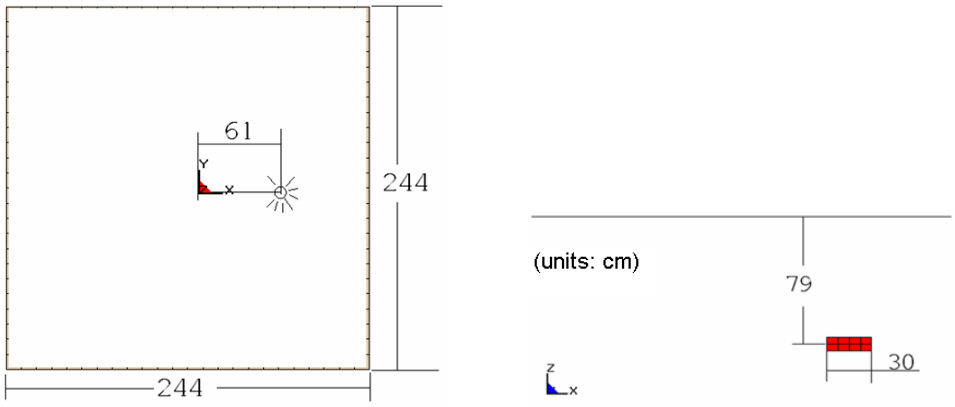

(a) (b)

Figure 5.2: A benchmark problem for blast simulation: asymmetric mine-plate interaction: (a) top view of configuration; and (b) side view of configuration.

As shown in Fig. 5.2, a square plate with sides of 244 cm, and a thickness of 15 cm is subjected to a free-air detonation; the mine contains an explosive with an equivalent charge weight of 9.05 kg TNT, which is asymmetrically located with a horizontal centerline offset distance of 61 cm relative to the center of the plate. The vertical distance between the middle-plane of the plate and the middle-plane of the mine is 79 cm. The cylindrical configuration of the mine has a diameter of 30 cm and a height of 8 cm.

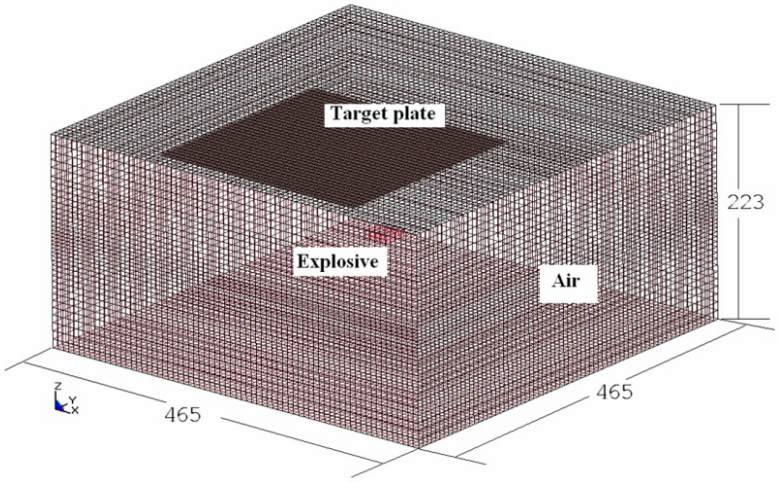

Figure 5.3: ALE model of the benchmark problem

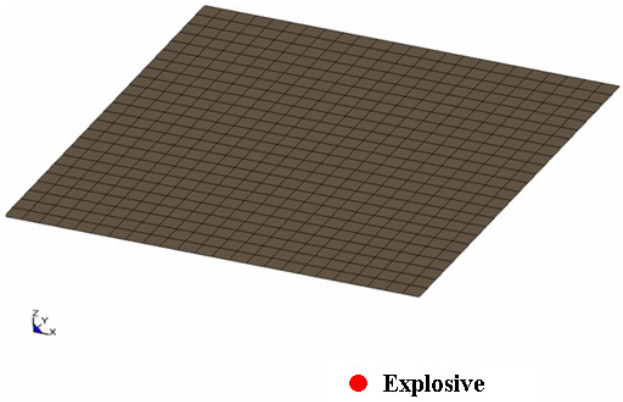

Figure 5.4: CONWEP model of the benchmark problem

The ALE model and the CONWEP model are developed for the simulation as shown in Fig. 5.3 and Fig. 5.4, respectively. Table 5.1 summarizes the material types, material properties, and EOS parameters for the ALE model in LS-DYNA.

Table 5.1: LS-DYNA material types, material property input data, and EOS input data for the ALE model of the benchmark problem [95]

Material	Dyna material types, material property input data and EOS input data (unit = cm, g, μs)								
C4	*MAT_HIGH_EXPLOSIVE_BURN								
	RO	D	PCJ						
	1.601	0.8193	0.28						
	*EOS_JWL								
	A	B	R1	R2	OMEG	E0	V0		
	6.0997	1.295E-1	4.50	1.40	0.250	9.00E-02	1.00		
Air	*MAT_NULL								
	RO	PC	MU						
	1.29E-3	0.0	0.0						
	*EOS_LINEAR_POLYNOMIAL								
	C0	C1	C2	C3	C4	C5	C6	E0	V0
	-1.0E-6	0.0	0.0	0.0	0.4	0.4	0.0	2.50E-6	1.0E+0
Steel	*MAT_PLASTIC_KINEMATIC								
	RO	E	PR	SIGY	ETAM	BETA			
	7.9	2.1	0.29	2.75E-3	0.021	1.00			

The simulated blast pressure contour on the target plate at a specific moment ($t = 0.4$ ms) is illustrated in Fig. 5.5. Figure 5.6 shows the plate momentum history in the Z direction resulting from the mine blast, as predicted by both the ALE model and the CONWEP model. Compared to the ALE model, the CONWEP model under-predicts the maximum plate momentum in this case, although good agreement has been achieved in the time scheme. After giving a scale factor of 1.2 to the CONWEP function, the maximum plate momentum can be obtained, similar to what was obtained from the ALE model. This benchmark problem shows that the CONWEP empirical model is capable of predicting the blast load on a general structural system, although scale factors may need to be determined beforehand to make the prediction more accurate. It is worth noting that the computational cost of the CONWEP model is much less than the ALE model in this benchmark problem simulation.

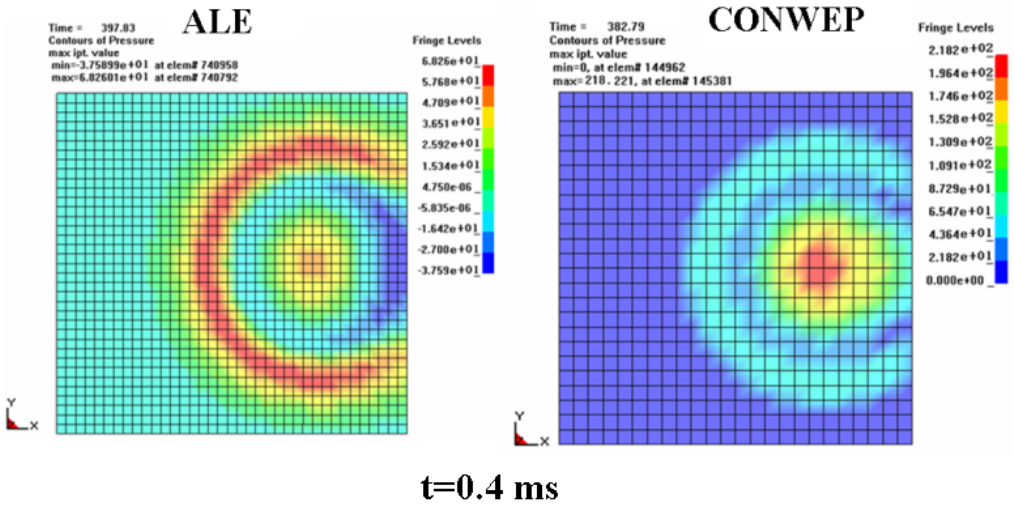

Figure 5.5: Pressure contour on the target plate predicted by the two models (unit: bar)

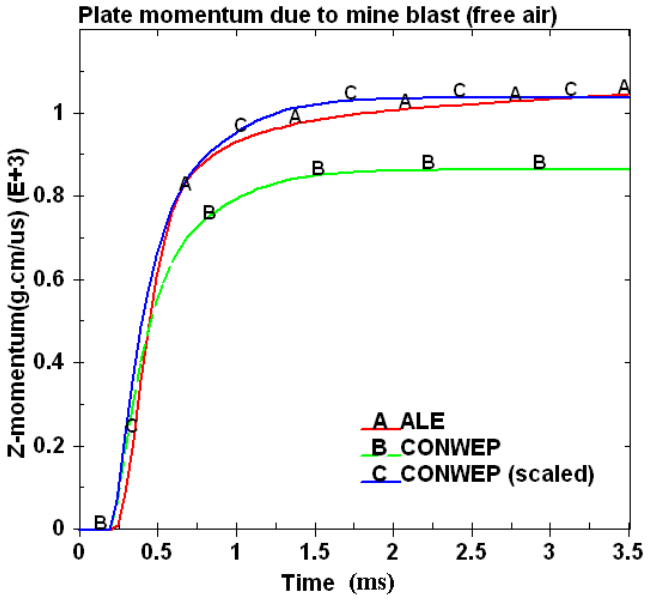

Figure 5.6: Comparison of plate momentum predicted by the two models

5.2.2 Dummy Model and Vehicle Model

Dummy Model

The ultimate goal of safety design is to protect the occupants of a vehicle from dangerous loads, either a crash load or a blast load. Crash test dummies (or dummy

models) are usually included in tests (or simulations) to predict occupant responses under different crash loads; these responses will be used to guide the crashworthiness design. Various dummy models for vehicle crashworthiness design have been developed, from very complicated FE models with thousands of DOF, to much simpler rigid body models. Figure 5.7 shows the 50th percentile male GEBOD dummy model; the model is comprised of fifteen rigid bodies (segments) that represent the lower torso, middle torso, upper torso, neck, head, upper arms, forearms and hands, upper legs, lower legs, and feet of the dummy. The revolutions of the dummy are represented by spring elements with viscous damps. The dummy weighs 76 kg, and the model has 1745 finite elements.

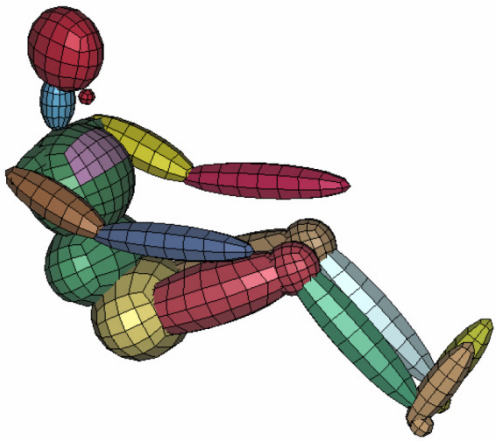

Figure 5.7: GEBOD dummy model

At present, specifically developed and validated human surrogate models suitable for assessing occupant response in a vehicle subject to mine strike are not available. Horst et al. [96] used the standard Hybrid III crash test dummy to study the lower leg injuries occurring in anti-tank mine strikes. Williams et al. [97] studied

crew member responses in a light armored vehicle (LAV) subjected to a mine blast load by using the GEBOD rigid body dummy model incorporated in LS-DYNA. Due to the computational efficiency of this dummy model, a total of six GEBOD dummies were put at different positions in the LAV for the simulation.

In this work, the GEBOD dummy model shown in Fig. 5.7 is employed for blast protection design because of its low computational cost and an acceptable error level.

Vehicle Model

A FE model of a military vehicle is developed in this work, based on rough computer aided design (CAD) data obtained from the internet, as shown in Fig. 5.8.

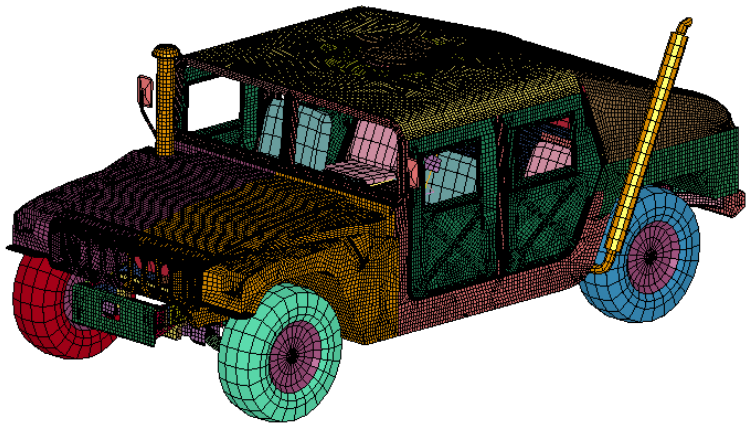

Figure 5.8: Finite element model of a military vehicle

Figure 5.9 is a snapshot of the simulation result of a vehicle under landmine blast attack, using the developed vehicle model coupled with the GEBOD dummy model. The blast load from the landmine is simulated using the CONWEP empirical model in LS-DYNA. The landmine is detonated directly underneath the driver's seat.

As illustrated, the vehicle body adjacent to the landmine has been significantly damaged. The resultant dummy responses can also be predicted. As expected, in this case, the dummy will be seriously damaged if no additional protection is provided. This example demonstrates the capability developed in this work, enabling the simulation of a general mine-vehicle-occupant interaction. It is worth noting that although the vehicle model and the dummy model employed in this work have not been validated through rigorous testing procedures, they are more than sufficient to be utilized to demonstrate the concept and method proposed in this work for blast protection design.

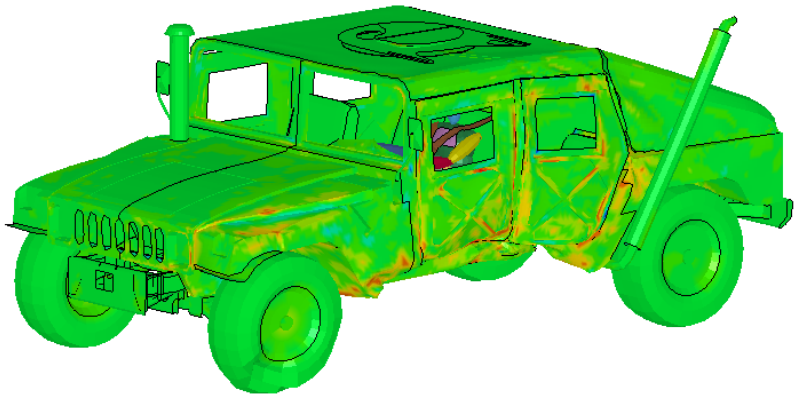

Figure 5.9: Snapshot of a blast simulation result with developed capabilities

5.3 Implementation of Space Decomposition

5.3.1 Vehicle-Level Space Decomposition

To simplify the design process, the *space decomposition* approach is

implemented in the vehicle level to obtain a reduced DOF subsystem model as shown in Fig. 5.10a. Besides the GEBOD dummy, this subsystem model includes driver seat, seat belts, and the underbody armor structure. The blast simulation results from this subsystem model representing the vehicle model, including the deformation of the vehicle (floor and driver seat structure), the energy absorption of the underbody armor structure, and, especially, the responses of the dummy, etc. This is ensured by the target cascading process, and is realized by applying the appropriate boundary conditions and loads to the subsystem model. Figure 5.10b shows a snapshot of a blast simulation result using the reduced DOF subsystem model.

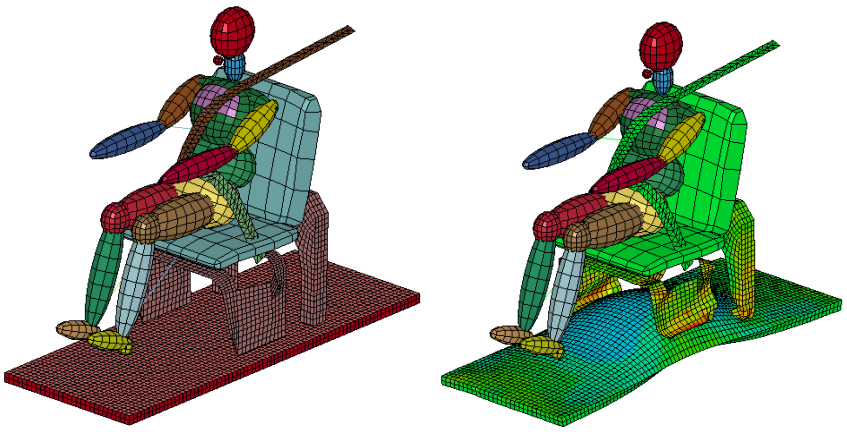

(a) (b)

Figure 5.10: (a) Reduced DOF model for blast protection design; and (b) simulation result.

5.3.2 Subsystem-Level Space Decomposition

Let's consider the detailed mine-vehicle-occupant interaction using the *time (process) decomposition* concept, based on the reduced DOF subsystem model. First, the blast load from the landmine is exerted on the underbody armor structure; part of

the blast energy is dissipated by the armor structure, and the rest of the energy causes vehicle floor acceleration. The acceleration forces directly injure the feet and the lower legs of the occupant. At the same time, the acceleration forces are transmitted to the driver seat through the seat mounts, causing seat deformation and injury to the upper body of the occupant. This whole process takes place in about ten milliseconds. Note that only the effects of forces (momentum) from the landmine blast are considered; other effects including blast overpressure and fragmentation are neglected to simplify the problem.

Designing a blast protection system under such an extreme load is difficult due to the complexity of the process, especially the coupling effects of various subsystems. To simplify the design, the *space decomposition* approach is employed a second time. As shown in Fig. 5.11, the reduced DOF subsystem is decomposed into three sub-subsystems, the driver seat subsystem, the restraint (seat belts) subsystem, and the underbody armor structure subsystem. A simplified analytical model of the reduced DOF subsystem can be employed to assist the corresponding target cascading process. Figure 5.12 demonstrates the target cascading process of the blast protection design problem.

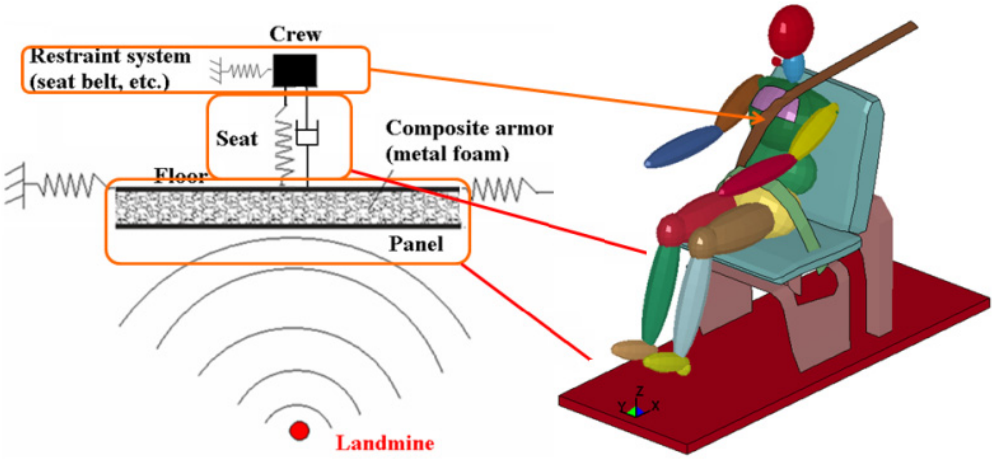

Figure 5.11: Space decomposition of the reduced DOF subsystem

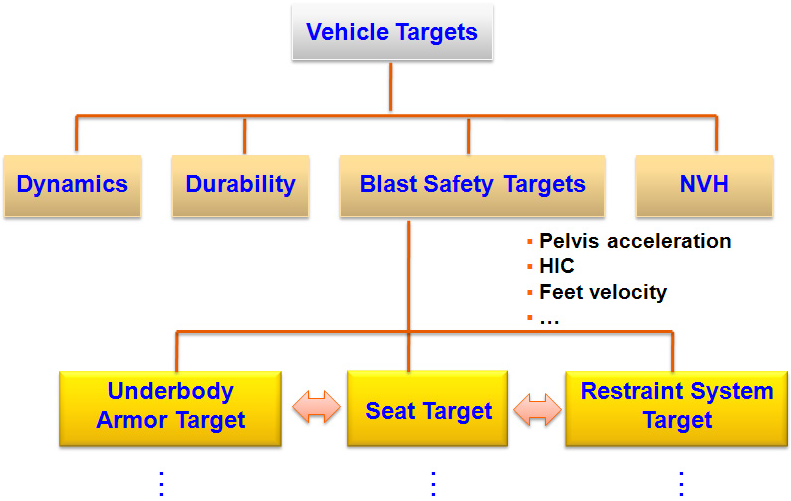

Figure 5.12: Target cascading process in a blast protection design problem

After the design targets for each subsystem are obtained, these subsystems can be designed individually. The original blast protection design problem is greatly simplified in this way. The design of the driver seat subsystem and the effects of the restraint subsystem are briefly discussed in the following sections, while the design of the underbody armor structure will be investigated in more detail later.

5.4 Effects of Seat Design

The design goal for the driver seat subsystem is to mitigate the level of force that is transmitted to the occupant's upper body, when the input is the acceleration force from the blast transmitted to the seat mounts on the vehicle floor. An ideally designed seat should be one that can adjust to the optimal mechanical properties according to various acceleration force levels, so as to reduce the force transmitted to the upper body of the occupant.

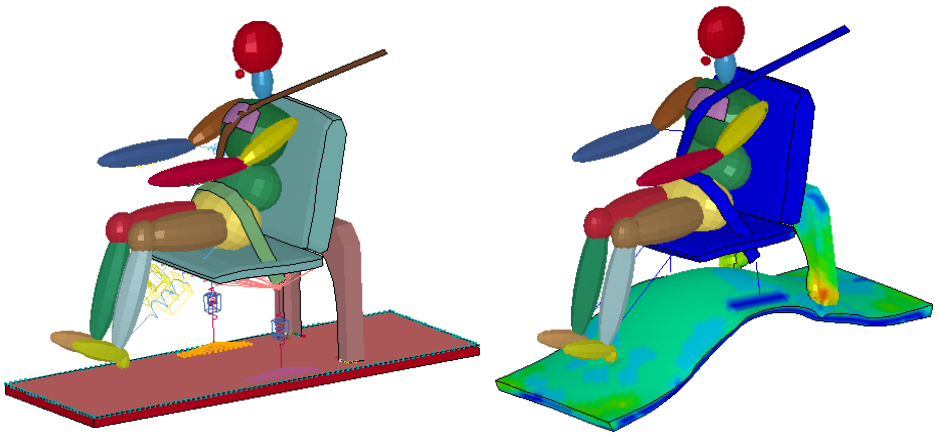

(a) (b)

Figure 5.13: (a) A simplified driver seat model; and (b) simulation result.

For a demonstration of the effects of seat design changes on occupant responses under a blast load, a simplified driver seat model is built as shown in Fig. 5.13a. Figure 5.13b shows a snapshot of a blast simulation result using the simplified driver seat model. In this model, one dimensional non-linear springs and dampers are employed to represent the driver seat structure, linking the seat pad to the vehicle floor. Three designs with different spring stiffness are evaluated with a focus on the responses of the occupant. Figure 5.14 compares the occupant responses in the three

different designs; it is seen that the driver seat properties have great influence on occupant responses under a blast load. A properly designed driver seat can mitigate occupant injuries by reducing the resultant acceleration levels of the pelvis and the head of the occupant, as shown in Fig. 5.14a and Fig. 5.14b, respectively. It is also seen that seat properties have little effect on the occupant lower body responses such as the feet velocities, as shown in Fig. 5.14c.

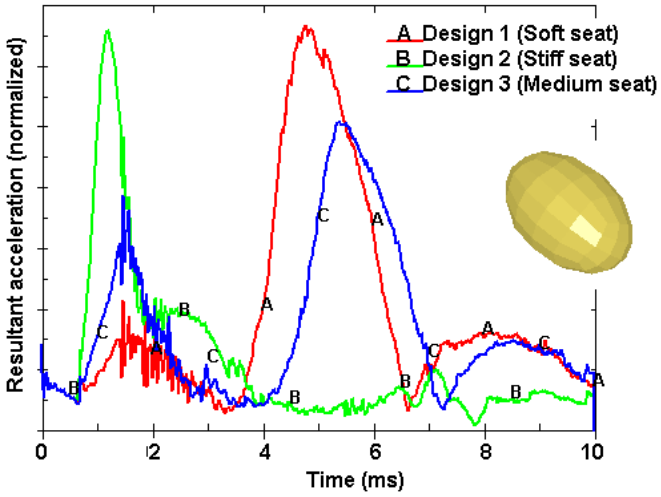

(a)

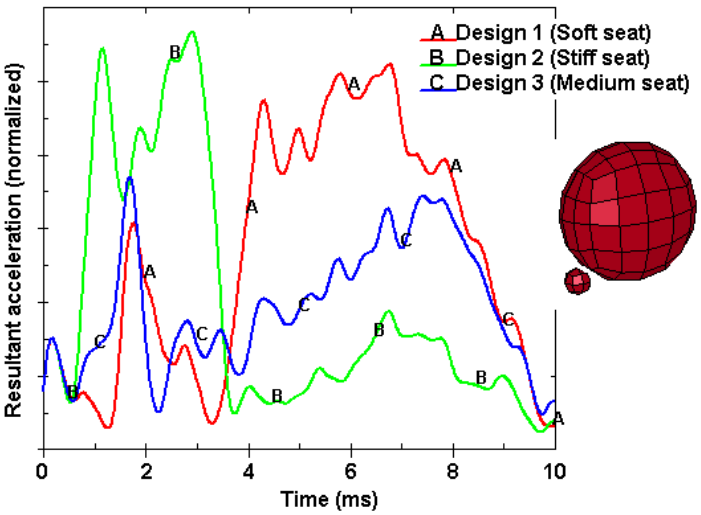

(b)

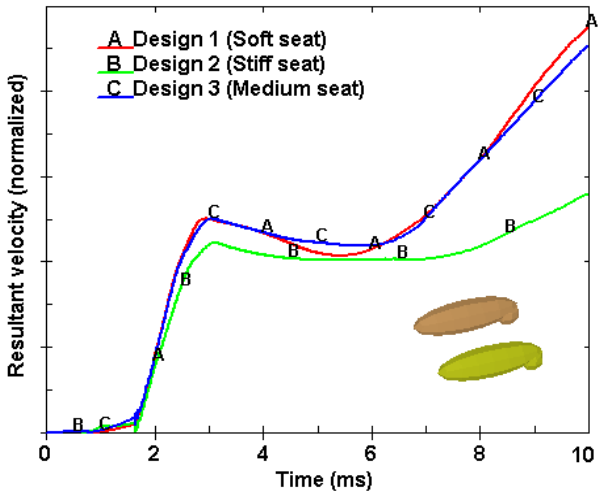

(c)

Figure 5.14: Occupant responses with driver seat design variations under a blast load: (a) head acceleration; (b) pelvis acceleration; and (c) feet velocity.

Design optimization can be conducted to obtain the optimal properties of the non-linear springs and viscous dampers in the simplified driver seat model. These optimal properties can be then set as design targets for detailed seat structures. Advanced topology optimization techniques may be applied to the design of these seat structures. This can be viewed as a target cascading process.

5.5 Effects of Restraint System

Two simulations are conducted to show the effects of a restraint system (seat belts) on occupant responses under a blast load. Figure 5.15 shows occupant kinematics under a blast load with (Fig. 5.15b) and without (Fig. 5.15a) seat belts being worn. It is seen that without seat belts, the occupant is ejected from the seat and hits the A pillar under a blast load, implying much greater injuries than in the case when seat belts are properly worn; in this latter case, the occupant is constrained to the seat by the seat belts, implying a much lower chance of severe injury. Figure

5.16 further compares the whole-body kinetic energy of the occupant in the two cases, with the case of seat belts being worn showing a much lower kinetic energy level. It is concluded from this example that the restraint subsystem (seat belts) is critical for occupant injury mitigation under a blast load, and therefore, needs to be considered in a blast protection design.

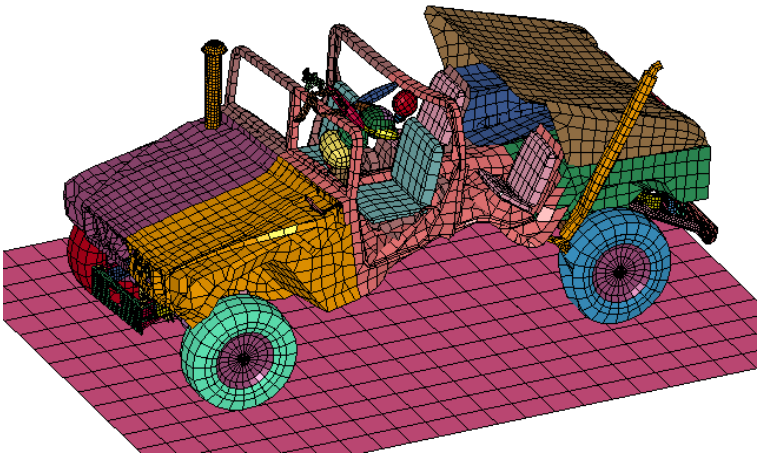

(a)

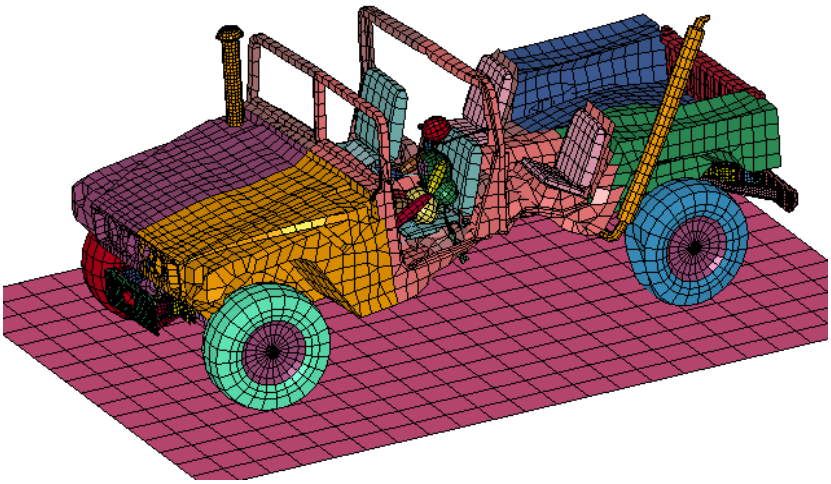

(b)

Figure 5.15: Occupant responses (a) without, and (b) with seat belts being worn, under a blast load

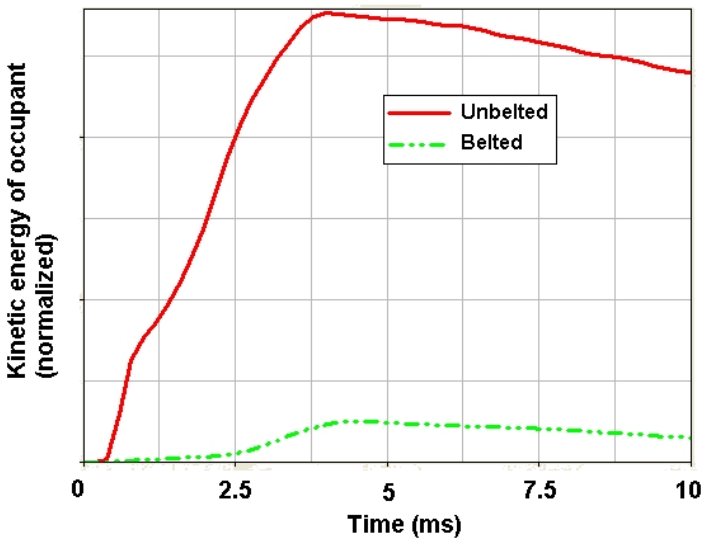

Figure 5.16: Reduced occupant injuries with seat belts worn

5.6 Underbody Armor Structure Design with Uncertainties

The objective of underbody armor structure design is to minimize the blast load transmitted to the vehicle floor, especially at the location of the seat mounts. Because of the nature of armed conflict, military vehicles are subjected to attacks by landmines whose location and TNT equivalent are never accurately anticipated. Considering these uncertainties in armor structure design is necessary, because various blast locations and varying TNT equivalents will result in a variety of crew responses and injury levels. From a design point of view, these uncertainties should be considered in order to achieve a reliable design. For the underbody armor structure design, two design concepts are proposed to account for the landmine location uncertainties: design for worst case (DWC), and equal protection design (EPD).

5.6.1 Metal Foam Material Model

Aluminum foam is a lightweight material with excellent plastic energy absorbing characteristics. In compression, aluminum foam behaves very much like a perfect-plastic material, making it attractive for use in a sacrificial layer for blast protection. The density of aluminum foam can be specified in the range from 0.1 to 0.5 g/cm^3. A general characteristic is that most foam properties are functions of the foam's density. This means that the collapse load for blast-protective sacrificial layers made of aluminum foam is easily specified by selection of the proper foam density. A general relationship relating the plateau stress of foams to their density, ρ_f, has been proposed by Ashby et al. [49] as

$$\frac{\sigma_f}{\sigma_{f0}} = K\left(\frac{\rho_f}{\rho_{f0}}\right)^n \tag{5.12}$$

where the subscript f and f0 refer to foam and dense solid, respectively; K and n are constants (at fixed strain rate); K usually ranges from 0.25 to 0.35, and n ranges between 1.5 and 2.0. Test data shows that there is no clear dependence between plateau stress and strain rate for aluminum foams [98].

Table 5.2: Material card used in LS-DYNA for aluminum foam (Units = cm, g, microsecond)

*MAT_HONEYCOMB							
RO	E	PR	SIGY	VF	MU	BULK	AOPT
0.34	0.7	0.33	0.00322	0.126	0.05	0	0
EAAU	EBBU	ECCU	GABU	GBCU	GCAU		
0.02	0.02	0.02	0.02	0.02	0.02		
*DEFINE_CURVE (STRESS VS. STRAIN) (STRAIN) 0.00E+00 4.00E-03 8.10E-01 8.14E-01 (STRESS) 0.00E+00 8.00E-05 8.00E-05 1.60E-04							
*DEFINE_CURVE (SHEAR STRESS VS. VOLUME STRAIN) (STRAIN) 0.00E+00 4.00E-03 8.10E-01 8.14E-01 (STRESS) 0.00E+00 8.00E-05 8.00E-05 1.60E-04							

The MAT_HONEYCOMB material card in LS-DYNA is employed to model the aluminum foam material for the underbody armor structure design. This material card allows one to use experimentally measured load curves in compression and shear. It neglects the elastic deformation and is sufficient for the computation of energy and displacement. The material parameters and the load curves for the aluminum foam used in this work are summarized in Table 5.2. In addition to load curves, this model requires the elastic-plastic properties of fully compacted materials, and in the present case, the properties of aluminum are used.

5.6.2 Landmine Location Uncertainties

Suppose a landmine is detonated directly under a military vehicle's left floor span at an unanticipated location. Figure 5.17 shows the sampling of blast locations. Considering the maximum value of the kinetic energy the crew experiences during the blast process to be the injury criteria, a response surface is constructed with

respect to landmine locations based on the data at the sampling locations, using the Kriging method, as shown in Fig. 5.18. It can be seen that a blast right under the driver seat (Case 8) gives the maximum value of response. The scenario is then identified as the worst case for underbody armor structure design.

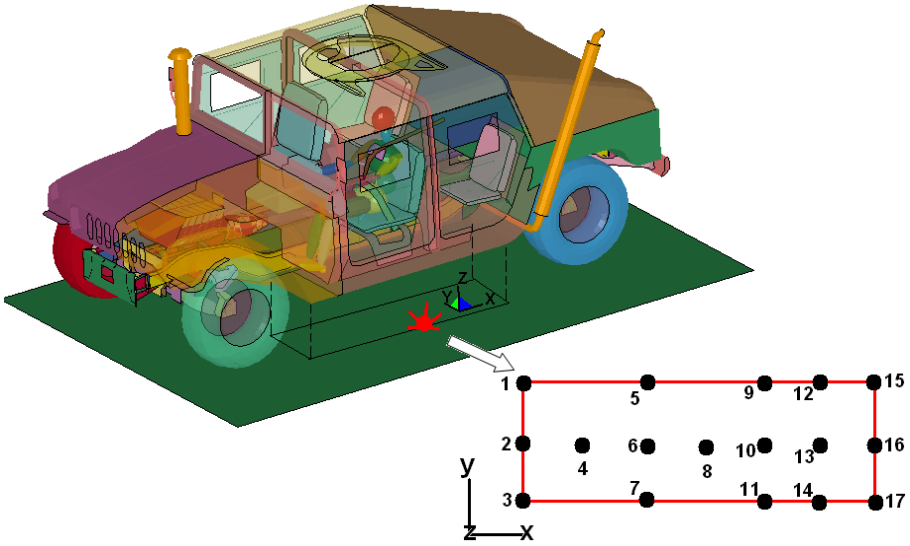

Figure 5.17: Illustration of landmine location uncertainties

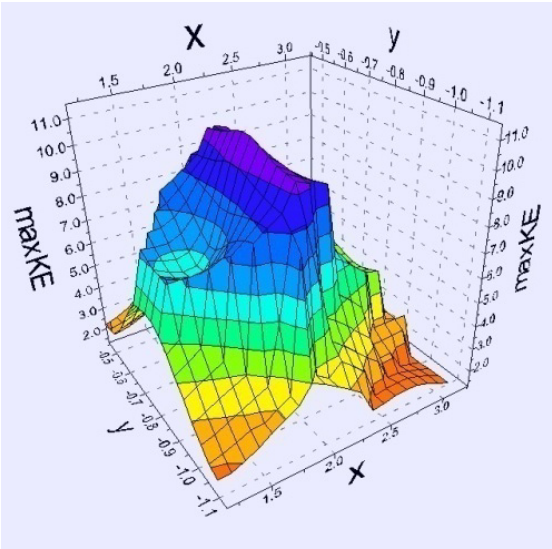

Figure 5.18: Response surface of maximum kinetic energy of crew with respect to landmine locations

5.6.3 Design for Worst Case

Once the worst case (Case 8) is identified using the response surface method, the design for the worst case is a straightforward concept to implement. Figure 5.19 shows the position where the aluminum foam armor structure is attached to the vehicle floor. The design variable in the current study is the thickness of the aluminum foam layer as shown in Fig. 5.20; a stiffened aluminum panel is attached to the aluminum foam layer to deflect the blast wave, as well as to prevent fragments from shooting into the occupant compartment. The relationship between the maximum kinetic energy of the crew and the thickness of the aluminum foam layer for Case 8 is identified as shown in Fig. 5.21. With the proposed design target shown in Fig. 6.25, a minimum foam layer thickness of 10 cm is determined to meet the design target. One obvious drawback of the DWC concept is that its conservative property always results in unnecessary weight being added at the less critical locations of the designed foam armor structure.

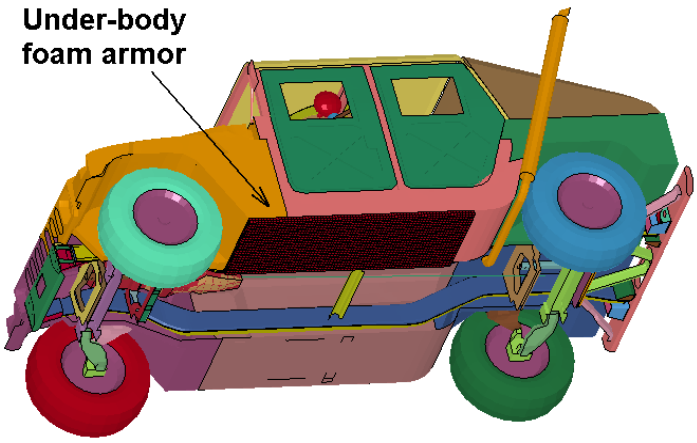

Figure 5.19: Aluminum foam armor structure is attached to the vehicle floor

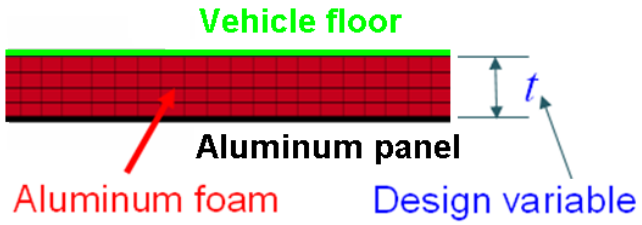

Figure 5.20: Design variable of the aluminum foam armor structure

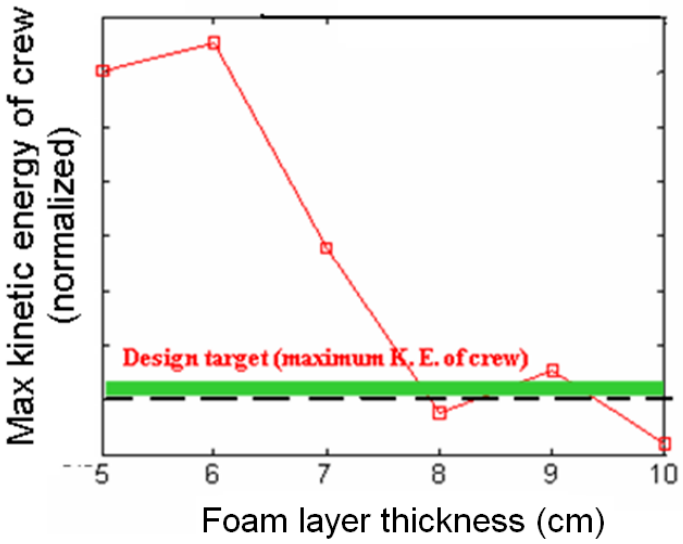

Figure 5.21: Maximum crew member kinetic energy vs. foam thickness (case 8)

5.6.4 Equal Protection Design

The equal protection design (EPD) concept for the aluminum foam armor profile design provides equal protection for crew members subjected to landmine blast originating at any possible location. With the EPD concept, more material is positioned in the critical locations where potential crew injury level is high, while less material is used at locations farther from the crew. The advantage of using EPD is the potential weight savings of the armor structure, which is a high priority for military vehicle applications.

Space Decomposition of the Foam Armor Panel

The first step of the EPD process is to develop an analytical model to predict the deformation contour of the sandwich aluminum foam panel subjected to a blast load. The analytical model can afterward be used for design purposes. *Space decomposition* is employed here at the component level, as shown in Fig. 5.22; the armor foam panel is decomposed into a number of evenly-divided foam bars. The blast pressure load on each foam bar can be determined from the relative position of the bar compared to the explosive charge. For the *i*th bar in row, load pressure $p_i(t)$ can be obtained as

$$p_i(t) = p(t)\cos\theta_i \tag{5.13}$$

where $p(t)$ is the blast load pressure at the proximal end the specific foam bar, which is a function of the weight of the explosive, W and the distance from the center of the explosion, R.

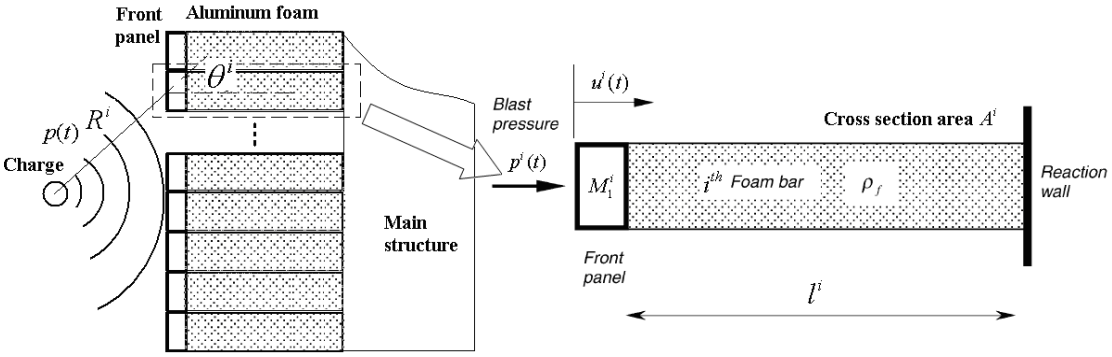

Figure 5.22: Space decomposition of a foam panel into foam bars

With *space decomposition*, the original structural design problem is transformed into a series of simplified design problems; each has a single design variable, namely

the length of the foam bar, as shown in Fig. 5.22. By solving the foam bar crushing problem caused by the cascaded blast load, an analytical solution for each foam bar deformation under the blast load can be obtained. Then, using a so-called "inverse thickness design" (ITD) method in the next section, the optimal profile of the sandwich panel can be determined. The resulting design will be validated in the later parts of this section.

Analytical Model for Design

The analytical solution has been developed by Hanssen et al. [59] to describe the deformation behavior of an aluminum foam bar subjected to a linearly decaying blast load. As shown in Fig. 5.22, the foam bar is covered by a front panel with mass M_1 and cross-sectional area of A. The compressive blast loading $p(t)$ acts directly on the front plate. Here, $p(t)$ does not take into account spatial distributions, i.e. $p(t)$ is not reduced as the front plate moves away from the blast-loading source. The foam bar itself has length l, cross-sectional area A, and total mass $M_0 = \rho_f Al$. The foam density is denoted by ρ_f whereas the density of the solid-base material of the foam is ρ_{f0} (as it would be for fully compacted and densified foam). The front panel is considered to be rigid, whereas the foam material has a plateau-stress level of σ_0. At an engineering-strain level of ε_D, the foam locks into a rigid solid as shown in Fig. 5.23. The foam bar is fixed to a rigid wall at the end furthest away from the blast loading (the distal end). The displacement of the front panel, and thus the deformation of the foam bar, is given by $u(t)$.

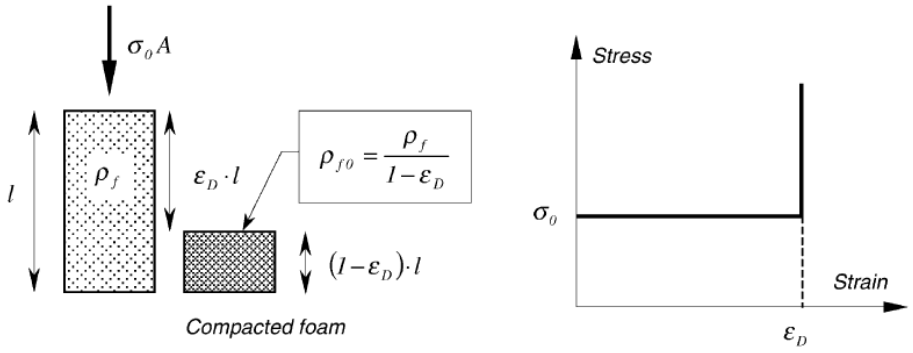

Figure 5.23: Material characteristics of the foam bar [59]

One differential equation can be derived by making the momentum change of the complete foam bar equal to the impulse exerted by the blast loading and the reaction wall force; that equation reads

$$\left[1+\frac{\rho_f A}{M_1 \varepsilon_D}u\right]\ddot{u}+\frac{\rho_f A}{M_1 \varepsilon_D}\dot{u}^2+\left(\sigma_0 - p(t)\right)\frac{A}{M_1}=0 \tag{5.14}$$

The blast loading pressure $p(t)$ is assumed to have a triangular shape and is defined by

$$p(t)=\begin{cases} p_0\left(1-\dfrac{t}{t_0}\right), & t \le t_0 \\ 0, & t > t_0 \end{cases} \tag{5.15}$$

Here, p_0 is the initial peak overpressure, whereas t_0 is the duration of the blast loading. The initial conditions of the system are $u(0)=0$ and $\dot{u}(0)=0$. The complete solution to the problem is given by

$$\frac{u}{\varepsilon_D l}=0, \quad t \le 0 \text{ or } \frac{p_0}{\sigma_0} \le 1 \quad ,$$

$$\frac{u}{\varepsilon_D l} = -m + \sqrt{m^2 + 4\xi\left\{\left(1-\frac{\sigma_0}{p_0}\right)\left[\frac{t}{t_0}\right]^2 - \frac{1}{3}\left[\frac{t}{t_0}\right]^3\right\}}, \quad 0 < t \le t_0 \text{ and } \frac{p_0}{\sigma_0} > 1,$$

$$\frac{u}{\varepsilon_D l} = -m + \sqrt{m^2 + 4\xi\left\{-\frac{1}{3} + \left[\frac{t}{t_0}\right] - \frac{\sigma_0}{p_0}\left[\frac{t}{t_0}\right]^2\right\}}, \quad t_0 < t \le \frac{1}{2}\frac{p_0}{\sigma_0}t_0 \text{ and } \frac{p_0}{\sigma_0} > 2,$$

$$\frac{u}{\varepsilon_D l} = -m + \sqrt{m^2 + \xi\left\{\frac{p_0}{\sigma_0} - \frac{4}{3}\right\}}, \quad t > \frac{1}{2}\frac{p_0}{\sigma_0}t_0 \text{ and } \frac{p_0}{\sigma_0} > 2. \tag{5.16}$$

where $m = \dfrac{M_1}{M_0}$ is the mass ratio between the front panel and the foam bar; $\xi = \dfrac{I^2}{M_0 P_0 \varepsilon_D l}$ is the impact factor with I the total impulse exerted on the front panel by the blast loading, $I = \dfrac{1}{2}p_0 t_0 A$, and where P_0 is the initial blast-loading force $P_0 = p_0 A$.

From the above solution, if $p_0 < \sigma_0$, no deformation of the foam bar will take place at all; if $p_0 > \sigma_0$, then it is seen that the deformation of the foam bar will reach its maximum and stop during blast loading ($t < t_0$) if $1 \le \dfrac{p_0}{\sigma_0} \le 2$.

Furthermore, the solution states that after the end of the blast loading, the deformation of the foam will reach its maximum value at time t_m given by $\dfrac{t_m}{t_0} = \dfrac{1}{2}\dfrac{p_0}{\sigma_0}, \ \dfrac{p_0}{\sigma_0} > 2.$

The cross-sections of deformed aluminum foam bar specimens under different blast pressures are shown in Fig. 5.24.

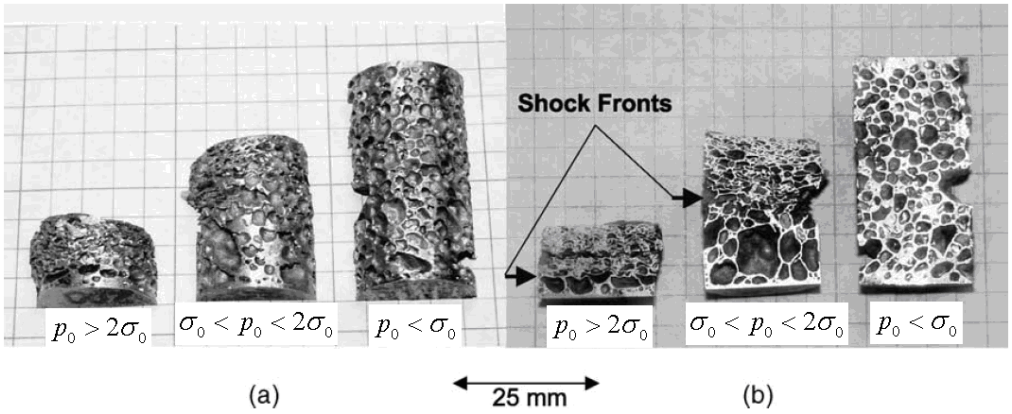

Figure 5.24: Deformations of aluminum foam bar specimens under different blast pressures: (a) surfaces; (b) sections.

An example problem is solved using the analytical solution developed above, as well as by using LS-DYNA simulation. The purpose is to understand the relative accuracy of both the analytical and numerical solutions so that the designed armor structure (based on the analytical solution) can be used in the LS-DYNA simulation for the purpose of validation based on a full vehicle model. Figure 5.26 shows that the difference is significantly large when a very rough mesh (i.e., mesh level 1 in Fig. 5.25) is used in LS-DYNA simulation, but it decreases when a finer mesh is used, with convergence to the analytical solution taking place when the mesh is further refined. As shown in Fig. 5.26, the difference becomes negligible when mesh level 4 is used. This validates the analytical solution and its usefulness for the design process.

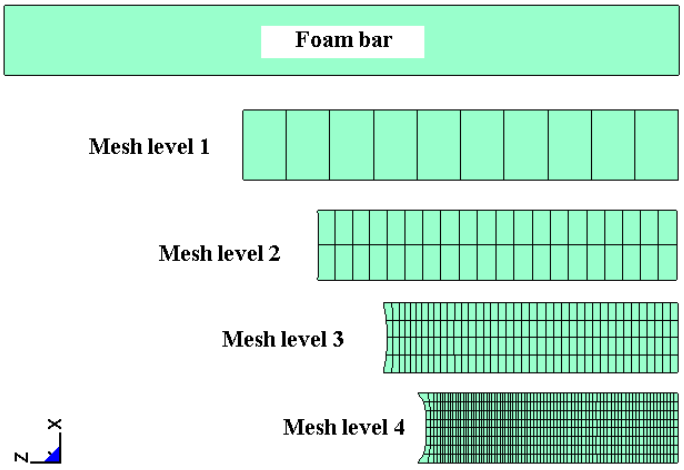

Figure 5.25: Deformed shape of foam bar with various mesh size levels

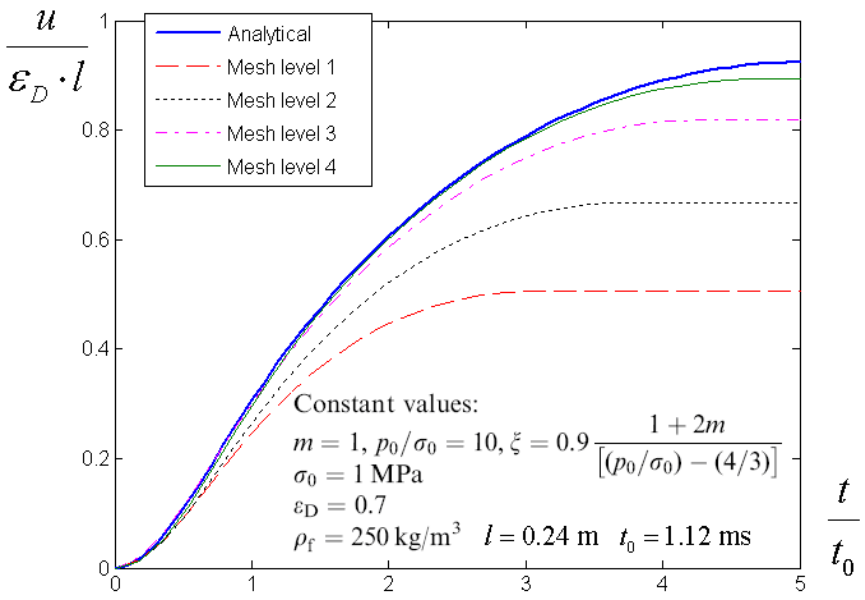

(a)

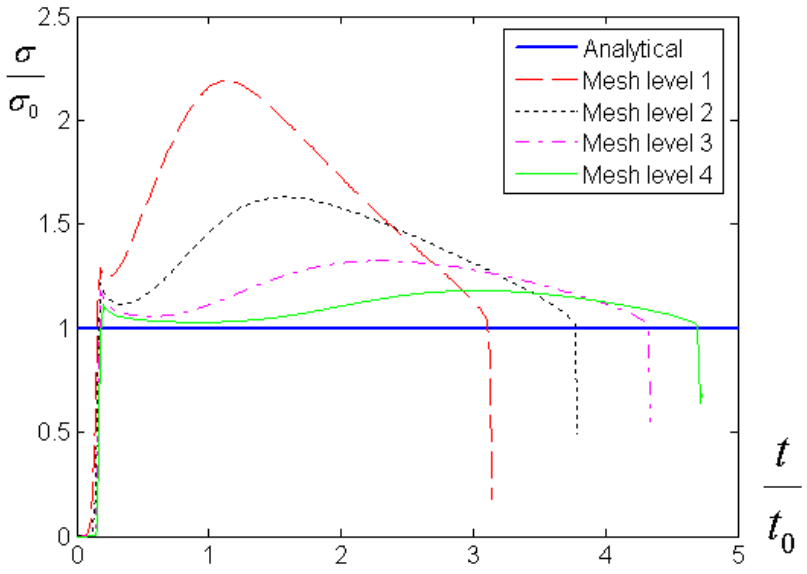

(b)

Figure 5.26: Comparison of the analytical solution and LS-DYNA results of foam bar under blast load: (a) displacement u of foam bar; and (b) pressure σ on the end of the foam bar.

The time duration of the blast loading t_0 compared to the time the pressure σ_0 acts on the reaction wall t_m is illustrated in Fig. 5.27. Hence, the impulse transferred to the reaction wall is $\sigma_0 A t_m = \frac{1}{2} p_0 A t_0$, which shows that the impulse exerted by the blast loading on the front panel equals the impulse exerted by the foam bar on the reaction wall, i.e. momentum is conserved.

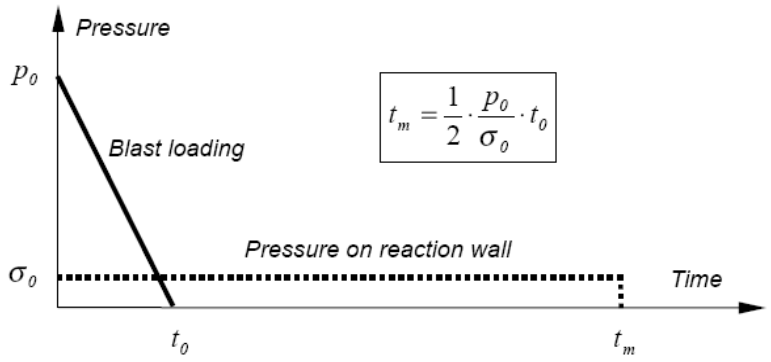

Figure 5.27: Pressure on front panel vs. pressure on reaction wall [59]

The maximum deformation in the foam is determined by the lock-in strain ε_D, hence

$$0 \le \frac{u}{\varepsilon_D l} \le 1 \tag{5.17}$$

Using Eq. (5.16), this can be recast into the following condition between the two dimensionless numbers m and ξ

$$0 \le \xi \le \frac{1+2m}{\left[\dfrac{p_0}{\sigma_0} - \dfrac{4}{3}\right]}, \quad \frac{p_0}{\sigma_0} > 2. \tag{5.18}$$

Therefore, the minimum length l of the foam bar in order to fully absorb the blast loading is

$$l \ge \frac{I^2}{(M_0 + 2M_1) p_0 A \varepsilon_D} \left\{ \frac{p_0}{\sigma_0} - \frac{4}{3} \right\}, \quad \frac{p_0}{\sigma_0} > 2. \tag{5.19}$$

When an equal sign is applied, the minimum length l^i of the i^{th} foam bar to fully absorb the blast loading is obtained as

$$l^i = \sqrt{\left(\frac{M_1^i}{A^i \rho_{\mathrm{f}}} \right)^2 + \frac{p_0^i (t_0^i)^2}{4 \rho_{\mathrm{f}} \varepsilon_D} \left\{ \frac{p_0^i}{\sigma_0} - \frac{4}{3} \right\}} - \frac{M_1^i}{A^i \rho_{\mathrm{f}}}, \quad \frac{p_0^i}{\sigma_0} > 2. \tag{5.20}$$

where M_1^i is the front panel mass attached to the ith foam bar, if the armor plate is evenly decomposed by N foam bar with front panel mass, then $M_1^i = M_1 / N$ with M_1 the total mass of the front panel; A^i is the cross sectional area of the ith foam bar and $A^i = A/N$ with A the total area of the armor plate. p_0^i is the initial peak of the blast pressure and t_0^i is the total load duration of free-field blast loading at the ith foam bar; both are functions of the distance R^i from the center of the explosion,

the weight of explosive W, and pressure angle θ^i. Equation (5.3) shows that p_0^i is linearly proportion to W and inversely proportion to $(R^i)^3$.

If the minimum value of the foam bar is not met, the foam bar will be completely compacted before the blast loading has fully attenuated. In this case, the rest of the blast loading will be fed directly into the protected structure and a force enhancement phenomenon happens, one that will result in more serious damage to the protected structure than that without the foam bar. This unexpected phenomenon will be investigated thoroughly in the next chapter.

Aluminum Armor Profile Design

After the analytical model has been validated, a design method called inverse thickness design (ITD) is developed based on the *space decomposition* described above, in order to achieve the equal protection design (EPD). As illustrated in Fig. 5.28, the optimal profile is determined using the ITD method based on the predicted deformation of the sandwich panel and the trial thickness, t_{trial}, and the given minimal thickness, $t_{\mathbf{minimal}}$, of the foam layer. With this design method, the smallest needed amount of the foam material can be calculated with superior computational efficiency, so that it can be extended far enough to take into consideration the blast load uncertainties in a real design problem. A Matlab code called Foam Design Kit (FDK) has been developed to predict the deformation of the foam layer under certain blast loads as shown in Fig. 5.29a, as well as to obtain the optimal profile as shown in Fig. 5.29b (for a two-dimensional design). The designed foam layer compressed

evenly under the same blast load as that shown in Fig. 5.29c, provides equal protection along the foam, yet with reduced material usage. Figure 5.30 further illustrates a three dimensional example with the deformed shapes of the foam layer predicted by different models to validate the FDK developed. Two LS-DYNA models have been developed: a discrete model with decomposed foam bars separated from each other, exactly like what was used in the foam design kit; and a continuous model with a foam layer without decomposition. It is seen that the FDK is capable of predicting the results of the discrete LS-DYNA model and yielding more deformation than the continuous model, as shown in Fig. 5.30c. This is understandable, since the bending stiffness of the foam layer is not included in the discrete model. After validation, the FDK can be employed in the following proposed design process.

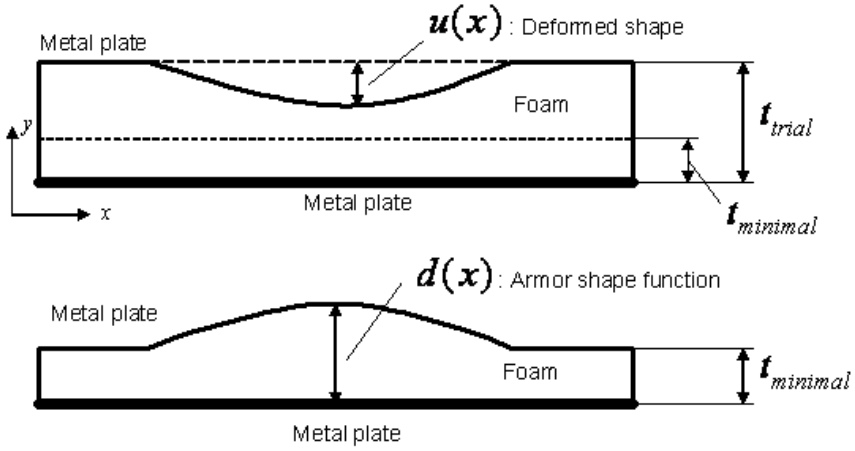

Figure 5.28: ITD method for EPD

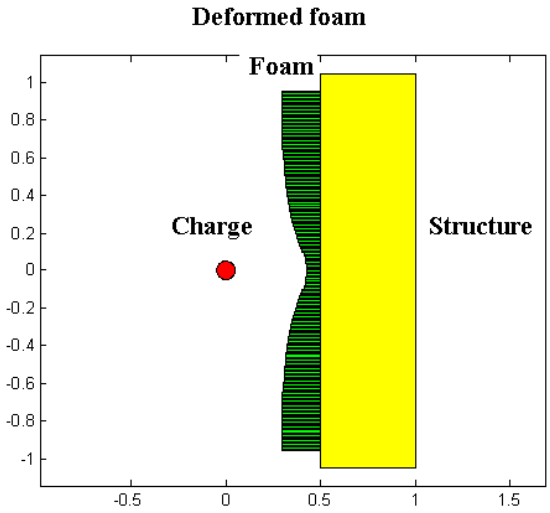

(a)

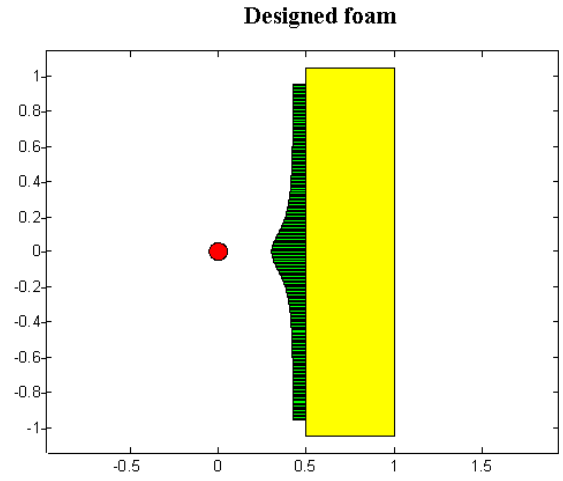

(b)

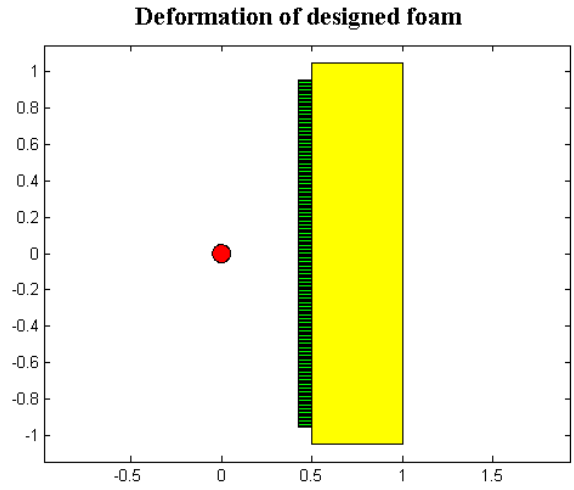

(c)

Figure 5.29: Two-dimensional foam layer profile design example: (a) deformed shape; (b) designed profile; and (c) deformation of designed foam layer.

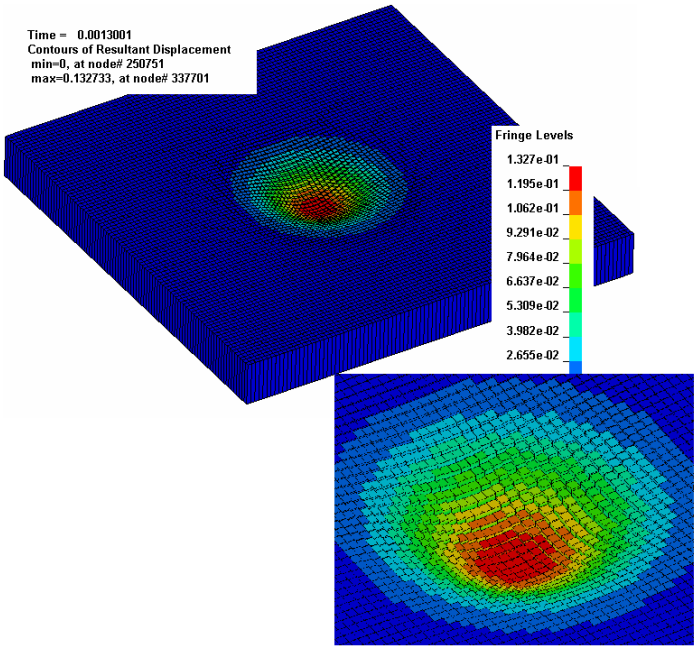
Time = 0.0013001
Contours of Resultant Displacement
min=0, at node# 250751
max=0.132733, at node# 337701
Fringe Levels
1.327e-01
1.195e-01
1.062e-01
9.291e-02
7.964e-02
6.637e-02
5.309e-02
3.982e-02
2.655e-02

(a)

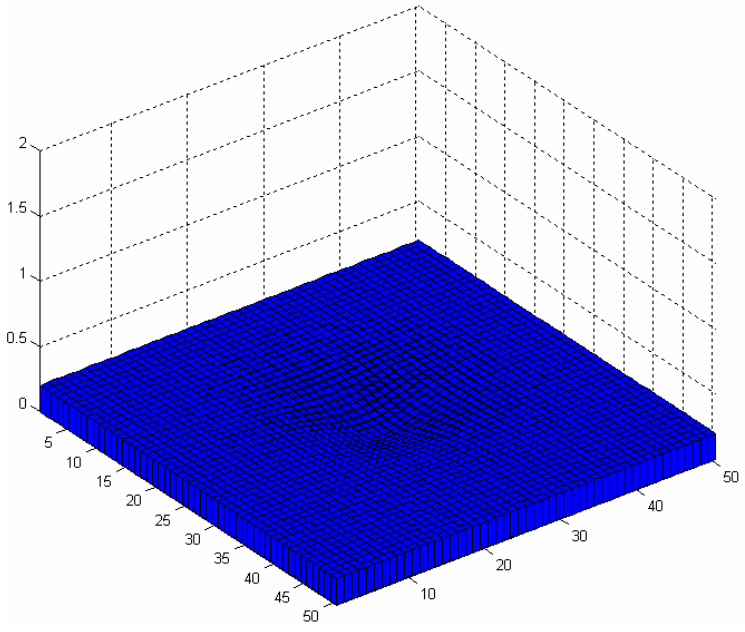
2
1.5
1
0.5
0
5
10
15
20
25
30
35
40
45
50
10
20
30
40
50

(b)

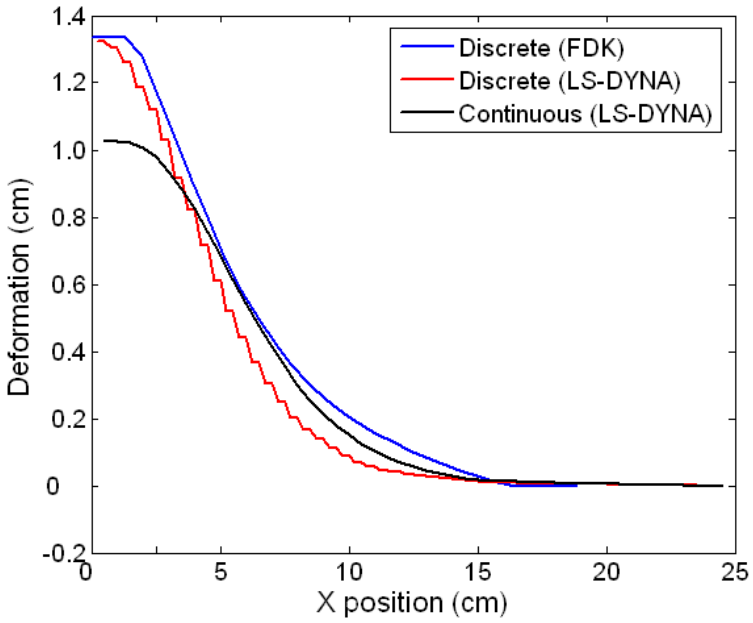

(c)

Figure 5.30: Comparison of three-dimensional foam layer deformations predicted by different models: (a) deformation predicted by LS-DYNA; (b) deformation predicted by FDK; and (c) comparison of foam layer deformation predicted with different models.

Equal Protection Design with Uncertainties

Again, consider the aluminum foam armor profile design problem with landmine location uncertainty; for simplification, only three representative locations are considered, as shown in Fig. 5.31. For the specified design target, i.e., the maximum allowable kinetic energy of the crew, the minimum foam layer thickness for blast location "x" (Case 8) can be determined to be 10 cm as illustrated in Fig. 5.21; and for locations "1" and "2", the minimum foam layer thickness are determined to be 7 cm and 8 cm, respectively. After applying the ITD method using the FDK, the two-dimensional profile of the foam layer for each individual location is obtained; the profile of the final design is created by combining the three single profiles smoothly, as illustrated in Fig. 5.32a. Figure 5.32b shows the three-

dimensional shape of the final designed foam armor with varying thicknesses. It is obvious that with more locations addressed, the shape of the designed foam armor will be more precise, providing equal protection for the crew member regardless the location of the landmine. After attaching the designed foam armor to the floor of the vehicle, simulation results show that with the designed foam armor taking into consideration the landmine location uncertainty, the crew responses fall within the design target at all three locations, as shown in Fig. 5.33. This design process can be easily extended to enable consideration of many arbitrarily selected possible blast locations. Table 6.3 further gives information about the mass increase ratio that takes place with the various designs, noting that all of the designs will provide the same crew protection capability. Compared to the metal armor, the aluminum foam armor adds much less mass to the baseline vehicle mass, and the proposed design approach can further reduce the armor mass by one-half.

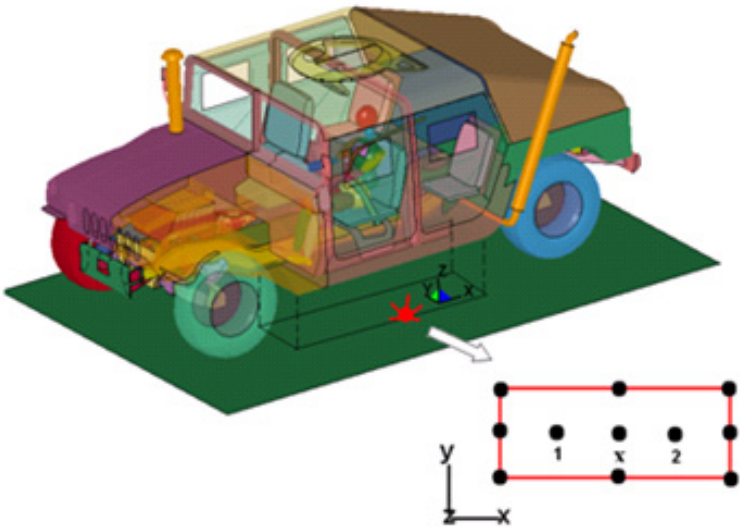

Figure 5.31: Illustration of possible landmine blast locations

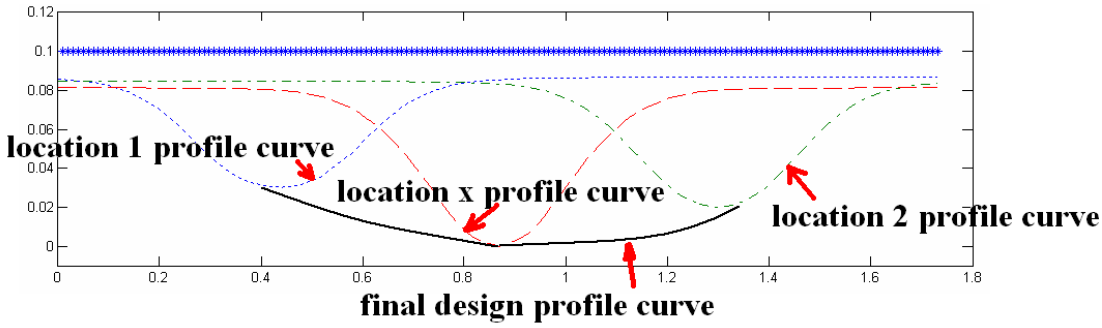

(a)

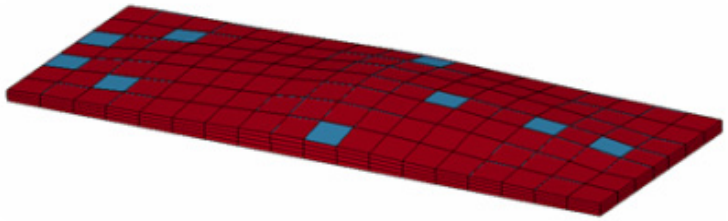

(b)

Figure 5.32: Designed aluminum foam armor with uncertainties: (a) 2-D profile; and (b) 3-D shape.

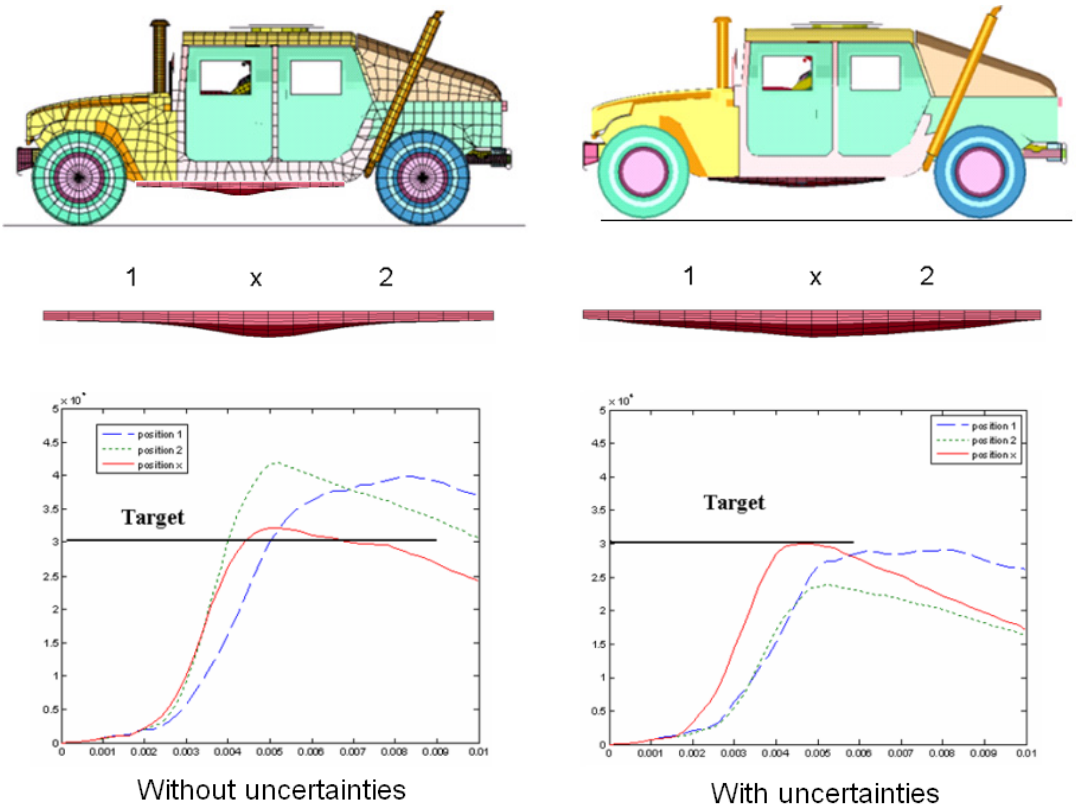

(a) (b)

Figure 5.33: Design results (a) without, and (b) with uncertainties.

Table 5.3: Comparison of weights with different armors

Systems	(Added) mass (kg)	(Added) mass ratio (%)
Vehicle	3,397	100
Steel armor	1,797	53
Uniform aluminum foam armor	116	3.4
Designed aluminum foam armor	66	1.9

In this example design problem, approaches related the following layers of the magic cube have been employed: *space decomposition, target cascading, optimization technique, loading*, and *uncertainties*. The employed approaches can be represented by four elements of the magic cube as shown in Fig. 5.34.

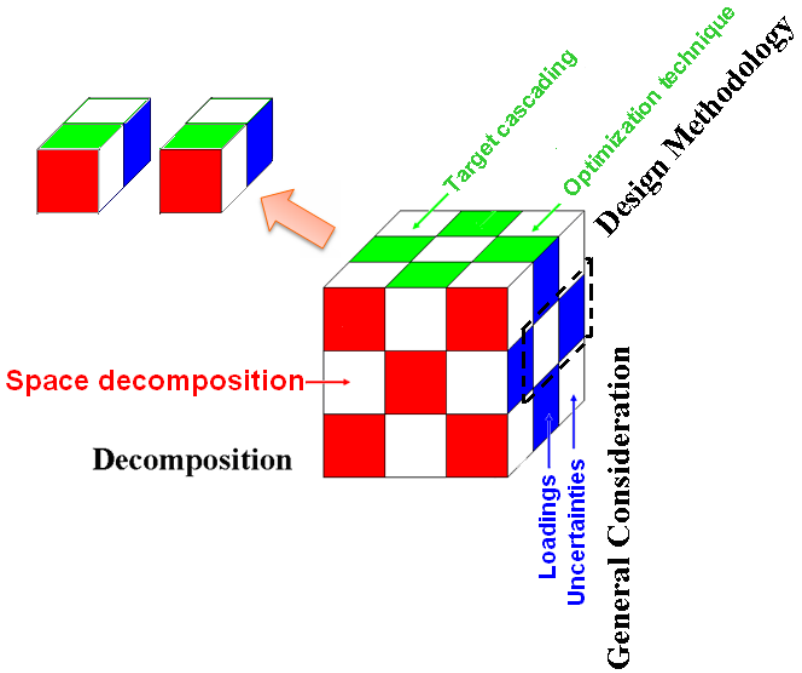

Figure 5.34: Elements of the magic cube for the blast protection design problem

5.7 Conclusions

In this chapter, the MQ approach has been successfully employed to assist in a complicated blast protection design process of a military vehicle system. The *space decomposition* in the MQ approach has been employed to decompose the complicated blast protection system into three subsystems, which are driver seat, restraint system (seat belts), and underbody armor structure. Simulation results show that driver seat properties have great influence on occupant responses under a blast load; simulation results also show that the restraint subsystem (seat belts) is critical for occupant injury mitigation during a blast load. Two design concepts, DWC and EPD, have been proposed for the design of the underbody armor structure. Examples have demonstrated the effectiveness of these concepts for the underbody armor structure design for weight reduction purpose, with consideration of loading uncertainties.

CHAPTER VI

Force Enhancement Phenomenon with Cellular Material

This chapter is dedicated to investigate the root cause of the force enhancement phenomenon when using a cellular material, such as aluminum foam, for blast protection, and to seek countermeasures to prevent this undesired phenomenon from happening. This chapter is organized as follows: first, two cellular material models with microscopic features are proposed and utilized to demonstrate the force enhancement phenomenon, through LS-DYNA simulations. Second, a one-dimensional analytical model, which was previously proposed in reference [62], is employed to seek the root cause of the force enhancement effect of cellular materials subjected to blast loads. A panel-foam-structure model is then introduced to seek countermeasures to eliminate force enhancement. Finally, an interim isolating (I-I) structure is introduced to eliminate force enhancement in real blast protection applications, and design strategies are discussed using an example blast protection design problem.

6.1 Understanding Root Cause of Force Enhancement

6.1.1 Three-dimensional Cellular Material Models with Microscopic Features

Let's first show the force enhancement phenomenon through FE simulations. In the LS-DYNA system, cellular materials are generally modeled as solid elements; material properties are represented through material models, such as MAT26, MAT57, MAT63, MAT75, MAT126, etc., by assigning appropriate parameters and loading curves in the material cards. In these models, the microstructure of a specific cellular material is neglected and only the macroscopic properties are taken into consideration. Considering the fact that using cellular materials for blast protection is still an immature research field [49], the need to design the microstructure of a cellular material in order to achieve specific macroscopic properties for blast protection application is far from critical. Once this does become critical, the *scale decomposition* from the MQ approach is ready to be employed to assist in the design process. By way of preliminary work, two cellular material models with microscopic features have been developed. At this time, these two models are employed only to show the force enhancement phenomenon.

Homogenized Model

A homogenized cellular material model uses piecewise linear material for the solid phase of the cellular material, while "holes" are evenly distributed throughout the material domain, as shown in Fig.6.1. The properties of the cellular material are achieved by tuning the material parameters of the solid phase material. Internal

contacts are defined for the solid phase material. Under a blast load, the solid phase materials are accelerated, while the "holes" provide space for material travel. When fully compacted, momentum transfer takes place between the solid phase material and the structure to which the cellular material is attached. This momentum transfer occurs within very short period of time, resulting in force enhancement as shown in Fig. 6.2.

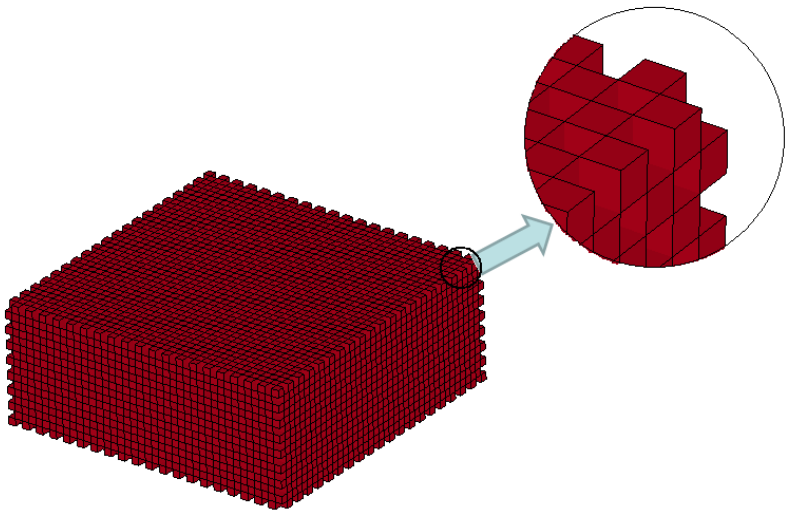

Figure 6.1: Homogenized cellular material model

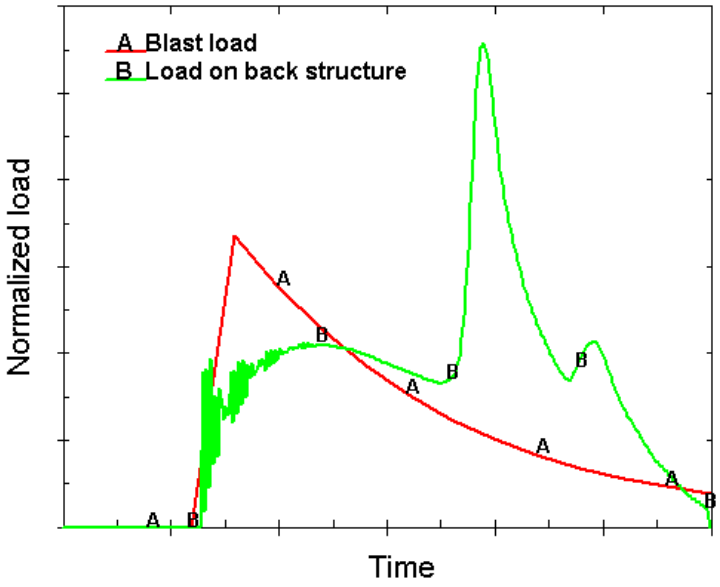

Figure 6.2: Simulation of force enhancement with the homogenized cellular material model

Micro-ball Model

The "micro-ball" model of a cellular material is shown in Fig.6.3. Density and other properties of the cellular material are achieved by choosing the appropriate wall thickness and material properties of the micro balls. Contacts are defined among the micro-balls to represent the internal connections and friction of the cellular material. Figure 6.3a shows a cellular bar under a blast load, using the "micro-ball" model, and Fig. 6.3b shows the simulated deformation of the bar. The bar deforms from near the blast point to the distal end, layer by layer, in a manner similar to what happens in real tests [59].

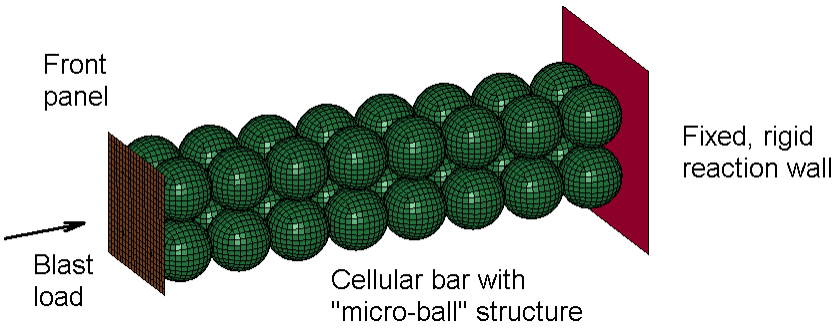

(a)

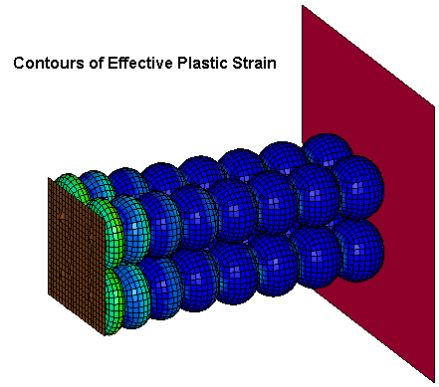

(b)

Figure 6.3: "Micro-ball" cellular material model: (a) a cellular material bar; and (b) deformation of the cellular bar under a blast load.

If it is not fully compacted to the densification strain, the cellular material bar can attenuate the blast load exerted on the front panel as shown in Fig. 6.4a. When the blast load reaches a critical level, the cellular bar is fully compacted and force enhancement happens, as shown in Fig. 6.4b.

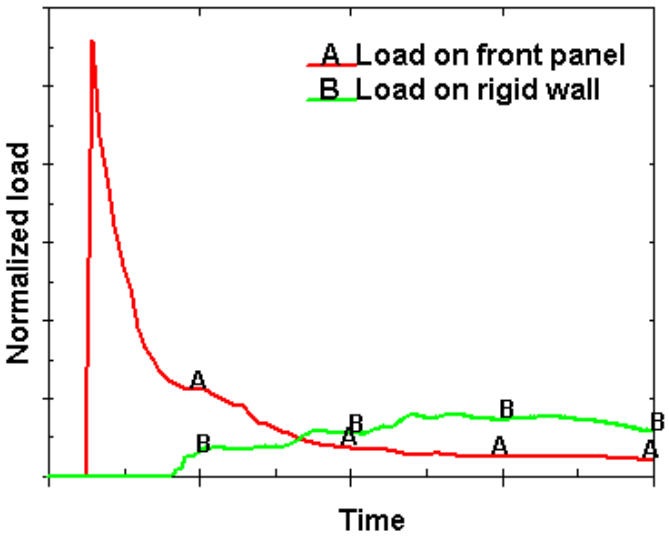

(a)

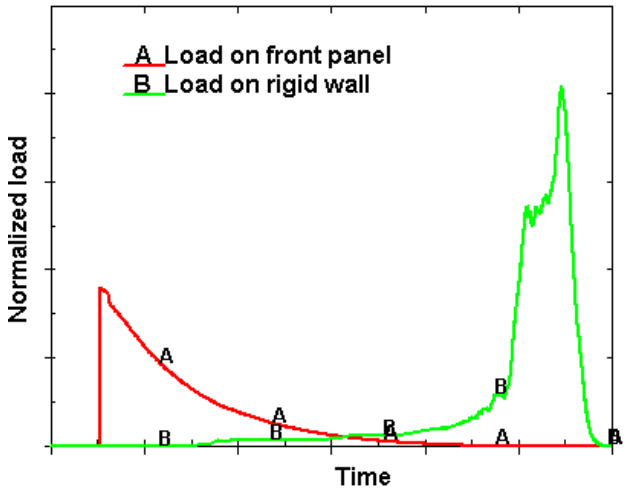

(b)

Figure 6.4: Simulation of cellular material bar response under a blast load using the "micro-ball" model: (a) force attenuation; and (b) force enhancement.

6.1.2 Root Cause Investigation Using an Analytical Model

Consider the situation when a fixed end cellular bar, as shown in Fig. 6.5a, is subjected to a triangular blast pressure pulse $p(t)$ with peak P and duration T, as shown in Fig. 6.6. The length and the cross-section area of the bar are L and A,

respectively. The one-dimensional analytical model, which has N discrete lumped masses connected by N identical non-linear springs, is shown in Fig. 6.5b, where $m_i = m = \rho AL/N$, $i = 1,\ldots,N$, and ρ is the density of the cellular material. The elastic property of the spring is determined by $k_i = k = EA/(L/N)$. The input blast pressure pulse is applied on the N-th lumped mass. The first spring is connected to a rigid wall. A complete description of the compressive stress-strain relation of the non-linear spring is shown in Fig. 6.7, and is characterized by the compressive modulus, E, plateau stress, σ_y, lock-up strain, ε_l, and compressive stress-strain relation $\sigma = \sigma(\varepsilon)$ in the densification range. Dimensional analysis was conducted by Li et al. [62], with five significant non-dimensional numbers given as

$$\varepsilon_y = \frac{1}{E/\sigma_y}$$

$$p = \frac{P}{\sigma_y}$$

$$\tau_d = \frac{T}{L/\sqrt{E/\rho}}$$

$$\varepsilon_l$$

and

$$N$$

and two dimensionless variables, $\bar{y}_j = y_j/L$ and $\tau = t/\left(L/\sqrt{E/\rho}\right)$.

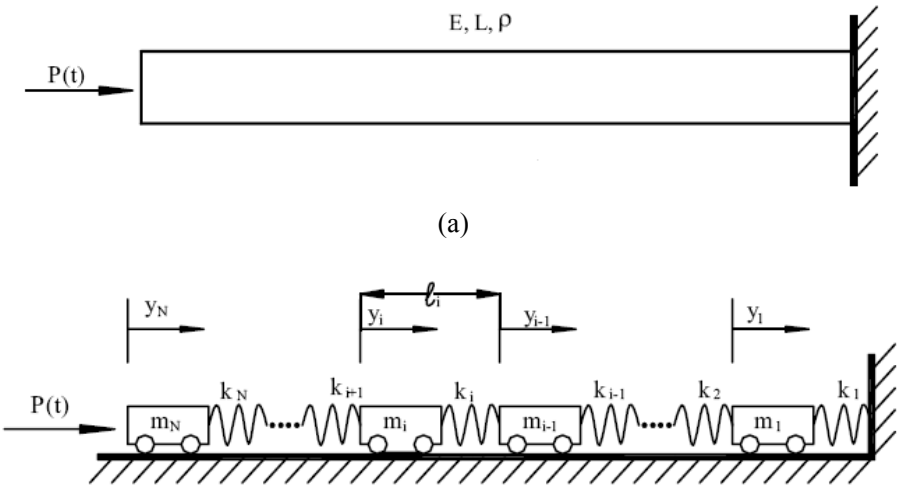

Figure 6.5: (a) Cellular bar subjected to a blast pulse load; and (b) the one-dimensional analytical model of the cellular bar [62]

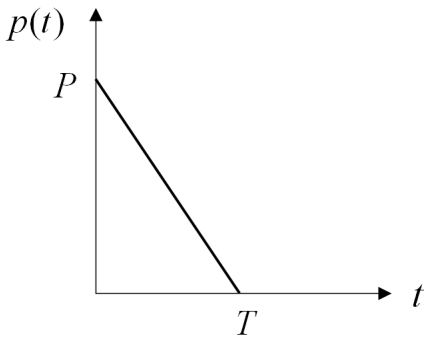

Figure 6.6: Blast load on the cellular material bar

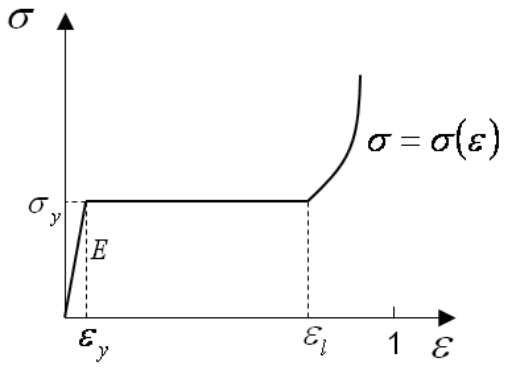

Figure 6.7: Stress-strain curve of non-linear springs

A numerical example is conducted for $\varepsilon_y = 10\%$, $\varepsilon_l = 90\%$, and $N = 3$ to

investigate the blast pulse load transmission in the cellular bar and the root cause of the force enhancement phenomenon; the model is shown in Fig. 6.8. Two different pulse loads are applied to node 1 of the system with the same peak load P, while pulse load 2 has a longer duration than pulse load 1 ($T_2 > T_1$), which provides more impulse to the system. An enhancement factor R is defined as the ratio between the force transmitted to the fixed end and the pulse peak load. Figure 6.9a compares the momentum histories of the two cases, and it is seen that momentum transfer occurs only between nodes 1 and 2 for the low impulse input; while momentum transfer between nodes 1 and 2, 2 and 3, and 3 and 4 (the fixed end) happens for the high impulse input. It is also seen that these momentum transfers happen within very short periods of time. This will result in high force amplitude and high acceleration, as shown in Fig. 6.9b. Once the propagated momentum transferred through the system reaches the fixed end, a high magnitude force is expected, and this will cause the force enhancement at the fixed end. Figure 6.9c depicts the observation that with a lower impulse input, the impulse is attenuated, and the enhancement factor is the ratio of the plateau force of the non-linear spring and the input pulse peak load. At the same time, with a higher impulse input, the system is fully compressed and the enhancement factor is identified as 1.39.

Figure 6.8: A one-dimensional model of fixed end cellular bar with three lumped masses

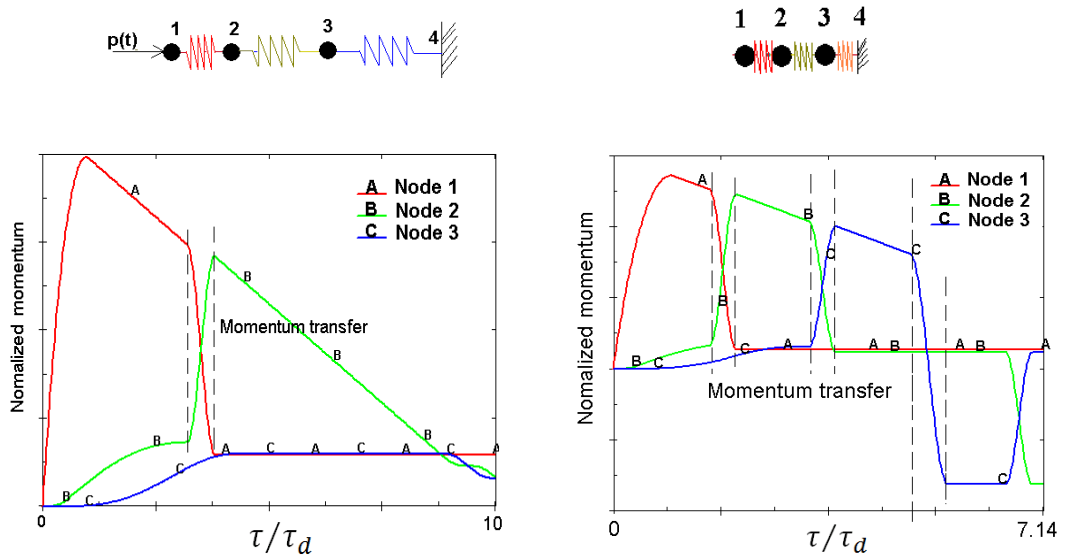

(a)

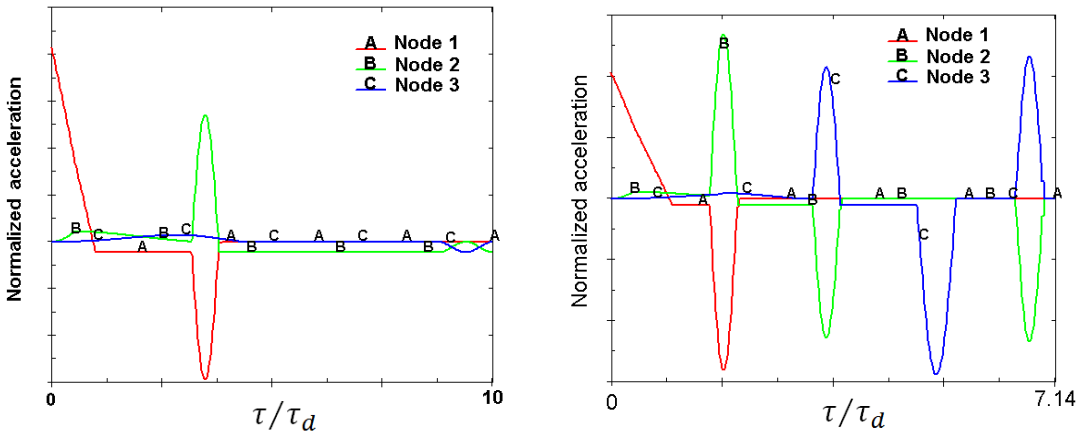

(b)

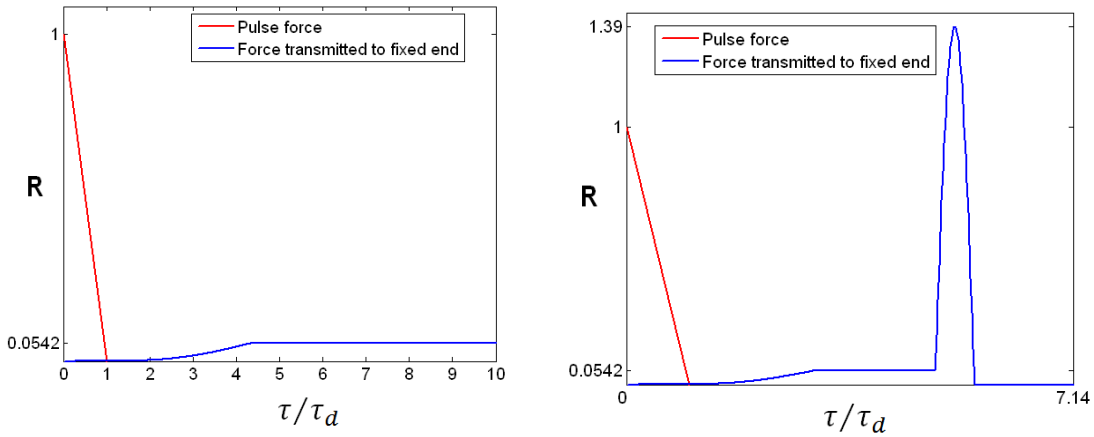

(c)

Figure 6.9: Comparison of system responses with various pulse loads: (a) momentum; (b) acceleration; and (c) force.

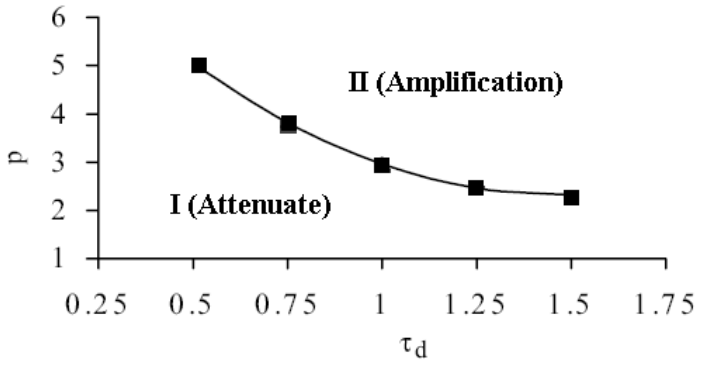

Figure 6.10: Critical load curve of a fixed-end cellular bar

In addition, for a specific fixed-end cellular bar configuration (material and dimension), a critical load curve can be identified as shown in Fig. 6.10. For a blast load with pressure intensity (p) and loading duration (τ_d) under the critical curve, the cellular bar will not be compacted, and the blast force is attenuated at the fixed end. But for a blast load above the critical curve, once the cellular bar is fully compacted, force enhancement is expected. This critical curve can be used to determine when "force enhancement" will happen, so as to assist the appropriate design process.

6.2 Design Strategy Against Force Enhancement

6.2.1 Panel-foam-structure Simulation Model

For vehicle (underbody) blast protection design, the protected structure (vehicle floor) is not fixed in space, and so it will deform along with the attached metal foam armor structure. Taking into account the flexibility of the protected structure will yield a foam armor structure different from the case when the back of the protected structure is fixed.

A FE model has been developed to discover countermeasures that may be employed to prevent force enhancement. As shown in Fig. 6.11a, a square block of aluminum foam is attached to a structural plate that serves to represent the floor of a military vehicle. A frontal panel made of aluminum is attached to the side of the foam cladding that faces the blast load. Note that the frontal panel is used to prevent the disintegration of the aluminum foam cladding under the blast load, as well as to add a buffer mass, so as to reduce the chance of force enhancement. This is demonstrated in the following. For a real underbody armor structure, adding the frontal panel also helps to prevent blast debris from penetrating the vehicle floor and injuring crew members. Figure 6.11b shows a snapshot of the simulated effective stress and deformation of the system.

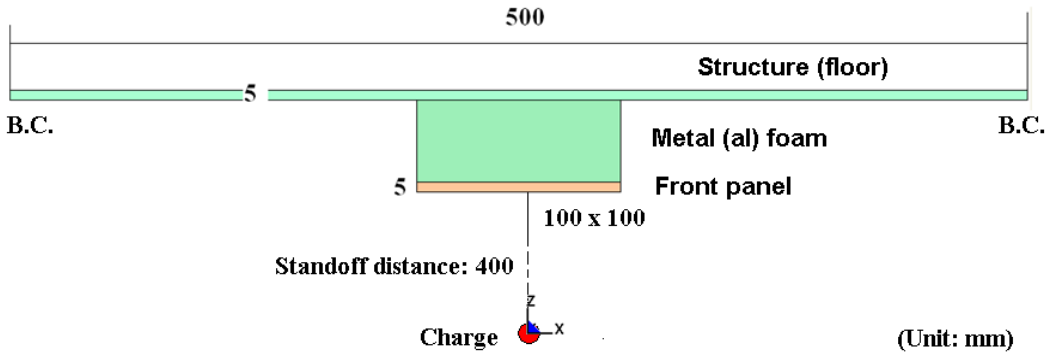

(a)

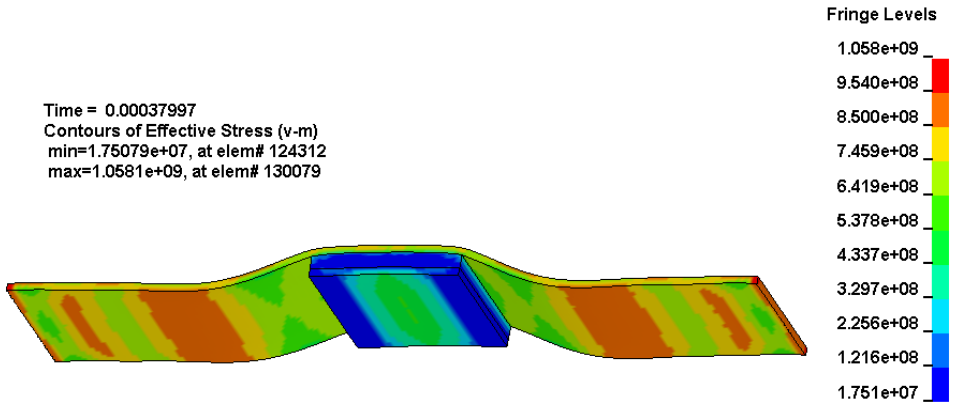

(b)

Figure 6.11: Model of a panel-foam-structure system under a blast load: (a) system configuration; and (b) deformation and effective stress.

The *LOAD_BLAST card in LS-DYNA is utilized to apply blast loads to the frontal panel of the system, with the option ISURF set to 1 to represent a hemispherical charge situated on the surface. Three cases are simulated with charge TNT equivalents of 0.3 kg, 3 kg and 6 kg, respectively. It is seen from Fig. 6.12a, that with a 0.3 kg TNT load, the aluminum foam is loaded only in the elastic region, and the resultant force on the back plate does not show much alleviation compared to the blast load. In fact, Makris [99] and Neremberg [100] showed that by using a shock tube test, that weak blast waves loaded the foam only in the elastic phase, leading to transmitted overpressure amplification. This amplification was attributed to an elastic wave coupling phenomenon. This statement cannot be verified using the current simulation model, since only the solid phase of the foam material is modeled, and the gas response and gas-solid interaction is not being considered. Most cellular materials, whether they made of polymers, metals, or other materials, have relatively high densities, and the stress transmission is determined mainly by

the solid phase. Figure 6.12b shows that when the blast load compresses the foam into its plateau region, the transmitted force on the back plate is attenuated; the amplitude of the transmitted force is limited by the foam plateau stress and the contact area of the foam and the back plate. In this case, no compaction occurs in the aluminum foam cladding. If the blast load is high enough to compress the foam up to the point of densification, the force transmitted to the back plate will be higher than even the blast load, as shown in Fig. 6.12c. Aluminum foam causes force enhancement in this case.

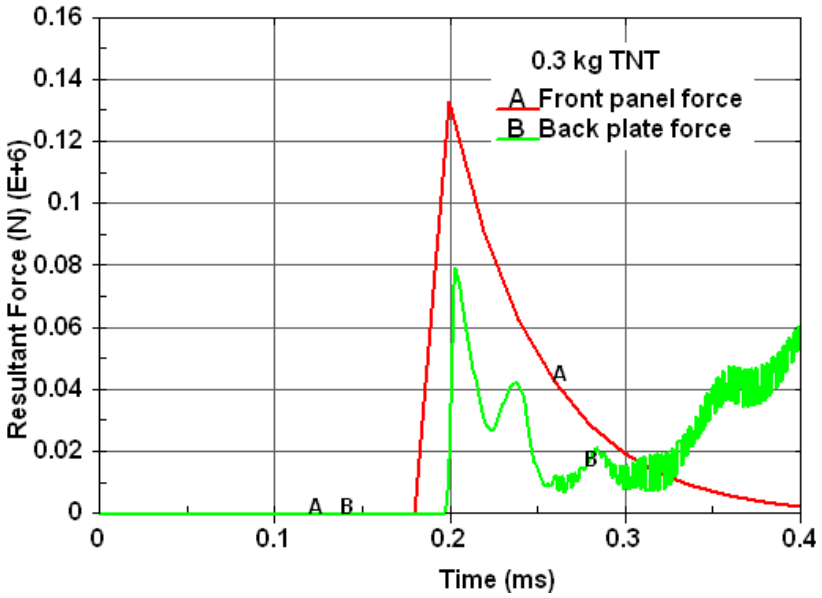

(a)

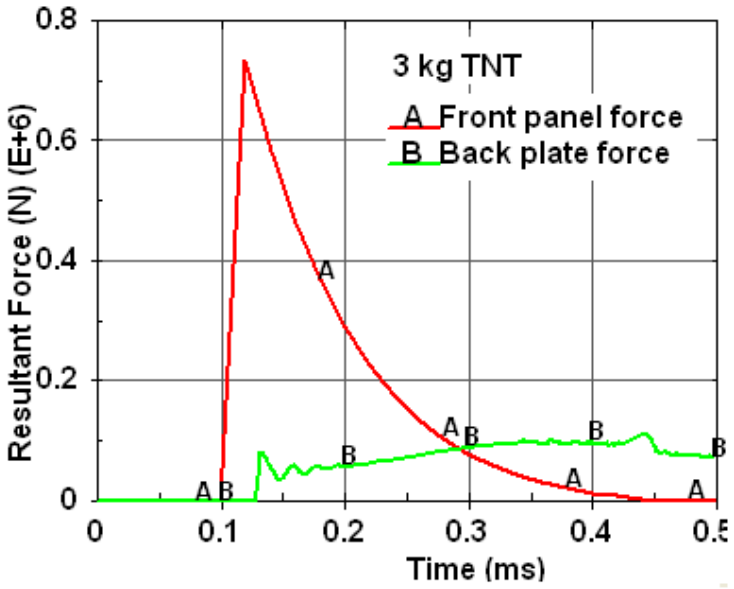

(b)

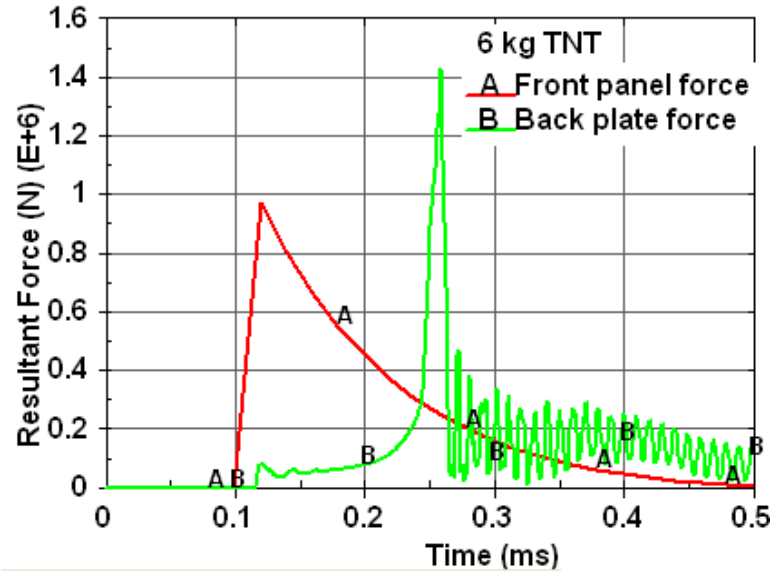

(c)

Figure 6.12: Responses of panel-foam-structure system under various blast loads: (a) 0.3 kg TNT equivalent; (b) 3 kg TNT equivalent; and (c) 6 kg TNT equivalent.

Figure 6.13 further shows the momentum histories of the system under different intensities of blast load. It can be seen from Fig. 6.13a that the momentums are transferred "smoothly" between different components of the system, and the force transmitted to the back plate is attenuated as shown in Fig. 6.12b. Once the blast

load intensity reaches a certain level, the momentum transfer between the components of the system becomes "abrupt," as shown in Fig. 6.13b, where the force transmitted to the back plate is enhanced due to the reduced momentum transfer time.

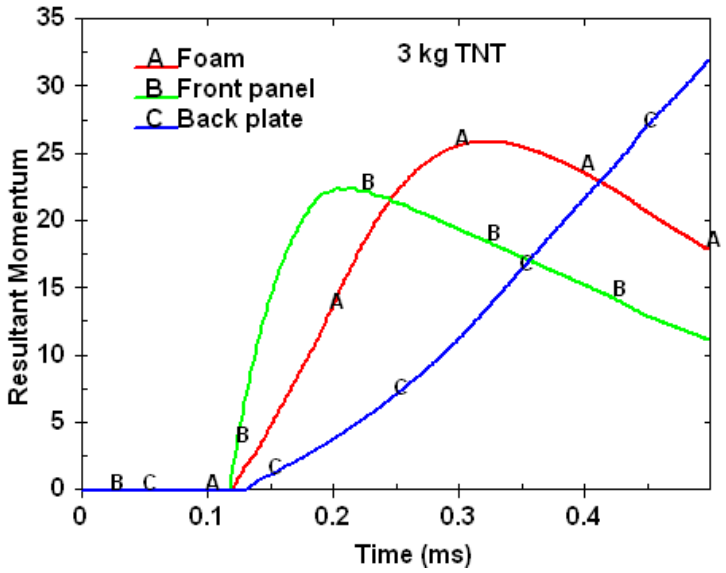

(a)

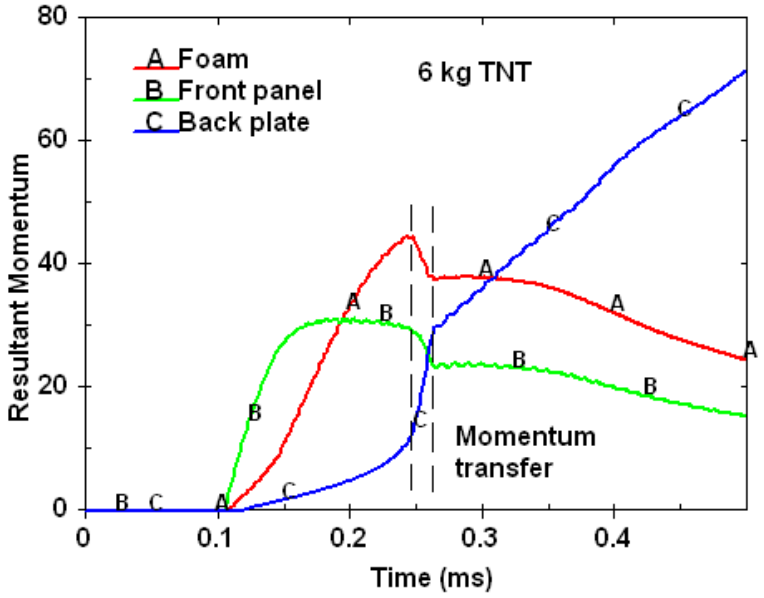

(b)

Figure 6.13: Momentum histories of panel-foam-structure system under various blast loads: (a) 3 kg TNT equivalent; and (b) 6 kg TNT equivalent.

It is assumed that the density and stiffness mismatches between the metal foam and the protected structure at the contact interface cause the "abrupt" momentum transfer, at the moment of foam densification. To verify this assumption, the density and stiffness of the back plate are revised to match those of the metal foam before applying the blast loads to the system.

Density Match

As shown in Fig. 6.14a, by matching the mass densities of the back plate material and the aluminum foam at the interface, the peak force exerted on the back plate is removed. Figure 6.14b depicts the resultant momentum histories of the system with density match, which shows no further "abrupt" momentum transfer occurring.

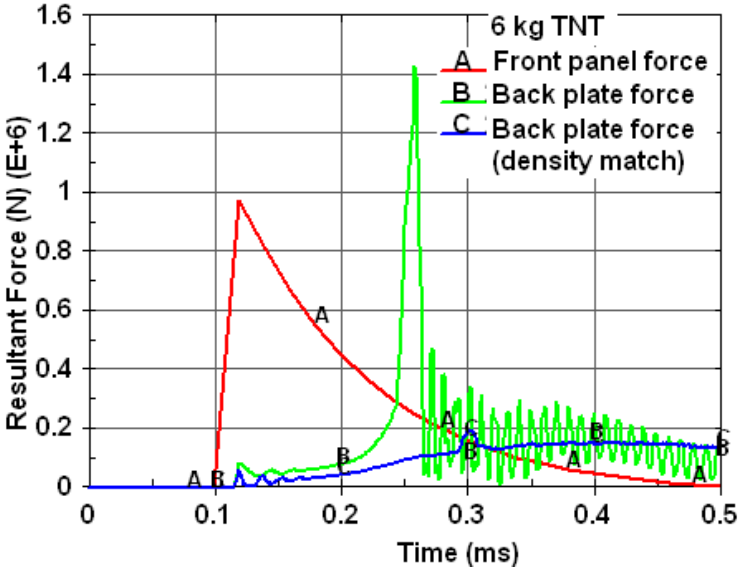

(a)

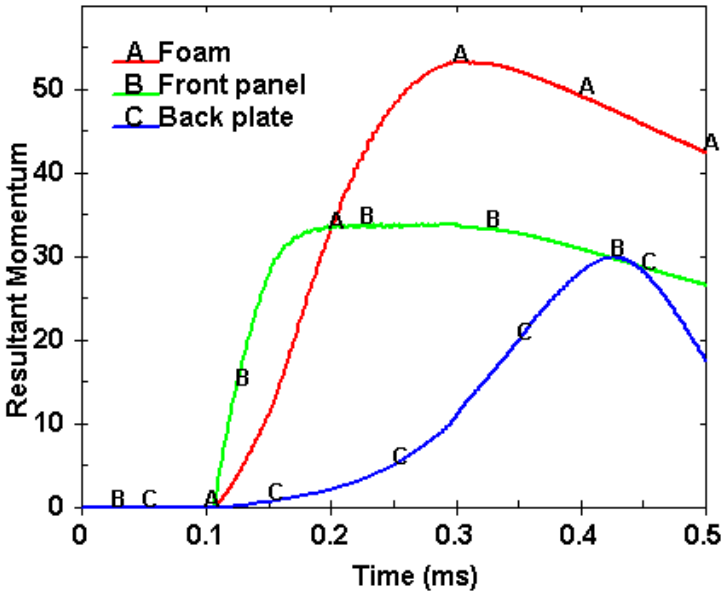

(b)

Figure 6.14: Density match prevents force enhancement: (a) resultant force; and (b) resultant momentum.

Stiffness Match

By matching the stiffness of the back plate material and the aluminum foam at the interface, the enhanced peak force is reduced as shown in Fig. 6.15.

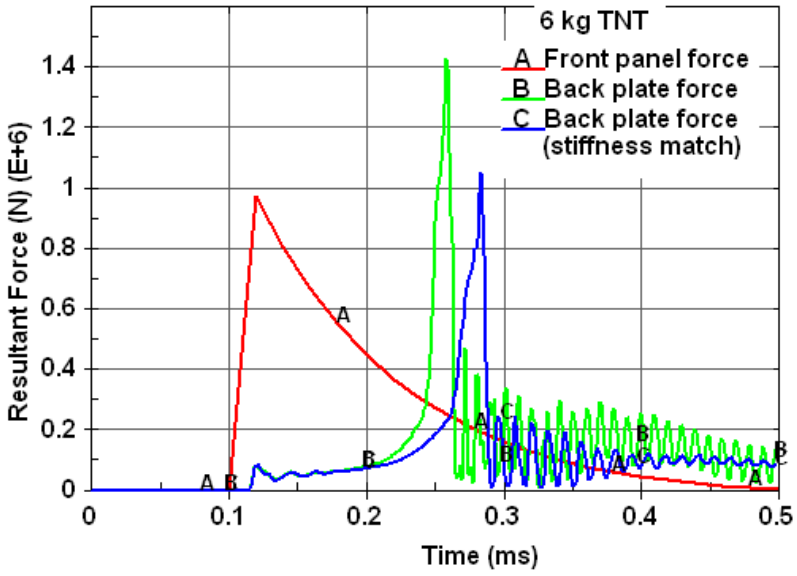

Figure 6.15: Stiffness match reduces enhanced peak force

It can be concluded from the above study that by matching the mass density, and the stiffness between the protected structure and the aluminum foam at the interface, force enhancement by the foam material can be effectively prevented.

Effect of Frontal Panel

As mentioned previously, the frontal panel in the system helps to reduce the chance of force enhancement. The mass, as well as the flexural stiffness of the frontal panel, can mitigate the blast impulse transmitted to the metal foam cladding. As illustrated in Fig. 6.16, under a blast load equivalent to 3 kg TNT, the resultant peak force on the back plate is removed by use of the frontal panel in the system.

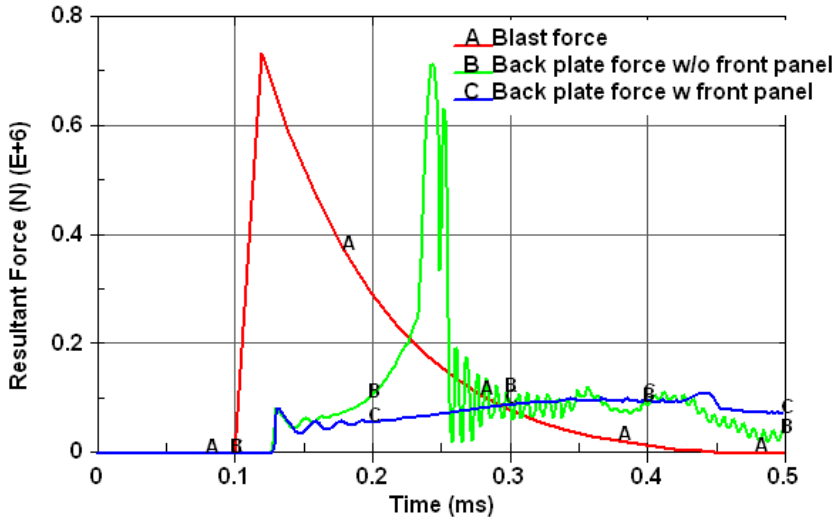

Figure 6.16: Frontal panel helps to prevent force enhancement

6.2.2 Introduce Interim Isolating (I-I) Structure between the Foam and Floor

In reality, a vehicle floor is designed for load bearing purposes; the mass density and stiffness of the floor material are usually not design variables for blast protection. To avoid possible force enhancement when the metal foam enables blast mitigation,

alternative solutions are required. A carefully designed interim (transition) isolating (I-I) structure between the protected structure and the metal foam layer provides a solution to this problem. A possible configuration of I-I structure is shown in Fig. 6.17a. The aim is to disconnect the protected structure from the metal foam layer, in order to prevent the enhanced force from being transmitted to the protected structure upon the compaction of the metal foam layer under a blast load. Figure 6.17b shows that the I-I structure can effectively isolate the protected structure from the compacted foam layer under a blast load. Figure 6.18 demonstrates that the transmitted force to the main structure can be effectively reduced.

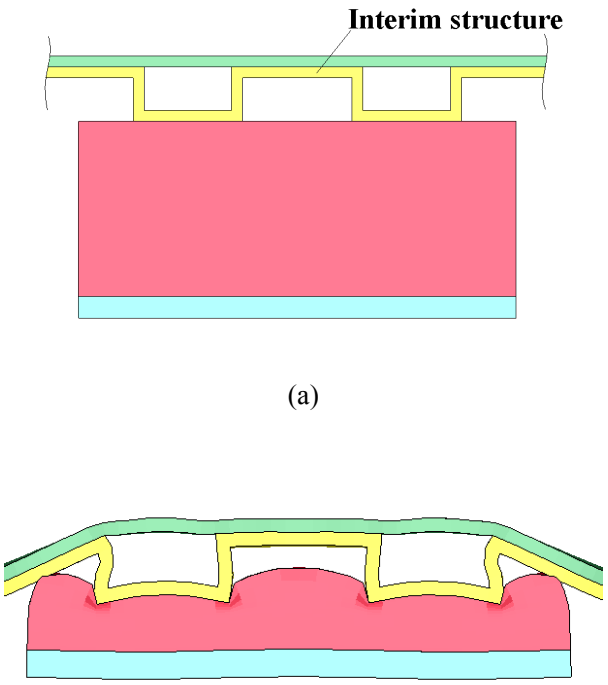

(a)

(b)

Figure 6.17: Interim isolating structure between the protected structure and the metal foam layer: (a) system configuration; and (b) system deformation under a blast load.

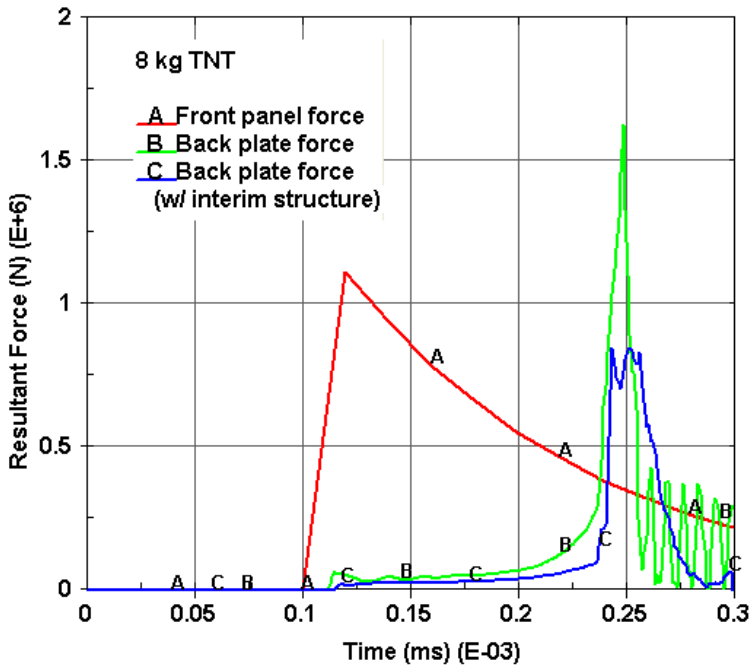

Figure 6.18: Interim isolating structure helps reduce enhanced force on the protected structure

6.2.3 I-I Structure Design Problem

The configuration of an I-I structure can be designed to achieve the greatest blast protection capability by decreasing the effective area of contact between the metal foam layer and the protected structure. Designs can be conducted to achieve the optimal gauge, shape, beads pattern, or even structural topology of the I-I structure. These variations are problem-dependent and are beyond the scope of this research.

6.2.4 Example Results

Consider a blast-protective structure design that uses aluminum foam for blast load attenuation. An I-I structural plate is placed between the foam armor and the vehicle floor, to prevent force enhancement following foam compaction, as shown in Fig. 6.19. The reduced DOF model developed in Chapter V is employed for the

simulation and the design. A landmine with explosive force equivalent to 4 kg of TNT is detonated directly under the left seat mount, at a distance of 0.4 m below the vehicle floor. The design objective is to reduce the force transmitted to the seat mounts from the blast load, so as to reduce the severity of the crew member's pelvic injury.

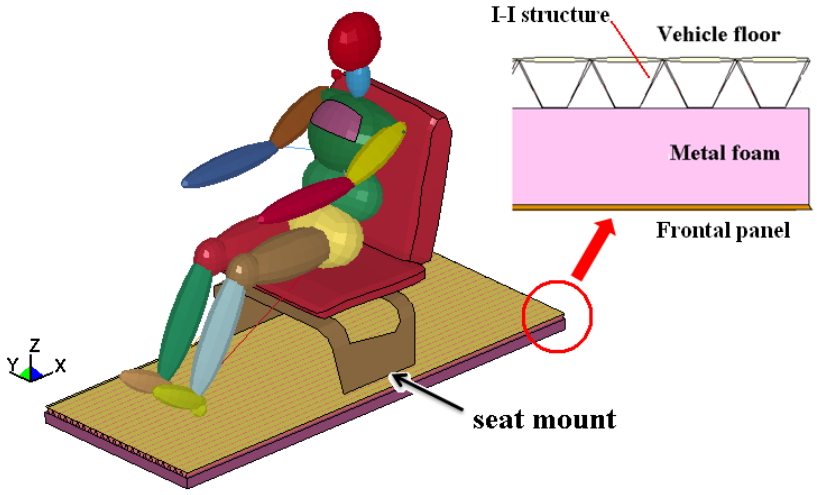

Figure 6.19: Simulation model for blast-protective structure design

Figure 6.21 depicts the side view of the various design configurations of the I-I structural plate; note that the weight added to the baseline design are the same for the design with 6 cm of foam, as in Design 1 and Design 2. Also, the I-I structure has less contact area with the metal foam in Design 2 than in Design 1.

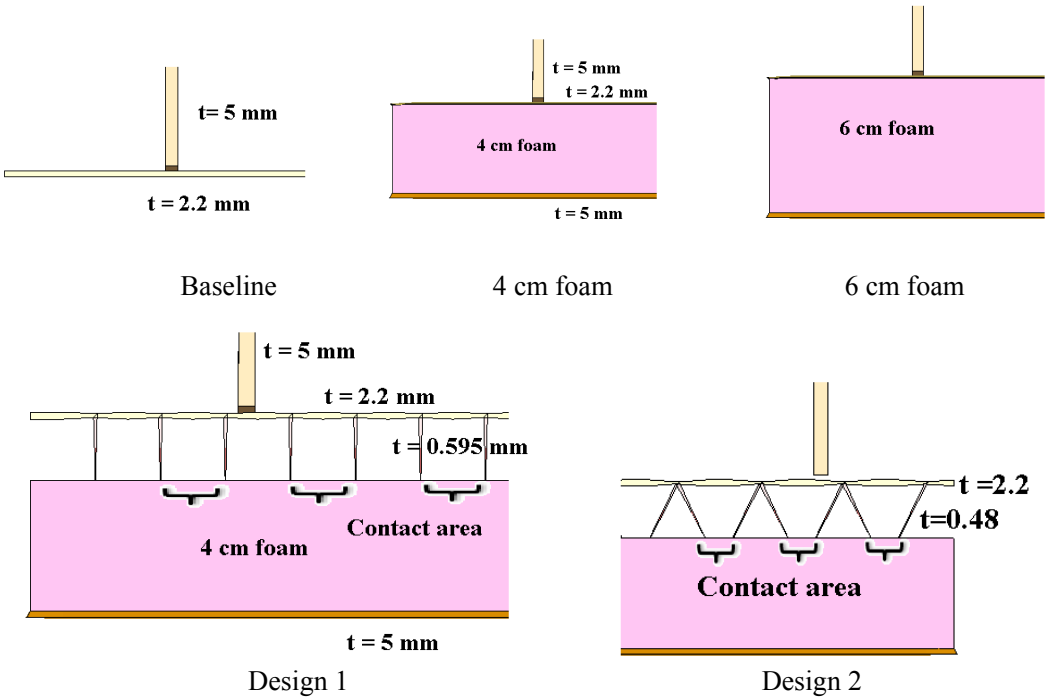

Figure 6.21: Design configurations of an I-I structural plate (side view)

The force transmitted to the seat mount with the different designs are compared in Fig. 6.22a: force enhancement happens when 4 cm of foam is fully compacted under the blast load; the transmitted force is lower than the baseline design with 6 cm of foam, but still has a high peak value. Design 1 eliminates the peak force transmitted to the seat mount, while Design 2, which has less area of contact between the I-I structure and the foam armor than Design 1, further reduces the force level. These results can be verified by examining crew member pelvis accelerations as illustrated in Fig. 6.22b; with the introduction of the I-I structural plate and the decreased area of contact, the crew member's vulnerability to pelvic injury is effectively mitigated. The designed I-I structure is employed in the underbody armor structure of the vehicle system for validation; Figure 6.23 depicts that the I-I

structure can greatly reduce the crew member pelvis acceleration caused by the force enhancement with the foam material under a blast load. Note that the current work is a qualitative study of the I-I structure design undertaken to show a good design strategy; a detailed study with design optimization would give a more thorough and robust picture of the configurations of the blast-protection system.

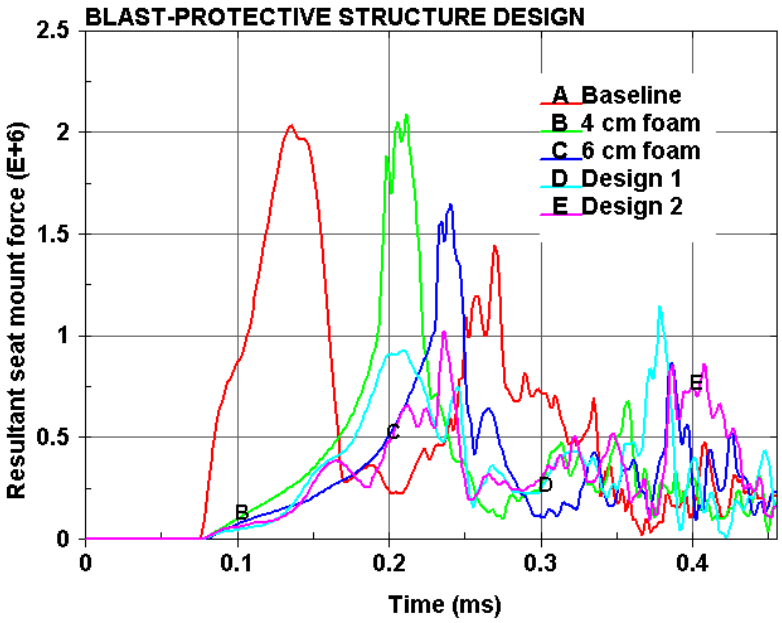

(a)

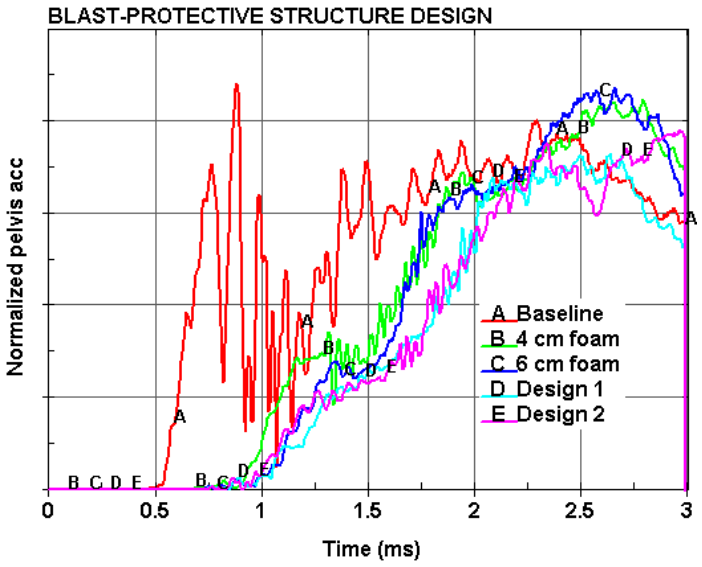

(b)

Figure 6.22: Comparison of various designs: (a) seat mounts forces; and (b) crew pelvis acceleration.

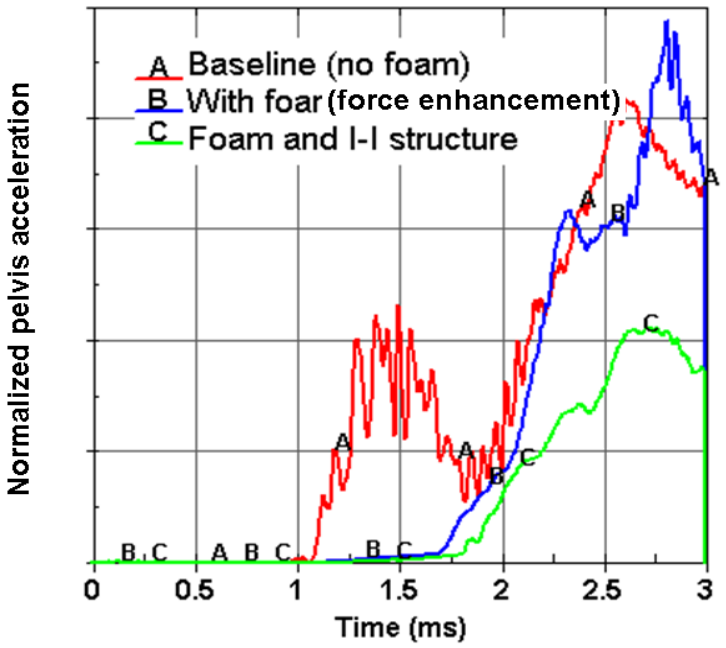

Figure 6.23: I-I structure design validation at vehicle system level

6.3 Conclusions

Force enhancement phenomenon when using cellular materials for blast protection has been investigated using both FE simulations and one-dimensional

analytical model. It was found that the mismatches of the mass density and the stiffness between the cellular material and the protected structure are the root cause of force enhancement. Therefore, force enhancement can be effectively prevented by matching the mass density and stiffness of the protected structure with the cellular material being used. A panel-foam-structure model has been used for validation and demonstration of the findings.

Considering the fact that the mass density and stiffness of the protected structure are difficult to change in a real design situation, an interim isolating (I-I) structure (plate) has been introduced and was shown to be effective at preventing force enhancement. It has also shown by example that reducing the area of contact between the I-I structure and the metallic foam armor can further enhance the blast protection capability of the system.

CHAPTER VII

Conclusions, Contributions, and Future Work

7.1 Conclusions

The complicated physical processes that occur during a crash event along with the complexity of automotive vehicle systems make crashworthiness design a very challenging task. The same is true for the blast protection design. New design approaches need to be developed; approaches that take into account the need to balance computational resources, product-development time, and that utilize available simulation and optimization techniques when working to achieve robust designs. The objective of this research is to develop an advanced and systematic approach for conducting general crashworthiness and blast protection designs for optimization of both structural and material systems.

An effective approach developed in this research is to break the crashworthiness and blast protection design problems into sub-problems through three decompositions in terms of space, time, and scale, using corresponding target cascading processes. Other aspects considered in the design approach also include failure modes management, optimization techniques, multidisciplinary objectives,

and uncertainties. The Magic Cube (MQ) has been developed through considering all of the above aspects, resulting in a systematic design approach for general applications.

Various design problems have been solved by employing the specific elements of the MQ, demonstrating the feasibility and effectiveness of this new approach. These examples include a representative vehicle crashworthiness design problem to meet the desired target of crash force history; a thin-walled tube design problem to address crash angle uncertainties, as well as to reduce the initial peak crash force; an elastomeric mounting system design problem to deal with multidisciplinary objectives; a vehicle frontal frame design for weight reduction via material substitution, and a blast protection system design of a military vehicle with reduced underbody armor weight and improved protection capability against landmine blast uncertainties.

7.2 Contributions

The major contributions of this research can be itemized as following:

1) Development of an advanced and systematic approach, the MQ approach, for generalized crashworthiness and blast protection design problems in terms of both structural and material optimizations.

2) Development of a multi-domain multi-step topology optimization (MMTO) process for laying out novel structural concepts for improving crash energy absorption and crashworthiness of the vehicular components.

3) Development of an objectives reduction approach (ORA) for

multidisciplinary design optimization problems.

4) Inclusion of uncertainties in both crashworthiness and blast protection designs to obtain more robust design configurations.

5) Development of an equal protection design (EPD) concept and an inverse thickness design (ITD) method for underbody armor structure design for weight reduction.

6) Discovery of the root cause of the "force enhancement" phenomenon when cellular material is fully compacted under a blast load. This discovery has led to an effective countermeasure design that improves the blast protection capability of the military vehicle system.

7.3 Future Work

The MQ approach developed in this research provides a general and systematic way for the crashworthiness and blast protection designs. Some additional details would need to be added to the MQ to address problem-specific designs in real engineering applications. Future research may include, but is not limited to:

1) Scale decomposition for an integrated structural-material system and blast-protective material designs with realistic crash (blast) scenarios.

2) Detailed optimization processes for each subsystem and sub-target identified in this research for blast protection design of the overall vehicle system.

3) Experimental testing and verification of the proposed I-I structure against force enhancement with blast loaded cellular material.

4) Application of the MQ approach for other related fields and design problems.

BIBLIOGRAPHY

BIBLOGRAPHY

[1] Yamazaki, K. and Han, J. Maximization of the crushing energy absorption of cylindrical shells. *Advances in Engineering Software*, 31:425-434, 2000.

[2] Yang, R. J. A numerical study of crash optimization. *1999 ASME Design Engineering Technical Conferences*, Las Vegas, Nevada, 1999.

[3] Mayer, R. R., Kikuchi, N. and Scott, R. A. Applications of topology optimization techniques to structural crashworthiness. *International Journal of Numerical Methods in Engineering*, 39:1383-1403, 1996.

[4] Ambrosio, J. A. C. Dynamics of structures undergoing gross motion and nonlinear deformations: a multibody approach. *Computers & Structures*, 59(6): 1001-1012, 1996.

[5] Dias, J. P. and Pereira, M. S. Optimization methods for crashworthiness design using multi-body models. *Computers and Structures*, 82: 1371-1380, 2004.

[6] Green, J. E. Computer simulation of car-to-car collisions. *SAE Paper*, 770015.

[7] Kamal, M. M. Analysis and simulation of vehicle to barrier impact. *SAE Paper*, 700414.

[8] Lim, G. G. and Paluszny, A. Side impact research. *SAE Paper*, 885055.

[9] Magee, C. L. Design for crash energy management - present and future developments. *The Seventh International Conference on Vehicle Structural Mechanics*, 1988.

[10] Hamza, K. and Saitou, K. Design optimization of vehicle structures for crashworthiness using equivalent mechanism approximations.

[11] Dias, J. P. and Pereira, M. S. Design for vehicle crashworthiness using multi-body dynamics. *International Journal of Vehicle Design*, 15(6), 1994.

[12] Pereira, M. S., Ambrosio, J. A. C. and Dias, J. P. Crashworthiness analysis and design using rigid-flexible multibody dynamics with application to train vehicles. *International Journal for Numerical Methods in Engineering*, 40: 655-687, 1997.

[13] Soto, C. A. and Díaz, A. R. Basic models for topology design optimization in crashworthiness problems. *Proceedings of DETC 99, 1999 ASME Design Engineering Technical Conference*, Las Vegas, Nevada, USA, 1999.

[14] Pedersen, C. B. W. Topology optimization of 2D-frame structure with path dependent response. *International Journal for Numerical Methods in Engineering*, 57:1471-1501, 2003.

[15] Yang, R. J., Tseng, L., Nagy, L. and Cheng, J. Feasibility study of crash optimization, ASME, DE-Vol. 69(2): 549-556, 1994.

[16] Etman, L. F. P., Adriaens, J. M. T. A., Slagmaat, M. T. P. and Schoofs, A. J. G. Crash worthiness design optimization using multipoint sequential linear programming. *Structural Optimization*, 12: 222-228, 1996.

[17] Schramm, U. and Thomas, H. Crashworthiness design using structural optimization. *7Th Multidisciplinary Analysis and Optimization Conference*, St. Louis, MO, 1998.

[18] Wang, H., Lin, Z. Q. and Jin, X. L. Study on optimal design of automotive body structure crashworthiness. *7th International LS-DYNA Users Conference*.

[19] Avalle, M., Chiandussi, G. and Belingardi, G. Design optimization by response surface methodology: application to crashworthiness design of vehicle structures. *Structural and Multidisciplinary Optimization*, 24: 325-332, 2002.

[20] Marklund, P. O. and Nilsson, L. Optimization of a car body component subject to side impact. *Structural and Multidisciplinary Optimization*, 21(5): 383-392, 2001.

[21] Redhe, M. and Nilsson, L. Optimization of the new Saab 9-3 exposed to impact load using a space mapping technique. *Structural and Multidisciplinary Optimization*, 27:411-420, 2004.

[22] Hajela, P. and Berke, L. Neural networks in engineering analysis and design: an overview. *Computer Systems Engineering*, 3: 525-539, 1992.

[23] Hajela, P. and Lee, E. Topological optimization of rotorcraft sub-floor structures for crashworthiness considerations. *Computers and Structures*, 64(1-4): 65-76, 1997.

[24] ModeFrontier 3.2.1 User's Manual.

[25] Bendsøe, M. P. and Kikuchi, N. Generating optimal topologies in structural design using a homogenization method. *Computer Methods in Applied Mechanics and Engineering*, 71(2): 197-224, 1988.

[26] Gea, H. C. and Luo, J. H. Design for energy absorption: a topology optimization approach. *ASME 2001 Design Engineering Technical Conference and Computers and Information in Engineering Conference*, Pittsburgh, 2001.

[27] Soto, C. A. Optimal structural topology design for energy absorption: a heuristic approach. *Proceedings of DETC'01, ASME 2001 Design Engineering Technical Conference and Computers and Information in Engineering Conference*, Pittsburgh, PA, USA, 2001.

[28] Díaz, A. R. and Soto, C. A. Lattice models for crash resistant design and optimization. *Proceedings of 3rd World Congress of Structural and Multidisciplinary Optimization*, Buffalo, New York, 1998.

[29] Arora, J. S., Kim, C. H. and Mijar, A. R. Simplified models for automotive crash simulation and design optimization. *Proceedings of 3rd World Congress of Structural and Multidisciplinary Optimization*, Buffalo, New York, U.S.A, 1999.

[30] Knap, L. and Holnicki-Szulc, J. Optimal design of adaptive structures for the best crashworthiness. *Proceedings of 3rd World Congress of Structural and Multidisciplinary Optimization*, Buffalo, New York, 1998.

[31] Yamakawa, H., Tsutsui, Z., Takemae, K., Ujita, Y. and Suzuki, Y. Structural optimization for improvement of train crashworthiness in conceptual and preliminary designs. *Proceedings of 3rd World Congress of Structural and Multidisciplinary Optimization*, Buffalo, New York, USA, 1998.

[32] Marzec, Z. and Holnicki-Szulc, J. Adaptive barriers with maximal impact energy absorption. *Proceedings of 3rd World Congress of Structural and Multidisciplinary Optimization*, Buffalo, New York, USA, 1999.

[33] Ma, Z. D., Kikuchi, N., Pierre, C. and Raju, B. Multi-domain topology optimization for vehicle structure design. In: *Proceeding of the 2002 ASME International Mechanical Engineering Congress and Exposition*, New Orleans, LA. (IMECE2002-32908), 1-10, November 2002.

[34] Wang, H., Ma, Z.-D., Kikuchi, N., Pierre, C. and Raju, B. Multi-Domain Multi-Step topology optimization for vehicle structure crashworthiness design. *SAE Paper*, 2004-01-1173.

[35] Yang, R. J. Multidiscipline topology optimization. *Computers & Structures*, 63(6):1205-1212, 1997.

[36] Sobieski, J., Kodiyalam, S. and Yang, R. J. Optimization of car body for noise, vibration and harshness (NVH) and crash. *Proceedings of the AIAA/ASME/ASCE/AHS/ASC 41st Structures, Structural Dynamics and Materials Conference,* AIAA, Atlanta, AIAA Paper No. 2000-1521.

[37] Craig, K. J., et al. MDO of automotive vehicle for crashworthiness and NVH using response surface methods. *AIAA Paper*, 2002-5607, 2002.

[38] Yang, R. J. and Choi, K. K. Reliability-based multidisciplinary design optimization of a full vehicle system. *43rd AIAA/ASME/ASCE/AHS/ASC Structures, Structural Dynamics, and Materials Conference*, Denver, Colorado, USA, 2002.

[39] Kodiyalam, S., Yang, R. J., Gu, L. and Tho, C.-H. Multidisciplinary design optimization of a vehicle system in a scalable, high performance computing

environment. *Structural and Multidisciplinary Optimization*, 26: 256-263, 2004.

[40] Kodiyalam, S. and Sobieski, J. S. Multidisciplinary design optimization-some formal methods, framework requirements, and application to vehicle design. *International Journal of Vehicle Design*, 25, 2001.

[41] Youn, B. D., Choi, K. K., Yang, R. J. and Gu, L. Reliability-based design optimization for crashworthiness of vehicle side impact. *Structural and Multidisciplinary Optimization*, 26: 272-283, 2004.

[42] Koch, P. N., Yang, R.-J. and Gu, L. Design for six sigma through robust optimization. *Structural and Multidisciplinary Optimization,* 26: 235-248, 2004.

[43] Carruthers, J. J., Kettle, A. P. and Robinson, A. M. Energy absorption capability and crashworthiness of composite material structures: a review.

[44] Ramakrishna, S. Microstructural design of composite materials for crashworthy structural applications. *Materials & Design*, 18(3):167-176, 1997.

[45] Pytleski, J. L. and Catherino, H. Lightweight hull floor program. *ARL-CR-58*, U. S. Army Research Laboratory, Watertown, MA, USA, 1993.

[46] Guruprasad, S. and Mukherjee, A. Layered sacrificial claddings under blast loading. Part I – analytical studies. *International Journal of Impact Engineering*, 24: 957-73, 2000.

[47] Guruprasad, S. and Mukherjee, A. Layered sacrificial claddings under blast loading. Part II – experimental studies. *International Journal of Impact Engineering*, 24: 975-84, 2000.

[48] Condon, J. A., Gniazdowski, N. and Gregory, F. H. The design, testing, and analysis of a proposed composite hull technology mine-blast-resistant vehicle floor panel. *ARL-TR-796*, 1995.

[49] Ashby, M. E., Evans, A., Fleck, N. A., Gibson L. J., Hutchinson, J. W. and Wadley, H. N. G. Metal foams: a design guide. Butterworth-Heinemann, 2000.

[50] Gama, B. A., Bogetti, T. A., Fink, B. K., Yu, C.-J., Claar, T. D., Eifert, H. H. and G, J. W. Aluminum foam integral armor: a new dimension in armor design. *Composite Structures*, 52: 381-395, 2001.

[51] Monti, R. Normal shock wave reflection on deformable solid walls. *Meccanica*, 4: 285-296, 1970.

[52] Gel'fand, B. E., Gubin, S. A., Kogarko, S. M. and Popov, O. E. Investigation of propagation and reflection of pressure waves in porous media. *Zh. Prikl. Mekh, Tekh. Fiz*, 16:74-77, 1975.

[53] Reid, S. R., Bell, W. W., Barr, R. Structural plastic model for one-dimensional ring system. *International Journal of Impact Engineering*, 1: 185-191, 1983.

[54] Reid, S. R., Reddy, T. Y., Peng, C. Dynamic compression of cellular structures and materials. In: Jones, N., Wierzbicki, T., editors. *Structural crashworthiness and failure*. London: Elsevier Application Science, 295-340, 1993.

[55] Song, B., Hu, S. S. and Liu, J. F. Shock wave in foam plastic. *Journal of experimental mechanics*, 14: 273-8, 1999.

[56] Skew, B. W., Atkins, M. D. and Seitz, M. W. The impact of a shock wave on porous compressive foams. *Journal of Fluid Mechanics*, 253:245-65, 1993.

[57] Mazor, G, Ben-Dor, G., Igra, O. and Sorek, S. Shock wave interaction with cellular materials. Part I – analytical investigation and governing equations. *Shock Waves*, 3: 159-65, 1994.

[58] Ben-Dor, G., Mazor, G., Igra, O. and Onadera H. Shock wave interaction with cellular materials, Part II: open cell foams-experimental and numerical results. *Shock Waves*, 3: 167-79, 1994.

[59] Hanssen, A. G., Enstock, L. and Langseth, M. Close-range blast loading of aluminum foam panels. *International Journal of Impact Engineering*, 27: 593-618, 2002.

[60] Ouellet, S., Frost, D. and Bouamoul, A. Using a shock tube to predict the response of polymeric foam to a blast loading. *Journal of Physics IV France*, 134:783-87, 2006.

[61] Olim, M., van Dongen, M. E. H., Kitamura, T. and Takayama, K. Numerical simulation of the propagation of shock waves in compressible open-cell porous foams. *International Journal of Multiphase Flow*, 20:557-68, 1994.

[62] Li, Q. M. and Meng, H. Attenuation or enhancement - a one-dimensional analysis on shock transmission in the solid phase of a cellular material. *International Journal of Impact Engineering*, 27:1049-65, 2002.

[63] Ma, G. W. and Ye, Z. Q. Energy absorption of double-layer foam cladding for blast alleviation. *International Journal of Impact Engineering*, 34: 329-347, 2007.

[64] Ma, G. W. and Ye, Z. Q. Analysis of foam claddings for blast alleviation. *International Journal of Impact Engineering*, 34: 60-70, 2007.

[65] Han, D. C. and Park, S. H. Collapse behavior of square thin-walled columns subjected to oblique loads. *Thin-Walled Structures*, 35: 167-184, 1999.

[66] Qi, C., Ma, Z.-D., Kikuchi, N., Pierre, C., Wang, H. and Raju, B. B. Fundamental studies on crashworthiness design with uncertainties in the system. *SAE Paper*, 2005-01-0613.

[67] Ralston, A. A first course in numerical analysis. McGraw Hill, 1965.

[68] Lord, H. C. Vibration dampening mounting, US Patent 1,778,503, 14 October 1930.

[69] Browne, K. A. and Taylor, E. A. Engine mount, US Patent 2,175,825, 10 October 1939.

[70] Coleman, E. W. and Alstadt, D. M. Bonding rubber to metal, US Paten 2,900,292, 18 August 1959.

[71] Miller, L. R. and Ahmadian, M. Active mounts - a discussion of future technological trends. *Inter-noise Conference*, Toronto, Canada, 1992.

[72] Arai, T., Kubozuka, T. and Gray, S. D. Development of an engine mount optimization method using modal parameters, *SAE Paper*, 932898.

[73] Bernard, J. E. and Starkey, J. Engine mount optimization. *SAE Paper*, 830257.

[74] Geck, P. E. and Patton, R. D. Front wheel drive engine mount optimization, *SAE Paper*, 840736.

[75] Johnson, S. R. and Subhaedar, J. W. Computer optimization of engine mounting systems. *SAE Paper*, 790974.

[76] Spiekermann, C. E., Radeliffe, C. J. and Goodman, E. D. Optimal design and simulation of vibrational isolation systems, *Journal of Mechanism, Transmissions, and Automation in Design*, 1985.

[77] Swanson, D. A., Wu, H. T. and Ashrafiuno, H. Optimization of aircraft engine suspension system. *Journal of Aircraft*, 30(6): 979-984, 1993.

[78] Ashrafiuon, H. Design optimization of aircraft engine-mount systems. *Journal of Vibration and Acoustics*, 115: 463-467, 1993.

[79] Lee, J. M., Yin, H. J. and Kim, J. H. Flexible chassis effects on dynamic response of engine mount systems. *SAE Paper*, 951094.

[80] Suresh, N., Shankar, S. and Bokil, V. Development of idealistic hydromount characteristics to minimize engine induced vibrations using unconstrained minimization. *SAE Paper*, 932432.

[81] Wise, K. A. and Reid, R. E. Modeling and identification of a light truck engine mounting system for ride quality optimization. *SAE Paper*, 841142.

[82] Ma, Z. D., Kikuchi, N. and Cheng, H. C. Topological design for vibrating structures. *Computer Methods in Applied Mechanics Engineering*, 121:259-280, 1995.

[83] Madsen, H. O., Krenk, S. and Lind, N. C. *Methods of structural safety*, Prentice-Hall Inc., Englewood Cliffs, NJ, 1986.

[84] Hasofer, A. M. and Lind, N. C. Exact and invariant second-moment code format. *Journal of Engineering Mechanics*, Division ASCE, 100 (EMI):111-121, 1974.

[85] Wierzbicki, T. and Abramowicz, W. On the crushing mechanics of thin-walled structures. *Journal of Applied Mechanics*, 50:727-34, 1983.

[86] Kingery, C. N. and Bulmash, G. Air-blast parameters from TNT spherical air blast and hemispherical surface blast. *ARBRL-TR-o2555*, U.S. Army Ballistic Research Laboratory, Aberdeen Proving Ground, 1984.

[87] Beshara, F. B. A. Modeling of blast loading on aboveground structures-I. General phenomenology and external blast. *Computers and Structures*, 51(5): 585-596, 1994.

[88] Beshara, F. B. A. Modeling of blast loading on aboveground structures-II. Internal blast and ground shock. *Computers and Structures*, 51(5): 597-606, 1994.

[89] Taylor, G. I. The propagation and decay of blast waves. UK Home Office, ARP dept, Rc 39, 1939.

[90] Alem, N. M. Mine blast acceleration injury assessment: methods, criteria and software. Report No. 97-04, USAARL, 1996.

[91] Black, A. N., Christopherson, D. C. and Zuckerman, S. Fractures of the head and feet. Ministry of Home Security, R.C. 334, London, U.K., 1942.

[92] Draeger, R. H. *et.al.* A study of personnel injury by "solid blast" and the design and evaluation of protective devices. research project X-517, Report No. 1, Naval Medical Research Institute, 1945.

[93] LS-DYNA Keyword User's Manual, Version 960, LSTC, Livermore, CA, 2001.

[94] Dobratz, B. M. and Crawford, P. C. LLNL explosive handbook. properties of chemical explosives and explosive stimulants, *Lawrence Livermore National Laboratory Report* UCRL-52997 Change 2, 8-22 to 8-23, 1985.

[95] Wang, J. Simulation of landmine explosion using LS-DYNA3D software: benchmark work of simulation of explosion in soil and air. *DSTO-TR-1168*.

[96] Horst, M. J. v., Simms, C. K., Maasdam, R. V. and Leerdam, P. J. C. Occupant lower leg injury assessment in landmine detonations under a vehicle.

[97] Williams, K. and Gourdeau, F. F. Numerical simulation of light armored vehicle occupant vulnerability to anti-vehicle mine blast. *7th International LS-DYNA Users Conference*.

[98] Hall, I. W., Guden, M. and Yu, C. J. Crushing of aluminum closed cell foams: density and strain rate effects. *Scripta mater*, 43: 515-521, 2000.

[99] Makris, A., Frost, D. L., Neremberg, J. and Lee, J. H. S. in Proceeding of the 20th Int. Symp. On Shock Waves, edited by B. Sturtevant, J. E., Sheperd, H.G.Hornung (World scientific, 1995); 1987.

[100] Neremberg, J., Frost, D. L. and Makris, A. *Proceedings of the 21th Int. Symp. On Shock Waves*, 1997.